STUDY OF THE MOST AMPLIFIED WAVELENGTH GÖRTLER VORTICES

TANDIONO

NATIONAL UNIVERSITY OF SINGAPORE

2009

STUDY OF THE MOST AMPLIFIED WAVELENGTH GÖRTLER VORTICES

TANDIONO

(Sarjana Teknik, ITB)

A THESIS SUBMITTED

FOR THE DEGREE OF DOCTOR OF PHILOSOPHY

DEPARTMENT OF MECHANICAL ENGINEERING

NATIONAL UNIVERSITY OF SINGAPORE

2009

ACKNOWLEDGEMENTS

First and foremost, all praises and thanks be to God for all the gifts to me until now so that this research work can be finished. His guidance is indispensable, and I am nothing without Him.

I would also like to express my sincere appreciation to my supervisors, Associate Professor S. H. Winoto and Dr. D. A. Shah for their precious guidance, encouragement, and support throughout the years. To all staff members and fellow research students in the Fluid Mechanics Laboratory, Department of Mechanical Engineering, I am thankful for their valuable assistance, help, and advice in carrying out my experimental work.

I dedicate this work to my parents, sisters, and brother, and I thank them for their unyielding support, care, and concern throughout the years. I would never have gone this far without them.

Lastly, I am grateful to the National University of Singapore for the opportunity and the Research Scholarship to pursue the PhD degree program in the Department of Mechanical Engineering.

.

TABLE OF CONTENTS

SUMMARY

Concave surface boundary layer flow is subjected to centrifugal instability due to the imbalance between the centrifugal force and the radial pressure gradient, in addition to the viscous effect. This instability is called Görtler instability which manifests itself in the form of streamwise counter-rotating vortices, known as Görtler vortices. These vortices will be amplified resulting in three-dimensional boundary layer which gives rise to spanwise variation of streamwise velocity, boundary layer thickness, and wall shear stress.

The main objective of the present work is to experimentally investigate the characteristics of the boundary layer in the presence of the most amplified wavelength Görtler vortices. The experiments were conducted in a 90° curved plexiglass duct connected to a low speed, blow down type wind tunnel. The wavelength of the Görtler vortices is pre-set by a set of vertical wires placed prior and perpendicular to the leading edge of a concave surface. The velocity measurements were carried out by means of hot-wire anemometers (single probe and *X*-wire probe). The growth and breakdown of the vortices were investigated for three different configurations of free-stream velocities and wire spacings which correspond to the most amplified wavelength Görtler vortices. The pre-set wavelength Görtler vortices were found to preserve downstream which confirm the prediction of the most amplified wavelength Görtler vortices by using Görtler vortex stability diagram.

The vortex growth rate can be expressed in term of maximum disturbance amplitude. Comparison with the previous available results shows that all data of maximum disturbance amplitude obtained from the same experimental set-up seem to lie on a single line when they are plotted against Görtler number, regardless of the

values of free-stream velocity and concave surface radius of curvature. The normal position of maximum disturbance amplitude reaches the maximum point at the onset of nonlinear region before it drastically drops as the secondary instability overtakes the primary instability. The secondary instability is initiated near the boundary layer edge when the flow is sufficiently nonlinear, and it manifests itself as either varicose or sinuous mode.

The spanwise velocity measurement shows alternate regions of positive and negative spanwise velocity across boundary layer, indicating the appearance of Görtler vortices. The secondary motion is observed in the head of vortices, and this may be due to the amplification of free-stream disturbances caused by the secondary instability. The mushroom-like structures are found to oscillate in the spanwise direction, intensely at the vortex head and in the region near the wall.

Near-wall velocity measurements were carried out to identify the "linear" layers of the boundary layer velocity profiles. The wall shear stress coefficient C_f was estimated from the velocity gradient of the "linear" layer. The spanwise-averaged wall shear stress coefficient $\overline{C}_f$, which initially follows the Blasius curve, increases well above the local turbulent boundary layer value in the streamwise direction due to the nonlinear effect of Görtler instability and the secondary instability modes. The varicose mode is found to have a greater contribution to the enhancement of the wall shear stress than the sinuous mode.

LIST OF FIGURES

LIST OF SYMBOLS

$A, B, \hat{B}$	calibration constants
$A', B', \hat{B}'$	temperature compensated calibration constants
C_f	wall shear stress coefficient $\left(=\tau_w / 0.5\rho U_\infty^2\right)$
$\overline{C}_f$	spanwise-averaged wall shear stress coefficient
d	diameter of the hot-wire
e, e_0	perturbation energy, Eq. (5.1)
E	relative perturbation energy $\left(=e/e_0\right)$
	voltage output of CTA system, Eq. (3.1)
E^*	temperature compensated voltage output of CTA system, Eq. (3.2)
f	unstable frequency of secondary instability modes
f, g	yaw functions, Eq. (3.15)
G_θ	Görtler number based on momentum thickness, Eq. (2.1)
$G_{\theta,cr}$	critical Görtler number
$G_{\theta,tr}$	value of Görtler number at the onset of transition
k	yaw coefficient
l	length of the active hot-wire element
l^+	dimensionless wire length $\left(=l u_\tau / \nu\right)$
P_z	vortex amplification parameter based on spanwise gradient of streamwise
	velocity, Eq. (4.2)
r	Pearson product-moment correlation coefficient

R	concave surface radius of curvature
Re_θ	Reynolds number based on momentum thickness
T_a	ambient temperature
T_w	hot-wire temperature
Tu	turbulence intensity, Eq. (3.11)
u, v, w	mean streamwise, normal, and spanwise velocity components
u', v', w'	fluctuating stremwise, normal, and spanwise velocity components
$\hat{u}$	instantaneous velocity, Eq. (3.9)
u_τ	friction velocity $\left(=\sqrt{\tau_w/\rho}\right)$
$\tilde{u}_0, a_n, b_n$	Fourier coefficients, Eq. (6.3)
U_∞	free stream velocity
U_{Blas}	velocity based on Blasius laminar boundary layer velocity profile
V_e	effective velocity
$\tilde{V}$	magnitude of the velocity vector
x, y, z	streamwise, normal, and spanwise coordinates
y^+	normal coordinate in viscous wall layer $\left(=yu_\tau/v\right)$
$y(\kappa_{u,\max})$	normal coordinate of the location where $\kappa_{u,\max}$ occurs

Greek Symbols

α	wave number $\left(=2\pi/\lambda\right)$
	yaw angle, Section (3.3)
$\bar{\alpha}$	mean yaw angle, Section (3.3)
β, β_o	amplification rate of perturbations

δ	boundary layer thickness
δ_L	Blasius laminar boundary layer thickness
δ^*	boundary layer displacement thickness
η	dimensionless coordinate normal to the wall $\left(= y\sqrt{U_\infty / xv}\right)$
θ	boundary layer momentum thickness
θ_L	Blasius laminar boundary layer momentum thickness
κ_u	vortex or disturbance amplitude, Eq. (4.1)
$\kappa_{u,\max}$	maximum disturbance amplitude
λ	wavelength of Görtler vortices
λ_m	the most amplified wavelength Görtler vortices
Λ	dimensionless wavelength parameter, Eq. (2.2)
μ	fluid dynamic viscosity
v	fluid kinematic viscosity
ρ	fluid density
τ_w	wall shear stress, Eq. (7.1)
ω	dimensionless wave number $\left(= \alpha\theta\right)$

CHAPTER 1

INTRODUCTION

1.1 Background

Flow instability may occur due to the dynamical effects of rotation or of streamline curvature. This instability is related to the occurrence of centrifugal force associated with the change of direction of fluid motion. The force decreases from the outer layer of boundary layer towards the wall, and consequently the fluid particles are pushed towards the wall. If a fluid particle is inflected from its equilibrium position due to the disturbances in the flow, then it will move to the zones of lesser or greater centrifugal force. Its movement is reinforced further downstream resulting in an amplification of the instability.

The examples of flows which exhibit this type of centrifugal instability are Couette flow in two rotating coaxial cylinders, flow in a curved channel, and concave surface boundary layer flow. The instability observed in Couette flow in two rotating coaxial cylinders leads to a steady secondary flow in the form of toroidal vortices, known as Taylor vortices, which are regularly spaced along the axis of the cylinders (Taylor, 1921). A similar type of instability can also occur in a curved channel flow due to the pressure gradient acting round the channel. Such flow may cause the occurrence of the so-called Dean vortices (Dean, 1928). Lastly, the centrifugal instability that occurs in a concave surface boundary layer flow may form streamwise counter-rotating vortices called Görtler vortices, after Görtler (1940) who was the first to analytically show the occurrence of these vortices, as shown in Fig. 1.1.

These vortices occur due to the imbalance between radial pressure gradient

and centrifugal forces in a concave surface laminar boundary layer flow. The vortices will be amplified downstream resulting in three-dimensional boundary layer which gives rise to spanwise variation of streamwise velocity, as well as boundary layer thickness. A thicker boundary layer is formed when low momentum fluid moves away from the surface, which results in lower shear stress region. This region is called upwash. Meanwhile, a thinner boundary layer is formed when high momentum fluid moves towards the surface resulting in higher shear stress region. This region is called downwash.

The study of Görtler vortex boundary layer flow may be useful in some engineering applications, such as compressor blades (Peerhossaini, 1984; Shigemi *et al*., 1987), airfoils (Mangalam *et al*., 1985; Dagenhart and Mangalam, 1986), and heat transfer enhancements (McCormack *et al*., 1970; Syred *et al*., 2001), in which the wall shear stress becomes an important aspect to consider.

1.2 Motivation

The motivation of the present work is to further investigate the development of the most amplified wavelength Görtler vortices pre-set by a set of vertical thin perturbation wires in a concave surface boundary layer flows. Pre-setting the vortex wavelength is to overcome the non-uniformity of vortex wavelength in naturally developed Görtler vortices and hence the vortex growth rate. This will provide a more objective analysis of the development of Görtler vortices. The present work will be carried out on a concave surface of radius of curvature R of 1.0 m. In addition to mean and fluctuating velocity measurements, near wall velocity measurement will also be performed to obtain wall shear stress data. These experimental data will be useful for comparison with future analytical or numerical study of Görtler instability. The

spanwise velocity component *w*, which has hardly been reported in the literature, will also be measured in the present work to study its role in the development of Görtler vortices.

1.3 Objectives and Scope

The main objective of the present work is to experimentally investigate the characteristics of concave surface boundary layer in the presence of uniform wavelength Görtler vortices. The more specific objectives are listed in the following.

1. To study the linear and nonlinear developments of Görtler vortices. The developments of the vortices are presented in their mean and fluctuating velocity distributions, shear-stress distributions, and amplification parameters of the vortex growth.
2. To investigate the effect of curvature by comparing the present results for $R = 1.0$ m with the previously reported results for different concave surface radii of curvature.
3. To identify the secondary instability modes in the nonlinear region of Görtler instability. Spectral analysis will be performed to obtain the characteristic frequencies of the secondary instability.
4. To study the development of the spanwise velocity component *w* in the nonlinear region of Görtler vortices. The *X*-wire will be used to measure the streamwise and spanwise velocity components.
5. To study the effect of Görtler instability on the development of wall-shear stress in concave surface boundary layer flow by performing near-wall velocity measurement. Near-wall velocity gradient technique will be utilized to estimate the mean wall-shear stress.

The present study will focus on uniform wavelength Görtler vortices pre-set by a series of vertical thin perturbation wires placed prior and perpendicular to the leading edge of a concave surface. The growth and breakdown of the vortices will be investigated for three different cases of free-stream velocities and wire spacings which correspond to the most amplified wavelength Görtler vortices.

1.4 Organization of Thesis

This thesis documents the experimental results and analyses on most amplified wavelength Görtler vortices. It is organized into 9 chapters as briefly outlined in the following.

The background, motivation, objectives and scope of the present study is presented in Chapter 1, while an extensive literature review on the development of Görtler vortices and wall shear stress along concave surface boundary layer flows is presented in Chapter 2. The experimental setup, instrumentations, and experimental procedures are described in Chapter 3.

The experimental results and discussions are presented in the next four chapters. Chapter 4 presents the linear and nonlinear developments of Görtler vortices for three different cases. The mean and fluctuating streamwise velocity components, as well as the quantitative measurement of vortex growth rate, are discussed in this chapter. The flow characteristics in the nonlinear region of Görtler vortices, which correspond to the appearance of the secondary instability, are discussed further in Chapter 5, together with the spanwise harmonics of streamwise velocity and the frequency characteristics of Görtler vortices. The flow characteristics related to the spanwise velocity component in the nonlinear region of Görtler vortices are presented in Chapter 6, while the development of wall shear stress in the presence of Görtler

vortices is presented in Chapter 7. Near-wall velocity gradient technique is introduced to estimate the wall-shear stress from the near-wall velocity data. The substantial increase of wall shear stress in the nonlinear region of Görtler vortices are also highlighted in Chapter 7.

Finally, the main conclusions and the recommendations for the future work are given in Chapter 8.

CHAPTER 2

LITERATURE REVIEW

2.1 Growth and Breakdown of Görtler Vortices

The characteristics of concave surface boundary layer flow are very different from those of the flat plate due to the presence of centrifugal instability which manifests itself into streamwise counter-rotating vortices, called Görtler vortices (Görtler, 1940). Such vortices will occur if the non-dimensional parameter Görtler number G_θ, as defined by Smith (1955):

$$G_\theta = \frac{U_\infty \theta_L}{v}\sqrt{\frac{\theta_L}{R}} \tag{2.1}$$

exceeds a critical value (where v is the fluid kinematic viscosity, θ_L the Blasius boundary layer momentum thickness, U_∞ the free-stream velocity, and R the concave surface radius of curvature).

Many attempts had been made to establish a unique critical number in the early stage of Görtler instability study. Different neutral curves from different Görtler instability models had been suggested (Görtler, 1940; Smith, 1955; Herbert, 1979; Floryan and Saric, 1982; Hall, 1983; Finnis and Brown, 1989). Floryan and Saric (1982) found that the neutral curve appears to asymptotically level off at $G_{\theta,cr}$ = 0.4638 which can be considered as a critical value. Finnis and Brown (1989) found that the minimum point of the unstable region occurs at G_θ = 1.38 and dimensionless wave number $\omega = 2\pi\theta/\lambda$ = 0.28 (where θ is boundary layer momentum thickness and λ Görtler vortex wavelength), while Kottke and Mpourdis (1986) did not detect any sign of instability when the screens that act as a source of disturbance were placed

sufficiently far upstream. More recently, Mitsudharmadi *et al*. (2004) observed the appearance of forced wavelength Görtler vortices at G_θ = 2.39. These results show that the existence of a unique neutral curve in real developing boundary layer becomes questionable. Hall (1983) showed that the position of neutral stability curve depends on how and where the boundary layer is perturbed. This finding implies that the concept of a unique neutral curve does not apply in the Görtler instability problem, except for asymptotically small wavelengths. Hence, the work on Görtler instability is focused more on the development of the vortices rather than on the attempt to find a unique neutral curve.

It is generally believed that the onset and development of Görtler vortices is influenced by the initial disturbances. Denier *et al*. (1991) addressed this issue by considering the vortex induced by wall roughness. It was found that free-stream disturbances are more important in generating the vortex modes than isolated wall roughness (Denier *et al*., 1991; Bassom and Hall, 1994). However, the distributed forcing disturbances are likely to be more important receptivity mechanism than the two disturbances mentioned earlier (Bassom and Hall, 1994). Hall (1989) used a model of a free-stream longitudinal vortex impinging on the leading edge of a curved surface as initial conditions to theoretically investigate the leading-edge receptivity problem. It was found that the leading-edge receptivity also has a strong effect in determining the flow structures.

In addition to the receptivity process, the wavelength selection mechanism of Görtler instability is also not clearly understood yet. It appears that a competition of perturbations of different amplification rates is the only wavelength selection mechanism of Görtler vortices (Floryan, 1991). The Görtler instability will amplify the disturbances imposed by the rig facilities of the incoming flow (Kottke, 1988) and

at the same time damp other weak disturbances in the flow. Therefore, the observed vortices in the experiments correspond to the most amplified disturbances according to the linear theory (Bippes, 1978). If the disturbances' wavelength introduced into the flow does not correspond to the most amplified wavelength Görtler vortices, splitting or merging of Görtler vortices will occur in the nonlinear region (Mitsudharmadi *et al*., 2005b).

A simple method based on the Görtler vortex stability diagram can be used to predict the most amplified wavelength Görtler vortices. In this method, the non-dimensional wavelength parameter Λ is defined as:

$$\Lambda = \frac{U_\infty \lambda_m}{\nu} \sqrt{\frac{\lambda_m}{R}} \tag{2.2}$$

where λ_m is the most amplified wavelength Görtler vortices. A constant Λ represents a family of straight lines which cross the Görtler vortex stability diagram. The most amplified wavelength Görtler vortices occurs when the non-dimensional wavelength parameter Λ is in the range of 220-270 (Meksyn, 1950; Smith, 1955; Floryan, 1991; Bottaro *et al*., 1996; Luchini and Bottaro, 1998; Mitsudharmadi, 2004 and 2006).

Early experiments on Görtler vortices were conducted for naturally developed Görtler vortices (Liepmann, 1943; Tani, 1962; Wortmann, 1969; Bippes, 1978; Winoto and Crane, 1980; Swearingen and Blackwelder, 1987; Finnis and Brown, 1989 and 1997). Liepmann (1943) investigated the effect of wall curvature on the boundary layer transition and found that a concave curvature decreased the critical Reynolds number, that is, the transition point occurred earlier than that in a flat plate boundary layer, although there was no significant effect of the curvature on the mean velocity profile. The development of transition downstream of Görtler vortices was visualized by Wortmann (1969) by tellurium method. Another instability mode,

consisting of regular three-dimensional oscillations, was observed following the steady vortex pattern. Later, Winoto and Low (1989, 1991) experimentally confirmed that the transition was started at the upwash at $G_\theta \approx 7.5$ by means of hot-wire anemometer measurements.

It is evident that a primary instability in concave surface boundary layer flow first occurs in the form of Görtler vortices with the wavelengths depending on the boundary layer thickness and the wall curvature (Bippes, 1978). Following the primary Görtler instability, periodic spanwise vorticity concentrations develop at the upwash. Meandering of the vortices subsequently takes place prior to turbulence. Similar mechanism of the growth of forced wavelength Görtler vortices was reported by Mitsudharmadi *et al*. (2004) who found that the development of the vortices can be divided into three regions, namely linear region, nonlinear region, and decay of the mushroom structures. Each region is characterized by the growth rate of the disturbances which is clearly shown by the slope of the curve in the graph of the maximum disturbance amplitude $\kappa_{u,\max}$ versus the streamwise location (Winoto and Crane, 1980; Finnis and Brown, 1989).

Detailed comparison between experimental results on the linear growth of Görtler vortices and the normal-mode linear stability analysis was carried out by Finnis and Brown (1997). The measured growth rates were considerably lower than those obtained from the theory due to the limitations of the normal-mode analysis. It was also suspected that the experimental data may not lie on the maximum amplification line in the Görtler vortex instability chart.

Swearingen and Blackwelder (1987) experimentally studied naturally developed Görtler vortices and observed a strong inflectional streamwise velocity profiles in both the normal and spanwise directions at nonlinear state of instability,

indicating the lower-momentum fluid riding over the higher-momentum fluid, at the upwash. The secondary instability observed in the nonlinear region was found to be more related to the inflectional velocity gradient in the spanwise direction than to the normal gradient of the streamwise velocity. It was noticed from a stronger correlation between the r.m.s. fluctuations with $\partial u/\partial z$ than with $\partial u/\partial y$. The growth rate of the secondary instability in term of the r.m.s fluctuations was found to be much faster than that of the primary Görtler instability.

Several modes of secondary instability associated with the non-linear development of Görtler vortices have been experimentally observed. Wortmann (1969) identified a secondary instability in the form of twisted interfaces between the longitudinal vortices. However, this mode has not been reproduced by other researchers. Bippes (1978) perceived a meandering or sinuous mode of the longitudinal vortex street in the disturbed flow along a concave surface. This mode seems to be correlated with the unstable inflectional spanwise profiles of streamwise velocity (Swearingen and Blackwelder, 1987) and be responsible for the low frequencies in the power spectra. Aihara and Koyama (1981) observed the formation of the so-called “horseshoe” vortices as a result of interaction between the primary Görtler vortices and Kelvin-Helmholtz instability. This mode of instability is also known as varicose mode which gives rise to higher frequencies in the power spectra. Both sinuous and varicose modes are believed to be responsible for the transition process prior to turbulence in concave surface boundary layers.

The dominant mode in transition process leading to turbulence has not been clearly understood. Peerhossani and Bahri (1998) measured the spanwise and normal gradients of the streamwise velocity and found that the spanwise gradient $\partial u/\partial z$ grew faster than the normal velocity gradient $\partial u/\partial y$. This implies that the sinuous mode

dominates the transition process prior to turbulence. Similarly, Mitsudharmadi *et al*. (2005a) also showed that the secondary instability was of the varicose mode at the onset, and followed by the sinuous mode downstream prior to turbulence. These findings were also supported by the computational studies of Yu and Liu (1991) and Sabry and Liu (1991). However, Matsson (1995), who investigated the secondary instability of streamwise vortices in curved wall jet, detected only the horseshoe varicose mode of oscillation which leads the flow to turbulence. The same result was also reported by Aihara and Koyama (1981). Hall and Horseman (1991) computationally found that the dominant mode depends on several parameters such as: history of the vortex, wavelength parameter, and Görtler number. This finding was supported by Park and Huerre (1995) who found that the varicose mode is dominant in the case of large wavelength vortices while the sinuous mode is dominant in the case of small wavelength vortices.

Recently, Girgis and Liu (2006) investigated the evolution of the single fundamental sinuous mode of secondary instability of longitudinal vortices and compared their numerical results with the experimental results of Swearingen and Blackwelder (1987) and Mitsudharmadi *et al*. (2004). It was found that the relevant part of comparison is limited to $G_\theta = 7.5$ where the secondary instability in the experiment is still dominated by the sinuous mode. For $G_\theta > 7.5$, the maximum of the r.m.s of fluctuating component $u' - \text{rms}$ obtained by Mitsudharmadi *et al*. (2004) lies beyond the numerical results (Girgis and Liu, 2006) which only considered a single fundamental sinuous mode. It was suspected (Girgis and Liu, 2006) that other modes of instability or transition to turbulence might have appeared.

Li and Malik (1995) described the development of Görtler vortex secondary instability. It was shown that the dominance of the sinuous (odd) and varicose (even)

modes were affected by the Görtler vortex wavelength. For the short-wavelength $(\lambda = 0.9 \text{ cm})$, the Görtler vortices grow faster and the odd mode secondary instability start to appear at the location where the amplitude of the Görtler vortices is about 20%. For the medium wavelength $(\lambda = 1.8 \text{ cm})$, the odd mode is the first to become unstable. Subsequently, the even mode takes over and becomes the most unstable mode further downstream. For the long wavelength $(\lambda = 3.6 \text{ cm})$, the dominant mode is initially the odd mode, but it is very weak. Thus, before the odd mode growth rate becomes significantly large, the even mode begins to dominate.

2.2 Wall Shear Stress in the Presence of Görtler Vortices

2.2.1 Wall shear stress measurement

The techniques available to measure wall shear stress have been discussed by Winter (1979) and Hanratty and Campbell (1983), for example. A brief description on the use of hot-wire to measure streamwise velocity near a wall in order to estimate the wall shear stress is provided here.

Hot-wire or hot-film velocity measurements in the viscous sublayer to estimate the wall shear stress in turbulent boundary layer are generally associated with large methodological problems in the inner portions of the viscous sublayer. The setback is that the velocity in the sublayer is relatively small, and the heat loss due to free convection from the hot-wire or hot-film may give rise to erroneous readings. However, the hot-wire measurements in the viscous sublayer have been reported, for example by Bhatia *et al*. (1982), Alfredsson *et al*. (1988), and Chew *et al*. (1994). Alfredsson *et al*. (1988) measured the fluctuating wall shear stress with various types of hot-wire and hot-film sensors in turbulent boundary layer and channel flows. The mean wall shear stress in the oil channel was found to be accurately determined from

mean velocity measurements in the viscous sublayer. Chew *et al*. (1994) also successfully predicted the mean wall shear stress by means of the hot-wire with its active element positioned just above the wall within the viscous sublayer.

Another problem is related to the small thickness of the viscous sublayer so that the probe may cause significant aerodynamic interferences to the flow. The length (l) of the active hot-wire element has to be sufficiently large to achieve a length to diameter (l/d) ratio greater than 200 (Blackwelder and Haritonidis, 1983; Ligrani and Bradshaw, 1987b). On the other hand, l has to be sufficiently small to avoid the spatial resolution problems. Ligrani and Bradshaw (1987a) showed that the turbulence intensity, flatness factor, and skewness factor of the streamwise velocity fluctuations are independent of wire length as long as the non-dimensional wire length $l^+ (= l u_\tau / \nu)$ does not exceed 20-25.

2.2.2 Wall shear stress development

The appearance of streamwise counter-rotating Görtler vortices in nonlinear region will cause the friction drag to increase, especially when the secondary instability appears in the boundary layer. Although it gives unfavorable effects for the blades and airfoils, the increase of the wall shear stress and hence the heat transfer coefficient through Reynolds analogy may be useful in a thermal system. McCormack *et al*. (1970) reported a 100-150% increase in Nusselt number on concave surface boundary layer due to the presence of Görtler vortices, compared to that on a flat-plate boundary layer. Liu (2008) explained this enhancement of the heat transfer as a result of transport effects of the nonlinear secondary instability, which leads to the formation of vortex structures in the flow. Momayez *et al*. (2009) proposed an

algorithm for calculation of heat transfer enhancement in a concave surface boundary layer flow.

Swearingen and Blackwelder (1987) estimated the skin friction on a curved wall from the streamwise velocity profiles across boundary layer obtained by hot-wire anemometer measurements. It was found that the wall shear stress at downwash increases considerably at a streamwise (x) location until reaching a maximum value. Meanwhile, the wall shear stress at upwash decreases faster than that calculated from Blasius solution, and then increases after reaching a minimum value. Further downstream, the wall shear stress at both upwash and downwash move towards the same value.

The increase of wall shear stress in the nonlinear region of Görtler instability has also attracted attention of some theoreticians (Sabry and Liu, 1991; Hall and Horsemann, 1991; Girgis and Liu, 2006). The computational results of Sabry and Liu (1991), who studied the nonlinear effects of Görtler vortices via a prototype problem, showed good qualitative agreement with the measurement of Swearingen and Blackwelder (1987). Hall and Horseman (1991) also managed to approximate the Swearingen and Blackwelder's results up to a certain streamwise distance through the study of the linear inviscid secondary instability of Görtler vortices. Recently, Girgis and Liu (2006) focused on the nonlinear modification of the steady flow by the Reynolds stresses of the wavy disturbance, and found that the wall shear stress increased well beyond the local turbulent values as the flow developed downstream due to the presence of the secondary instability modes.

CHAPTER 3

EXPERIMENTAL DETAILS

3.1 Experimental Set-up

The experiments were conducted in a 90° curved plexiglass duct connected to a low speed, blow down type wind tunnel as also used by Mitsudharmadi *et al*. (2004) and shown in Fig. 3.1. The wind tunnel has a rectangular cross-section of 150 mm x 600 mm. The flow control was achieved by placing a honeycomb and five rectangular fine-mesh screens with decreasing mesh-sizes in the settling chamber prior to the contraction. The screens have the specification of ASTM E161 No. 35, 40, 50, 60, and 80 with the mesh-size of 500, 425, 300, 250, and 180 μm, respectively from the blower to the entrance of the contraction section. The contraction consists of a 300 mm straight channel of 600 mm × 600 mm cross-section followed by a two-dimensional contraction of 4:1 which reduces the cross-section to 150 mm x 600 mm.

A concave surface of radius of curvature R = 1.0 m was mounted inside the curved duct by means of slots at the duct side walls at a distance of 50 mm from its bottom surface. The distance between the concave surface and its top cover is 100 mm giving an aspect ratio of the test section of 6. The wind tunnel and the curved duct are connected by a straight channel of 150 mm length. The concave surface has a sharp leading edge with an angle of 45° to avoid flow separation. The free-stream turbulence levels in the test section are less than 0.45% for free-stream velocity range of 1.0 to 4.0 m/s.

A series of vertical perturbation wires of 0.2 mm diameter were positioned 10 mm prior and perpendicular to the concave surface leading edge to pre-set or to

"force" the wavelength of Görtler vortices. The spanwise spacing between the wires, which was found to be λ_m, and the free-stream velocity U_∞ were determined so that the wavelength parameter Λ = 250 [Eq. (2.2)], which corresponds to the most amplified wavelength λ_m of Görtler vortices, as also used by Mitsudharmadi *et al*. (2004).

Using Eqn. (2.2), three different cases of the most amplified wavelengths were considered in the present study: (1) λ_m = 12 mm, for which the corresponding U_∞ = 2.8 m/s, (2) λ_m = 15 mm, for which U_∞ = 2.1 m/s, and (3) λ_m = 20 mm, for which U_∞ = 1.3 m/s.

3.2 Instrumentations

The measurement process (including data acquisition) and the traversing mechanism were automatically controlled by a personal computer. The block diagram of the hot-wire anemometer system and other instruments used in the experiments is shown in Fig. 3.2. The detailed description of the instruments and the process are given below.

3.2.1 Hot Wire Anemometer and Sensors

A single-normal (*SN*) hot-wire probe (Dantec 55P15) and a cross (*X*) hot-wire probe (Dantec 55P61) of special design for boundary layer measurement with a 5 μm diameter and 1.25 mm long platinum-plated tungsten wire sensors were used to obtain mean and fluctuating velocities data. The *SN*-probe was used to obtain streamwise velocity in all cases, including near-wall velocity measurements, while the *X*-probe was used to measure streamwise and spanwise velocities in the nonlinear region of case 1 (λ_m = 12 mm, U_∞ = 2.8 m/s). The probes were operated in a Constant

Temperature Anemometer (CTA) mode by connecting them to a CTA system which consists of 56C01 CTA Main Frame, 56C17 CTA Bridge, and 56N20 Signal Conditioner. Overheat ratio of 1.8 was used throughout the experiment.

A Pitot-static tube, connected to a pressure transducer (Setra 235, 0-0.1 psid), was placed in the free-stream region and moved together with the hot-wire probe. It was used to calibrate the hot-wire(s) and to monitor the free-stream velocity.

A *T*-type thermocouple, connected to Agilent 34970A Data Acquisition / Switch Unit equipped with 34901A 20-Channel Multiplexer, was also mounted on the traversing mechanism and moved together with hot-wire probe and Pitot-static tube to measure the free-stream temperature. The temperature data were sent to the computer through RS-232 cable. It was then used to compensate the hot-wire voltage readings due to the change in ambient temperature during the hot-wire calibration and measurements.

A digital oscilloscope (Yokogawa DL1540) and multimeter (Keithley Model 2000) were respectively used to monitor the output of CTA system and pressure transducer during the measurement process.

The traverse mechanism control system was used to control the movement of sensors. The system consists of two linear slides which can move in the normal (y) and spanwise (z) directions by means of a stepper-motor installed on each slide. The mechanism allows the sensors to be moved in a step of 0.005 mm.

3.2.2 Data Acquisition System

Analog signals from the CTA system and pressure transducer were directly sent to analog to digital (A/D) data converter system. The system consists of a high-speed multifunction DT3016 board and DT740 screw terminal panel. The board has

an analog I/O resolution of 16 bits with a maximum sampling frequency of 250 kHz for a single channel. The system also has a capability to send a digital signal with a maximum D/A throughput of 100 kHz. This feature allows us to control the movement of stepper motors from the computer.

Agilent VEE Pro software was used for collecting data and controlling the measurement process from the computer, including the movement of stepper motors. It was also used in the post-processing of experimental data, such as a Fast Fourier Transform to obtain the spectra of the fluctuating velocity components. VEE programs were created by this software to provide visual interfaces in controlling data acquisition hardware.

3.3 Experimental Procedures

The CTA system was adjusted prior to its calibration and the subsequent experiments to ensure that the square-wave response at a maximum velocity expected in the experiments is greater than the sampling rate of the hot-wire signal of 6000 Hz.

Basically, the experiments were divided into three major parts: (a) measurement of mean and fluctuating streamwise velocities by *SN*-probe, (b) near-wall velocity measurement for estimating wall shear stress, and (c) streamwise and spanwise velocities measurement by *X*-probe to investigate the nonlinear development of spanwise velocity w, as well as the spectrum characteristics, in the nonlinear region of Görtler vortices. The detail of the experimental procedures is given below.

3.3.1 Calibrations

In-situ calibration of the hot-wire anemometer was carried out prior to the velocity measurement. The hot-wire anemometer was calibrated against a pressure

transducer which was connected to a Pitot-static tube. The pressure transducer was calibrated against a micro-manometer. The hot-wire calibration was based on the King's Law with temperature compensation. It was accomplished in free-stream flow over the range of velocities encountered within the boundary layer.

3.3.1.1 *SN*-probe calibration

The Pitot-static tube and hot-wire probe were positioned in the free-stream region at the same streamwise (x) location. The output signals from both pressure transducer and CTA system were then sampled simultaneously. The pressure transducer signal was sampled at 500 Hz and the hot-wire signal was low-pass filtered at 3000 Hz and sampled at 6000 Hz for 21 seconds. The voltage output of pressure transducer was converted into free-stream velocity data.

The relationship between the free-stream velocity U_∞ and the voltage output of CTA system E is assumed to follow King's law,

$$E^2 = AU_\infty^{0.45} + B \tag{3.1}$$

where A and B are calibration constants. By taking into account the ambient temperature drift, Eq. (3.1) can be modified into

$$E^* = \frac{E^2}{T_w - T_a} = A'U_\infty^{0.45} + B' \tag{3.2}$$

where T_w is the hot-wire temperature, T_a the ambient temperature, A' and B' are the temperature compensated calibration constants. The hot-wire temperature was determined based on the overheat ratio used in the measurement. The free-stream velocity data were then plotted against E^*, and linear regression was performed to obtain the calibration constants A' and B'. Calibration check was subsequently

carried out for the operating free-stream velocity to ensure that the calibration error was less than 1.0%.

3.3.1.2 *X*-probe calibration

The main purpose of utilizing *X*-probe was to capture the spanwise oscillation of low-speed streaks in the nonlinear region of Görtler vortices. The oscillation frequency is likely to be of the same order as the characteristic frequencies of streamwise velocity *u* or even lower. Therefore, the sampling frequency of the hot-wire and pressure transducer signals in the calibration and measurement were reduced to 600 Hz for 30 seconds. The hot-wire signals were low-pass filtered at 300 Hz prior to sampling.

The calibration of the *X*-probe was carried out by using V_e-calibration methods, in which each wire in *X*-probe is considered independently. By extending King's Law for *X*-probe, Eq. (3.1) can be written as:

$$E^2 = A + BV_e^{0.45} \tag{3.3}$$

where the effective velocity V_e can be expressed as:

$$V_e = \tilde{V} f(\alpha) \tag{3.4}$$

where $f(\alpha)$ is the yaw function and $\tilde{V}$ the magnitude of the flow vector. Several expressions have been proposed for the yaw function. The most common method, as proposed by Hinze (1959), was used in the present experiments, that is,

$$f(\alpha) = \left(\cos^2\alpha + k^2 \sin^2\alpha\right)^{1/2} \tag{3.5}$$

where *k* is the yaw coefficient and α the yaw angle. By substituting Eq. (3.4) into Eq. (3.3), the hot-wire response equation becomes

$$E^2 = A + B\left[f(\alpha)\tilde{V}\right]^{0.45} = A + \hat{B}(\alpha)\tilde{V}^{0.45} \tag{3.6}$$

with $\hat{B}(\alpha)$ defined by

$$\hat{B}(\alpha) = B\left[f(\alpha)\right]^{0.45} \tag{3.7}$$

In the calibration, *X*-probe was positioned normal to the free-stream at the mean yaw angles $\bar{\alpha}_1$ and $-\bar{\alpha}_2$, where $\bar{\alpha}_1 = \bar{\alpha}_2 = \bar{\alpha} = 45°$. The correction for ambient temperature drift was subsequently applied in Eq. (3.6). Hence, the hot-wire response equations for both wires become

$$E_1^* = \frac{E_1^2}{T_w - T_a} = A_1' + \hat{B}_1'(\bar{\alpha})U_\infty^{0.45} \tag{3.8a}$$

$$E_2^* = \frac{E_2^2}{T_w - T_a} = A_2' + \hat{B}_2'(-\bar{\alpha})U_\infty^{0.45} \tag{3.8b}$$

The velocity calibration at $\bar{\alpha}$ will give the calibration constants $A_1', B_1'(\bar{\alpha})$ and $A_2', B_2'(\bar{\alpha})$ for both wires. Since $B'(\bar{\alpha})$ contains two unknowns, *B* and $f(\bar{\alpha})$, yaw calibration is necessary to obtain the yaw coefficient $k(\bar{\alpha} = 45°)$. The value of $k(45°)$ for plated-probe with parallel-stem orientation is 0.15-0.20 (Brunn, 1995). A constant value $k(45°) = 0.2$ was used in the present experiments.

Calibration check was performed regularly after each measurement across boundary layer (± 15 minutes) to make sure that the calibration error was less than 0.5%.

3.3.2 Measurement of Mean and Fluctuating Streamwise Velocities

The mean and fluctuating streamwise velocities were measured by means of *SN*-probe. In the measurement process, the hot-wire signal was low-pass filtered at 3000 Hz and sampled at 6000 Hz for 21 seconds. The output voltage of CTA system was subsequently converted into velocity data by interpolation of the calibration

points. Calibration checks were regularly performed to ensure that the drift is within an acceptable range of ±1%, otherwise the data obtained were rejected, resulting in a re-calibration of the hot-wire.

The instantaneous velocity $\hat{u}$ obtained from the hot-wire measurement can be expressed as:

$$\hat{u} = u + u' \tag{3.9}$$

where u is the mean velocity and u' is the fluctuating velocity component. The mean velocity is obtained by time-averaging the sampled data, which is calculated as:

$$u = \frac{1}{n}\sum_{i=1}^{n}\hat{u}_i, \quad i = 1, 2, \cdots, n \tag{3.10}$$

where n is the total number of samples of velocity data within the sampling duration at a given point. The fluctuating velocity component is expressed in the turbulence intensity Tu, which is obtained from:

$$Tu = \frac{1}{u}\sqrt{\frac{\sum_{i=1}^{n}\left(\hat{u}_i - u\right)^2}{n}}, \quad i = 1, 2, \cdots, n \tag{3.11}$$

The above procedures were repeated at every point of the measurement domains.

The measurements of streamwise velocity component were carried out at several streamwise (x) locations. Five pairs of vortices were captured by the hot-wire measurement with 1.0 mm traversing step along the spanwise (z) direction and 0.5-1.0 mm step along the normal (y) direction inside boundary layers. Mean streamwise velocity contours were then plotted to determine the locations of the upwash and downwash regions. Subsequently, the velocity profiles were obtained by measuring the streamwise velocity across the boundary layer at those locations with 0.5 mm step. The measurements were carried out for all three cases considered in the present work.

3.3.3 Velocities Measurement Using Cross (*X*) Hot Wire Probe

The *X*-probe was used to measure the streamwise and spanwise velocity components in the nonlinear region of Görtler vortices. The hot-wire signals were low-pass filtered at 300 Hz and sampled at 600 Hz for 30 seconds. Three pairs of vortices were captured with 1.0 mm traversing step along both spanwise (z) and normal (y) directions. The measurement was carried out in nonlinear region of case 1 (λ_m = 12 mm, U_∞ = 2.8 m/s).

The signal analysis was carried out by applying a simple sum-and-difference method. The streamwise and spanwise velocity components were respectively obtained from equations:

$$u = \frac{V_{e1} + V_{e2}}{2 f(\bar{\alpha})} \tag{3.12a}$$

$$w = \frac{V_{e2} - V_{e1}}{2 f(\bar{\alpha}) g(\bar{\alpha})} \tag{3.12b}$$

where V_{e1}, V_{e2} are the effective velocities and $f(\bar{\alpha})$, $g(\bar{\alpha})$ are the yaw functions. The effective velocity was obtained from data conversion of the measured voltage output of the CTA system. It was calculated by using the inverted calibration relationship:

$$V_{e1} = \left(\frac{E_1^* - A_1'}{B_1'} \right)^{1/0.45} \quad \text{and} \quad V_{e2} = \left(\frac{E_2^* - A_2'}{B_2'} \right)^{1/0.45} \tag{3.13}$$

where B_1' and B_2' are calculated from Eq. (3.7),

$$B_1' = \frac{\hat{B}_1'(\bar{\alpha})}{\left[f(\alpha) \right]^{0.45}} \quad \text{and} \quad B_2' = \frac{\hat{B}_2'(\bar{\alpha})}{\left[f(\alpha) \right]^{0.45}} \tag{3.14}$$

The yaw functions are given by

$$f(\bar{\alpha}) = \left(\cos^2 \bar{\alpha} + k^2 \sin^2 \bar{\alpha} \right)^{1/2} \tag{3.15a}$$

$$g(\bar{\alpha}) = \frac{\left(1-k^2\right)\cos^2\bar{\alpha}}{\cos^2\bar{\alpha}+k^2\sin^2\bar{\alpha}}\tan\bar{\alpha} \tag{3.15b}$$

In addition to the mean velocity components *u* and *w*, other related fluid properties can also be evaluated, such as Reynolds stresses $\overline{u'^2}$, $\overline{u'w'}$, and $\overline{w'^2}$.

3.3.4 Near-wall Velocity Measurement

Basically, near-wall velocity measurement is identical with the streamwise velocity measurement (Section 3.3.2). The measurement was carried out by means of *SN*-probe to capture the region where the velocity profile is linear in order to estimate the wall shear stress. The signal was low-pass filtered at 3000 Hz and sampled at 6000 Hz for 21 seconds. The hot-wire probe was initially positioned very near to the concave surface with the aid of a camera. The streamwise velocity measurement was subsequently performed with the step size of 50 μm across the boundary layer for 40 points ranging from *y* equals 0.05 to 2.00 mm. Three pairs of vortices were captured in this near-wall streamwise velocity measurement with 2.0 mm traversing step along the spanwise direction. All three cases of different wavelengths were considered in this measurement.

CHAPTER 4

LINEAR AND NONLINEAR DEVELOPMENT OF GÖRTLER VORTICES*

4.1 Introduction

In most experiments of naturally developed Görtler vortices, each vortex pair develops with different growth rate which may affect the growth of the neighboring vortices, resulting in vortices with non-uniform wavelengths. This non-uniformity in wavelengths (and hence the vortex sizes) makes it difficult to objectively study the behavior of the vortices. In order to generate naturally developed Görtler vortices with as uniform wavelengths as possible, the oncoming flow has to be carefully controlled and the concave surface has to be perfectly smooth, as previously done by Wortmann (1969) in a curved water channel and Dagenhart and Mangalam (1986) on an airfoil.

To experimentally overcome this problem, the wavelength of Görtler vortices is pre-set or "forced" prior to the leading edge of the concave surface. Some methods have been suggested by introducing orderly disturbances at the concave surface leading edge. Aihara (1979) used a fine needle set at the gap in front of the leading edge and projected outward impulsively to give an artificial controlled disturbance. This method was also used by Tandiono *et al*. (2008a) who introduced a series of perturbation needles prior and perpendicular to the leading edge of the concave surface. Peerhossani and Bahri (1998) used a series of thin vertical wires placed prior and perpendicular to the concave surface leading edge. This method was also adopted by Ajakh *et al*. (1999), Toé *et al*.(2002), and Mitsudharmadi *et al*. (2004, 2005a,

* Parts of this Chapter have been published in *Physics of Fluids* (Tandiono *et al*., 2008b) and *Journal of Visualization* (Tandiono *et al*., 2009a).

2005b, 2006) since it could effectively generate Görtler vortices with uniform wavelengths equal to the pre-set spanwise spacing of the thin perturbation wires.

The work of Mitsudharmadi *et al*. (2004, 2005a, 2006) was on the most amplified wavelength Görtler vortices. The experiments were conducted on a concave surface of R = 2.0 m for only one set of wire-spacing and free-stream velocity which corresponds to the most amplified wavelength. Although some studies have suggested the range of wavelength parameter Λ, as defined by Eq. (2.2), for the most amplified wavelength Görtler vortices which will appear in experiments, only a few experimental findings are available to confirm this suggestion. In addition, more information is also required to better explain the growth and breakdown of the pre-set wavelength Görtler vortices.

This chapter discusses the linear and nonlinear development of the pre-set or "forced" wavelength Görtler vortices in the boundary layer on a concave surface of R = 1.0 m for three different cases of wires-spacing and free-stream velocity: (1) λ_m = 12 mm, for which the corresponding U_∞ = 2.8 m/s, (2) λ_m = 15 mm, for which U_∞ = 2.1 m/s, and (3) λ_m = 20 mm, for which U_∞ = 1.3 m/s. The results will also be compared with those obtained by Mitsudharmadi *et al*. (2004) who used a concave surface of R = 2.0 m.

4.2 Mean Velocity

Streamwise velocities were obtained across a spanwise distance covering five pairs of vortices, and the iso-contours of the mean (time-averaged) streamwise velocities were plotted on the y-z and x-z planes by using a commercial software TECPLOT with no smoothing performed for all the contours presented here. Basically, the mechanisms of the vortex structure development for the three cases are similar.

Figures 4.1 and 4.2 show the mean streamwise velocity contours for case 1 (λ_m = 12 mm and U_∞ = 2.8 m/s) on the *y*-*z* and *x*-*z* planes, respectively.

As shown in Fig. 4.1, the wavy profile generated by the vertical perturbation wires placed upstream near the concave surface leading edge becomes more visible further downstream. Low-momentum fluid at $z \approx \pm n\lambda_m$ (where n = 0, ±1, ±2, …) moves away from the wall to form low-speed regions called upwash with thicker boundary layer. Whereas, high-momentum fluid at $z \approx \pm(n + ½)\lambda_m$ moves towards the wall to form high-speed regions called downwash. The thickening of the boundary layer at the upwash makes the boundary layer at the downwash thinner. However, the decreasing rate of the boundary layer thickness at the downwash is lower than the increasing rate of the thickness at the upwash. This observation implies that the boundary layer at downwash is more resistant to the effects of curvature, and therefore the inflectional point, as expected, is first observed at the upwash which is the most unstable region.

Further downstream, the wavy profiles develop into horseshoe vortices at x = 300-400 mm, as shown in Figs. 4.1(c)-(d). The horseshoe structures propagate downstream and develop into mushroom-like structures. It is shown by the appearance of the small inflections at the sides of the stem of the vortices that move upward, lifting the head of the mushroom-like structures up. The inflection points in the velocity profile across boundary layer and the high-shear regions near the boundary layer edge are lifted up. Consequently, the support from the stem of the vortices to the mushroom-like structures' head becomes weaker so that the vortex structures are susceptible to the free-stream flow. Finally, the vortex's heads are dispersed and the flow turns into turbulence.

The development of the low-speed streaks for case 1 is shown in the velocity contours in the *x*-*z* planes at four different normal distances y/δ_L = 0.25, 0.50, 0.75, and 1.00, as shown in Fig. 4.2. At y/δ_L = 0.25, viscous effect is still very dominant in the linear region at both upwash and downwash so that the streamwise velocity is relatively very low. Downstream of $x \approx 350$ mm where $G_\theta \approx 4.9$, the viscous effect at the downwash becomes less significant compared to the effect of concave curvature. This can be seen from a considerable increase of the streamwise velocity component near that streamwise location. There is also an increase of velocity at the upwash, but it is not as large as at the downwash. The low-speed streaks become slightly narrower as the instability moves from linear to nonlinear at the location between x = 350 and 450 mm, as shown in Fig. 4.2(a). This is due to the formation of mushroom-like structures, that is, the horseshoe vortices are inflected at normal position near the wall surface resulting in thinner low-speed streak at y/δ_L = 0.25. Once the mushroom-like structures are fully formed, the width of the low-speed streaks at this normal (y) position will not change anymore. The narrowing of the low-speed streaks is also observed at y/δ_L = 0.50, as shown in Fig. 4.2(b), at the streamwise location slightly downstream from those at y/δ_L = 0.25, that is, between x = 400 and 500 mm. This indicates that the inflected parts of the vortex structures are moving upward as the flow moves downstream. In contrast to the narrowing of the low-speed streaks at y/δ_L = 0.25 and 0.50, the same streaks at y/δ_L = 0.75 and 1.00 are observed to broaden in the nonlinear region, as shown in Figs. 4.2(c) and 4.2(d), respectively. While the low-speed streaks at y/δ_L = 0.25 and 0.50 represent the stem of the vortex structures, the streaks at y/δ_L = 0.75 and 1.00 represent the head of the vortex structures. Therefore, the broadening of the streaks in the nonlinear region shows that

the vortex structures, which are dominated by the mushroom-like structures, expand side ways until they break into turbulent.

Figure 4.3 shows the downstream development of the streamwise velocity profile across boundary layer for case 1. The profiles presented here were obtained at the centers of the upwash and downwash and plotted in the graphs of u/U_∞ versus η, where $\eta\left(=y\sqrt{U_\infty/xv}\right)$ is the dimensionless coordinate normal to the wall. Velocity profiles of the Blasius flat plate boundary layer are also included for comparison. The maximum random error, apart from the calibration error (Section 3.3.2), in the measurement of u was estimated to be about 0.3%.

Initially, at x = 100 mm, the velocity profiles at upwash and downwash are very similar to the Blasius flat plate laminar boundary layer velocity profile. Further downstream, the velocity profiles at both upwash and downwash depart from the Blasius profile. As shown in Fig. 4.3, the velocity profile becomes "thinner" at the upwash and "fuller" at the downwash. The departure from the Blasius profile is slight in the linear region ($x < 300$ mm), but significant in the nonlinear region ($x > 300$ mm). Fuller velocity profile at the downwash shows an increase of wall shear stress, while thinner velocity profile at the upwash indicates a decrease of wall shear stress.

A single inflection point first appears in the velocity profile at the upwash near the boundary layer edge at x = 350 mm, which corresponds to the region where the intense turbulence is found in the turbulence intensity contour (Fig. 4.6). The appearance of the inflection point in the velocity profile implies the occurrence of high-shear layer near the boundary layer edge which triggers the appearance of horseshoe vortices as the secondary instability of Görtler vortices (Floryan, 1991). The viscous effect is relatively unimportant near the boundary layer edge where the

inflection point first appears (Swearingen and Blackwelder, 1987), hence the main force causing the instability is the centrifugal force.

As discussed earlier, the inflection point moves upward and the velocity profile defect increases as a consequence of the high-shear in that region. As the velocity defect grows progressively upward, a second inflection point appears in the region between the concave surface and the boundary layer edge, and the velocity profile evolves to become an **S**-shape, as shown at x = 500 mm in Fig. 4.3. Even though the second inflection point is not as obvious as the first one, it may be responsible for the transition process to turbulence. It can also be confirmed from the turbulence intensity (Tu) profile at the upwash, as shown in Fig. 4.6, where the highest peak is found between the concave surface and the boundary layer edge which is simply the location of the second inflection point in the velocity profile.

4.3 Shear Stress

Figure 4.4 shows the $\partial u/\partial y$ iso-shear contours at several streamwise (x) locations for case 1. In addition to the strong shear at the wall, there are other regions of strong positive shear, which indicates high-shear regions, appear near the boundary layer edge at the upwash. These high-shear regions rapidly move upward at x = 300 mm, as shown in Fig. 4.4(c), and followed by the formation of weak negative shear regions below the positive high-shear regions in the vicinity of the low-speed streaks of Fig. 4.2. These strong positive and weak negative shear regions are removed from the wall in the vicinity of the low-speed streaks (Bottaro and Klingmann, 1996) as a consequence of the net upward force at the upwash. The strong positive $\partial u/\partial y$ shear region seems to correspond to the first inflection point near the boundary layer edge (Fig. 4.3), while the weak negative shear region corresponds to the second inflection

point between the boundary layer edge and the concave surface. Excluding the strong shear region near the wall, three maxima are found in the shear contours: one positive peak at the head of the mushroom-like structures and two relatively weak negative peaks in the vicinity of the stem. Further downstream, the structures that are formed by the weak negative shear regions in the contours become unorganized. This coincides with the decay of the mushroom-like structures attributed to the increased mixing due to the onset of turbulence (Mitsudharmadi *et al*., 2006).

In addition to the inflection points in the normal direction which corresponds to the strong positive and weak negative $\partial u/\partial y$ shear regions, the velocity profile is also inflected along spanwise direction as depicted by the high-$\partial u/\partial z$ shear regions in the vicinity of the low-speed streaks, as shown in Fig. 4.5. Initially in the linear region, there are two peaks, which are symmetrical about the z-axis at the center of the iso-u mushroom structures, found in the contours for each vortex structure showing the concentration of the strong positive and negative $\partial u/\partial z$ shears. Further downstream, in the nonlinear region, the peaks are separated into two at x = 400 mm, as shown in Fig. 4.5(e). The first ones are close to the wall, while the others are near the boundary layer edge, and are called "turn-over" region (Bottaro and Klingmann, 1996) in which the secondary flow turns at this point and is directed towards the wall. Further downstream, the second peaks near the boundary layer edge decay as the flow reaches the location where the mushroom-like structures collapse prior to turbulence.

It is evident that the secondary instability of Görtler vortices is triggered by the high-shear layer formed near the boundary layer edge (Floryan, 1991). By comparing the contours of $\partial u/\partial y$ (Fig. 4.4) and $\partial u/\partial z$ (Fig. 4.5) shears with the turbulence intensity (Fig. 4.6) at the same streamwise locations, it is observed that the development of the intense regions of fluctuation in the turbulence intensity contour

seems to be more correlated with the contour of $\partial u/\partial z$ shear. The appearance of the second peaks of the $\partial u/\partial z$ shear is consistent with the intense regions of fluctuation that appear near the boundary layer edge in Fig. 4.6. These peaks seem to be the most unstable region in the flow that cause an increase of turbulence intensity due to direct energy conversion from the primary motion to the fluctuating component of kinetic energy (Yu and Liu, 1994). Subsequently, it enhances the development of the vortex structures from the wavy profile to the horseshoe and mushroom-like structures further downstream prior to turbulence. These unstable regions correspond to the inflectional spanwise profile of streamwise velocity u that is suspected to be responsible for the sinuous mode of secondary instability (Yu and Liu, 1991) in the form of oscillations of the low-speed streaks observed in the smoke-wire flow visualization (Swearingen and Blackwelder, 1987).

In contrast to the sinuous mode, in which the instability motions are the consequence of $\partial u/\partial z$ shear, the motions of the varicose mode are due to $\partial u/\partial y$. Hence, the intense regions of fluctuation are strongly related to the high-shear layers in iso-$\partial u/\partial y$ contours (Fig. 4.4) at the peak of the vortex structure and two smaller peaks on either side of the upper stem region of the vortex structure (Yu and Liu, 1994).

The iso-$\partial u/\partial y$ shear contours in Fig. 4.4 show high-shear regions at the peaks of the vortex structure or low-speed streaks to form "dome" regions. These indicate intense regions of fluctuations in the iso-Tu contours in Fig. 4.6 which appear as varicose mode. Although the maximum of this region is not clearly observed in the contours due to the dominance of the sinuous mode, its existence is shown by the appearance of the peaks in the turbulence intensity profile across boundary layer at the upwash (Fig. 4.7). The second peak appears near the boundary layer edge, exactly

in the high-shear region in iso-$\partial u/\partial y$ shear contour (Fig. 4.4), indicating the appearance of varicose mode of secondary instability.

4.4 Fluctuating Velocity

The fluctuating component of streamwise velocity u' for case 1 (λ_m = 12 mm and U_∞ = 2.85 m/s) is presented in term of turbulence intensity Tu [Eq. 3.11] for several streamwise (x) locations.

Figure 4.6 shows the streamwise development of turbulence intensity (Tu) contours in y-z plane. Upstream of x = 300 mm, the turbulence intensity is still relatively very low and the intense region of Tu have not been seen clearly. The structures of two symmetric intense regions of Tu begin to appear at the low-speed (upwash) region at x = 300 mm (Fig. 4.6(c)), and becomes more pronounce further downstream. These intense regions are found near the stem of the vortex structures. Another pair of intense region of Tu appears near the boundary layer edge at x = 400 mm, as shown in Fig. 4.6(e). The appearance of the second pair of intense regions, although the Tu is not as high as those found near the stem of the vortex structures, shows that another mechanism of instability appears in the boundary layer. Yu and Liu (1994) addressed this secondary instability as the sinuous mode which corresponds to the mushroom-like structures in the mean velocity contours (Fig. 4.1). The intense regions near the boundary layer edge become more visible further downstream to form a canopy structure covering the intense regions near the stem of the vortices. Both turbulence intensities near the stem of the vortices and of the boundary layer edge increase as the vortex structures grow upward and become more susceptible to the free-stream velocity. Transition to turbulence subsequently takes place as indicated by the significant increase of turbulence intensity in the range of x

= 700-800 mm.

The downstream development of turbulence intensity (*Tu*) profile across boundary layer for case 1 is shown in Fig. 4.7. The profiles were obtained at the centers of the upwash and downwash and plotted against η. The maximum random error in *Tu* was estimated to be about 0.4%.

Similar to *Tu* contours, there is no increase of *Tu* observed before x = 300 mm. The first peak of turbulence intensity in the profile is observed at x = 300 mm. At x = 350 mm, the second peak appears near the boundary layer edge, exactly in the high-shear region in iso-$\partial u/\partial y$ shear contour (Fig. 4.4). The peak further develops downstream and its amplitude increases significantly as the flow becomes turbulent. The transition to turbulence can be seen from the increase of magnitude of the peaks at both upwash and downwash at x = 700 mm, as a consequence of increased mixing.

Since parts of intense regions of both sinuous and varicose modes are located on either side of the low-speed streak near the stem of the vortex structure, the measured fluctuating velocity in those regions is affected by these two modes. It is very difficult to separate these two modes from the raw experimental data in those regions. However, as discussed earlier, the other parts of the intense region of the sinuous and varicose modes, which are located near the boundary layer edge, occur at different location. The intense turbulence corresponding to varicose mode occurs at the peak of the vortex structure or the low-speed streak to form a dome structure, while the one corresponding to sinuous mode occurs at the side of the low-speed streak near the boundary layer edge. By carefully measuring the maximum turbulence intensity in the intense regions near the boundary layer edge at both the dome structure (varicose mode) and the side of the low-speed streak (sinuous mode) for a number of streamwise locations along the nonlinear region, one can predict the

dominant mode of the secondary instability near the boundary layer edge although the largest turbulent intensities for both sinuous and varicose modes occur near the stem of the vortex structure.

The maximum values of turbulence intensity are extracted from the experimental data for three regions: I, II, and III, as shown in Fig. 4.8. Region I is near the stem of the vortex structure where the maximum shear and turbulence intensity are found. The streamwise velocity fluctuations in this region are affected by the sinuous and varicose modes of secondary instability. Region II covers the area at the edge of low-speed streak where the high-shear region of $\partial u/\partial z$ is observed in iso-$\partial u/\partial z$ shear contours. This region corresponds to the sinuous mode of secondary instability. Lastly, region III is the area with high $\partial u/\partial y$ shear at the peak of the vortex structure or the low-speed streak (dome) which corresponds to the varicose mode of secondary instability.

Figure 4.9 shows the development of the maxima of the intense turbulence in the three defined regions. The snapshot in the figure provides a clearer comparison between the maxima of turbulence intensities ($Tu_{\max}$) in regions II and III which correspond to the development of the sinuous and varicose modes near the boundary layer edge, respectively. The values of $Tu_{\max}$ in region II are always above those in region III along streamwise locations, indicating that the sinuous mode is more dominant than the varicose mode in the nonlinear region. The ratio of $Tu_{\max}$ in region III to that in region II is 0.45-0.62, that is, the fluctuations due to varicose mode is about two times smaller than those due to sinuous mode. It should be noted that these values are calculated from the experimental data in the region near the boundary layer edge. The $Tu_{\max}$ in those regions is still very small compared to the $Tu_{\max}$ in region I, as shown in the figure, in which the line of region I lies far beyond the lines of regions

II and III. It is also found that the spanwise location of Tu_{max} is observed at either side of the stem of the vortex structure, instead of lying at the center of the iso-*u* vortex structure. It reveals that the pair of intense regions of fluctuation is still present further downstream.

Comparisons of the present results with the experimental results of Mitsudharmadi *et al*. (2004) and the numerical results of Girgis and Liu (2006) are presented in Fig. 4.10. The snapshot of the figure captures the streamwise locations where the numerical study of Girgis and Liu (2006) was carried out to give a better comparison. These numerical results considered only the most amplified mode, which is the sinuous mode.

In the linear development stage of Görtler vortices, the present results agree very well with the results of Mitsudharmadi *et al*. (2004). In the nonlinear region, both results also show the same mechanism of the streamwise evolution of the Tu_{max}. The Tu_{max} slightly decreases until a certain streamwise location, where the transition Görtler number $G_{\theta,tr}$ is about to be reached. Mitsudharmadi *et al*. (2004) found the $G_{\theta,tr}$ to be 6.8 at x = 805 mm based on Finnis and Brown's method (Finnis and Brown, 1997). After reaching the minimum value, Tu_{max} increases considerably to a maximum value at the $G_{\theta,tr}$. Subsequently, Tu_{max} slightly decreases in the transition region before drastically increasing due to the onset of turbulence.

Since the experimental measurements are subjected to sinuous and varicose modes, the iso-*Tu* contours (Fig. 4.6) and Tu_{max} (Fig. 4.10) are affected by these modes. This may explain why the numerical results of Girgis and Liu (2006) do not quite agree with the experimental results of Mitsudharmadi *et al*. (2004). However, as seen in the snapshot in Fig. 4.10, the present experimental results agree well with the numerical results of Girgis and Liu (2006) prior to the transition at $G_{\theta,tr}$ = 7.20. As

Girgis and Liu (2006) only considered the sinuous mode of secondary instability, the good agreement between present results and Girgis and Liu's (2006) prior to the transition confirms that the sinuous mode is dominant over the varicose mode in the nonlinear region of Görtler instability. The large discrepancy between present results and Girgis and Liu's (2006) after the transition is because their numerical study did not take into account the effect of transition.

4.5 Vortex Growth Rate

To assess the growth of the vortices in term of the mean streamwise velocity component, a vortex or disturbance amplitude κ_u (Winoto and Crane, 1980; Finnis and Brown, 1989) is defined as

$$\kappa_u = \frac{u_d(\eta) - u_u(\eta)}{2U_\infty} \tag{4.1}$$

where u_d is the mean velocity at downwash, u_u the mean velocity at upwash. The developments of $\kappa_{u,\max}$ along the streamwise direction for the three cases are shown in Figs. 4.11 and 4.12 together with the results of Mitsudharmadi *et al*. (2004) and Finnis and Brown (1997) for comparison. Note that the present results for R = 1.0 m and Mitsudharmadi *et al*.'s (2004) for R = 2.0 m are for pre-set most amplified wavelength Görtler vortices, while Finnis and Brown's (1997) are for naturally developed Görtler vortices for R = 4 m. The slope of the curves in the semi-log presentation in Fig. 4.11 corresponds to the constant value of vortex growth rate β assumed in the normal-mode analysis (Finnis and Brown, 1989).

The development of $\kappa_{u,\max}$ in Fig. 4.11 can be divided into three regions of different disturbance growth rate (Mitsudharmadi *et al*., 2004). The first region is characterized by the steep increase of $\kappa_{u,\max}$ in the linear region of Görtler instability,

where the spanwise-periodic streamwise velocity profiles become wavier downstream along this region. At the end of linear region, at $x \approx 350$ mm for cases 1 and 2 and at $x \approx 400$ m for case 3, the slopes of the curves decrease considerably, that is, only a slight increase of $\kappa_{u,\max}$, in the second region before the negative growth as the mushroom-like structures decay prior to turbulence in the third region. The slight increase and then decrease of $\kappa_{u,\max}$ shows that the finite amplitude of the disturbance has been reached. In this region, the flow is dominated by the mushroom-like structures and transformed into the new possibly steady state in which the secondary instabilities may grow (Schmid and Henningson, 2001). The maximum $\kappa_{u,\max}$ before the decay of the mushroom-like structures is about 0.30 for Mitsudharmadi *et al*. (2004) and all the three cases in the present work, regardless of the concave surface radius of curvature and the free-stream velocity. Winoto and Crane (1980) reported that this value was in the range of 0.3 to 0.4.

The effect of concave surface radius of curvature can be derived by comparing the slope of the curves in Fig. 4.11. As expected, the smaller concave surface radius of curvature results in higher vortex growth rate in the linear region due to the stronger centrifugal effect. The slopes obtained from the figure (which correspond to the vortex growth rate β) are 7.0 m^{-1}, 4.7 m^{-1}, and 3.7 m^{-1} for R = 1 m, 2 m, and 4 m respectively. Consequently, the onset of the nonlinear region is more upstream for the smaller radius of curvature. However, the vortex growth rate seems to be unaffected by free-stream velocity since the slopes of the curves for all cases in the present work with different free-stream velocities do not vary. The same is true for the Finnis and Brown's (1997) results with two different free-stream velocities.

By plotting $\kappa_{u,\max}$ against G_θ, as shown in Fig. 4.12, all data of $\kappa_{u,\max}$ for pre-

set wavelength Görtler vortices fall on a single line. Similarly, all data of $\kappa_{u,\max}$ for naturally developed Görtler vortices of Finnis and Brown (1997) also fall on another single line. Finnis and Brown (1997) mentioned that it was not clear whether this was a coincidence or whether the vortex maximum amplitudes would also lie on the same line. Based on the present results, it can be concluded that all data of $\kappa_{u,\max}$ obtained from the same experimental set-up for the most amplified vortex wavelengths will fall on a single line, regardless of the values of U_∞ and R. The streamwise (x) locations where the tangent of the lines decreases significantly (which corresponds to the onset of the nonlinear region) for pre-set wavelength Görtler vortices occurs at about the same Görtler number $G_\theta \approx 5.0$ and the disturbance amplitude $\kappa_{u,\max} \approx 0.29$.

The κ_u criterion is to quantify the growth of the vortices and to detect the maximum disturbance amplitude and the location of the most amplified disturbances in the boundary layer. However, to quantify the longitudinal amplification of disturbances, an integral criterion as suggested by Toé *et al*. (2002) may be more appropriate since it covers the whole boundary layer, not only at the middle of upwash and downwash. This criterion is defined as an amplification parameter (P_z) based on the spanwise gradient of the streamwise velocity ($\partial u/\partial z$), that is:

$$P_z = \int_{y=0}^{\infty} \int_{z=0}^{2\lambda} \left| \frac{\partial u}{\partial z} \right| dz\, dy \tag{4.2}$$

Figs. 4.13 and 4.14 show the streamwise variation of P_z and its variation with Görtler number G_θ, respectively. The trend of the lines is similar to the maximum disturbance amplitude curves in Figs. 4.11 and 4.12. The development of Görtler vortices is first observed from the steep increase of P_z until x = 400 mm for cases 1 and 2, and until x = 450 mm for case 3. It is noticed that these streamwise locations,

which are presumed to be the location of the onset of nonlinear region, are slightly downstream of those obtained from the $\kappa_{u,\max}$ curves (Fig. 4.11). Downstream of these streamwise locations, the slopes of the curves decrease significantly before the decay of the mushroom-like structures that turns the flow into turbulence. The slope of the lines in Fig. 4.13 corresponds to an exponential change of P_z with x in the form $A^{\beta_o x}$, where β_o is defined as the amplification rate of the perturbations (Toé *et al*., 2002). For all cases in the present work, the exponential change of P_z per meter is found to be 5.6, and it compares well with 5.7 of Toé *et al*. (2002).

From the definition, $\kappa_{u,\max}$ is the maximum difference between the streamwise velocity at downwash and upwash at a particular streamwise (x) location. This difference causes the momentum transfer between the downwash and upwash which is a result of the flow instability. The normal distance from the wall where $\kappa_{u,\max}$ occurs is denoted as $y(\kappa_{u,\max})$, and may indicate the location of the most unstable region of the mean components of Görtler instability at a particular streamwise location. Figures 4.15 and 4.16 show the downstream variation of $y(\kappa_{u,\max})$ for all the three cases. The data were obtained across the boundary layer at the center of upwash and downwash. The measurements were carried out with the step of 0.05 mm for y = 0.05-2.00 mm and 0.50 mm for y > 2.00 mm.

As shown in Fig. 4.15, the $y(\kappa_{u,\max})$ increases downstream until it reaches its peak at x = 350 mm for case 1, at x = 350-400 mm for case 2, and at x = 450 mm for case 3. The peak of $y(\kappa_{u,\max})$ is shifted rightward and upward with decreasing free-stream velocity. These shifts may be explained by lower centrifugal force and thicker boundary layer for lower free-stream velocity. By using G_θ as the abscissa, the peaks of $y(\kappa_{u,\max})$ occur at about the same $G_\theta \approx 5.0$ which corresponds to the onset of the

nonlinear region, as shown in Fig. 4.16. In the nonlinear region, $y(\kappa_{u,\max})$ decreases due to the presence of secondary instability which is initiated near the boundary layer edge. The primary mode of Görtler instability seems to move towards the wall where the viscous effect and hence the damping effect is significant. This results in the secondary instability to become the dominant mode in the nonlinear region.

Figure 4.17 shows $y(\kappa_{u,\max})$ normalized by the Blasius boundary layer thickness (δ_L) at some streamwise locations in terms of the corresponding Görtler number G_θ. In the linear region, the waviness of the streamwise velocity distribution along the spanwise direction is most pronounced at the normal distance slightly below half of Blasius boundary layer thickness, that is, between $0.4\delta_L$ and $0.5\delta_L$. The normalized $y(\kappa_{u,\max})$ significantly decreases towards the surface region until $G_\theta \approx 6$. This seems to indicate that in the range of Görtler number (G_θ) between 5 and 6, the secondary instability sets in and overtakes the primary Görtler instability. It is believed that the energy conversion from primary to secondary instability takes place at this range of Görtler number (Yu and Liu, 1994). The secondary instability is initiated near the boundary layer edge, as discussed previously, and penetrates down the primary instability towards the concave surface, as shown in Fig. 4.17 by the occurrence of $\kappa_{u,\max}$ near the concave surface downstream of $G_\theta \approx 6$. The stronger viscous effect near the concave surface in the nonlinear region may explain why $\kappa_{u,\max}$ does not grow as fast as in the linear region.

4.6 Concluding Remarks

Three different cases have been experimentally investigated for concave surface with R = 1.0 m by using different wire spacing and different free-stream

velocities but the same wavelength parameter $\Lambda \approx 250$ to produce the most amplified wavelength Görtler vortices. The wavy profiles caused by the perturbation wires are amplified downstream to form horseshoe vortices and subsequently mushroom-like structures in the nonlinear region as the result of the onset of secondary instability. The wavelengths of the vortices are preserved downstream for all cases which confirm the prediction of the most amplified wavelength Görtler vortices.

The appearance of a second inflection point in the region between the wall surface and the boundary layer edge to form an **S**-shape velocity profile across the boundary layer at the upwash may be responsible for transition into turbulence. It is also confirmed from the turbulence intensity (Tu) profile in that region, where the highest peak is found between the wall surface and the boundary layer edge which simply corresponds to the location of the second inflection point in the velocity profile. This region is also well correlated with the peaks in the iso-$\partial u/\partial z$ shear contours and with the inflectional spanwise profile of streamwise velocity, and it is suspected to be responsible for the sinuous mode of secondary instability. In contrast to the sinuous mode, the intense regions of fluctuation that is responsible for the varicose mode of secondary instability are more related to the high-shear layers in iso-$\partial u/\partial y$ contours.

Three regions with the intense turbulence were found in the iso-Tu contours: near the stem of the vortex structure, at the edge of low-speed streak, and at the peak of the vortex structure (dome) which seem to correspond to developments of the maximum turbulence intensity (sinuous and varicose modes), sinuous mode, and varicose mode of secondary instability, respectively. The sinuous mode was found to be more dominant than the varicose mode in the nonlinear region.

Comparison of the present results with the previous results of larger radii of curvature shows that smaller radius of curvature results in higher vortex growth rate, as expressed in term of maximum disturbance amplitude $\kappa_{u,\max}$, in the linear region due to stronger centrifugal force. Consequently, the onset of the nonlinear region is found to be more upstream for the case of smaller radius of curvature, and it seems to be unaffected by the free-stream velocity. When $\kappa_{u,\max}$ is plotted against the Görtler number G_θ, all data obtained from the same experimental set-up seem to lie on a single line, regardless of the values of U_∞ and R.

The normal distance from the wall where $\kappa_{u,\max}$ occurs, denoted as $y(\kappa_{u,\max})$, increases in the streamwise direction until the onset of the nonlinear region following the thickening of the boundary layer, and decreases towards the wall due to the presence of secondary instability which is initiated near the boundary layer edge. The primary instability is penetrated downward and damped by the viscous effect near the surface. The secondary instability is overtaking as the dominant mode in the flow in the range of Görtler number G_θ between 5 and 6. Downstream of the streamwise (x) position where $G_\theta \approx 6.0$, the flow is dominated by the sinuous mode secondary instability.

CHAPTER 5

SPECTRAL ANALYSIS ON SECONDARY INSTABILITY

5.1 Introduction

The linear development of Görtler vortices can be considered to have been well established both analytically and experimentally. Thus, a lot of attention has recently been directed to the secondary instability phenomenon in the nonlinear region of Görtler vortices. However, most experimental works on the secondary instability were carried out in the naturally developed Görtler vortices. In addition, very limited information on spectra of secondary instability modes of Görtler vortices can be found in the literature. The dominant secondary instability mode in nonlinear region of Görtler vortices, as well as the transition process leading to turbulence, has not been clearly understood.

Bottaro and Klingmann (1996) showed that as the complexity of the flow field increases further downstream, the number of unstable modes in the eigenvalue spectrum increases, and the spectrum becomes more difficult to interpret. The number of spanwise harmonic mode required to interpret the spanwise variation of streamwise velocity correctly increases further downstream. Peerhossaini and Bahri (1998) performed spectral analysis of the spanwise distribution of streamwise velocity and found that seven modes are sufficient to represent the velocity field in the nonlinear regime.

This chapter focuses on the spectral analysis of the secondary instability modes of the most amplified wavelength Görtler vortices. The nonlinear growth of

Görtler vortices of case 1 (λ_m = 12 mm, U_∞ = 2.8 m/s) is presented in this chapter. The discussion includes the spanwise harmonics of streamwise velocity and frequency characteristics of Görtler vortices. Fast Fourier Transform (FFT) algorithm was developed to obtain the power spectrum.

5.2 Nonlinear Growth of Görtler Vortices

The nonlinear development of Görtler vortices is initiated by a nonlinear reorganization of perturbation energy growth (Bottaro and Klingmann, 1996), in which the typical mushroom-like structures develop in the mean streamwise velocity contours (Fig. 4.1). In this region, the energy begins to depart from its exponential growth to reach an asymptote before finally it saturates at a constant level. The flow subsequently becomes susceptible to secondary instability.

The perturbation energy e, which can also be used as the measure of perturbation growth, is defined as (Bottaro and Klingmann, 1996):

$$e = \frac{1}{2}\int_0^{\lambda/2}\int_0^{\infty}\left(u - U_{Blas}\right)^2 dydz \tag{5.1}$$

where u is the streamwise velocity, U_{Blas} the corresponding velocity based on Blasius laminar boundary layer velocity profile, and $\lambda = \lambda_m$ the spanwise wavelength of the vortices.

The leveling-off of the relative perturbation energy $E = e/e_0$ as the instability reaches nonlinear region is clearly shown in Fig. 5.1, where e_0 represents the initial energy defined at x_0 = 150 mm. The energy initially increases at a quasi-exponential rate in the linear region. It begins to depart from the quasi-exponential growth at x = 350 mm and reaches its saturation level approximately at x = 500 mm. This range of streamwise (x) location corresponds to streamwise location where the formation of

horseshoe vortices takes place and develops further into the mushroom-like structures, as observed in the mean streamwise velocity contours (Fig. 4.1). This observation suggests that the transformation of the horseshoe vortices into the mushroom-like structures is a result of the nonlinearity development of Görtler instability. The secondary instability subsequently appears in the flow as the energy saturation level is reached.

The nonlinear development of vortex growth rate can also be seen in the normal distribution of disturbance amplitude κ_u [Eq. 4.1], as shown in Fig. 5.2. The first peak appears as the wavy profiles observed in the mean streamwise velocity contours. In the linear region, where the perturbation energy increases exponentially, the peak of the κ_u profile becomes more pronounce. At x = 350 mm, where the energy begins to depart from its quasi-exponential growth, the peak (which also corresponds to the maximum disturbance amplitude $\kappa_{u,\max}$) seems to saturate at $\kappa_{u,\max} \approx 0.3$. It is subsequently followed by the appearance of the second peak near the boundary layer edge at x = 400 mm. Further downstream, the first peak moves toward the wall while the second peak is lifted up before finally the flow becomes turbulence.

It is interesting to note that the formation of the second peak occurs at the streamwise (x) location where the perturbation energy begins to depart from a quasi-exponential growth until reaching the saturation level, that is at x = 350-500 mm. Once the perturbation energy reaches its saturation level, the second peak seems to be damped. This can be seen in Fig. 5.2 that the amplitude of the second peak begins to decrease at x = 500 mm and finally disappears as the flow becomes turbulent.

Since the second peak is initiated at the boundary layer edge at x = 400 mm, it is therefore related to the head of the mushroom-like structures in the mean velocity contours. The decreasing magnitude of the second peak is hence a result of the

dispersing of the mushroom-like structures as the increased mixing due to the transition to turbulence. On the other hand, the first peak, which is located near the stem of the vortices, consistently maintain its magnitude until x = 750 mm, even though the second peak has died down. In addition, the wavy profiles still exist and there is no inflection point found in the spanwise distribution of mean streamwise velocity $u(z)$ near the stem region. It may be due to the dominant effect of the viscous terms near the wall.

5.3 Spanwise Harmonics of Streamwise Velocity

The nonlinear development of Görtler vortices leads to a change in the spanwise distributions of streamwise velocity $u(z)$. Figure 5.3 shows the typical spanwise distributions of $u(z)$ in nonlinear region (x = 600 mm) for several normal (y) locations. The inflectional velocity distributions $u(z)$, as the indication of the imminent onset of secondary instability, are observed at $y = 0.50\delta_L$ to $y = 1.00\delta_L$. However, these inflectional velocity distributions are not found at the $y = 0.25\delta_L$ (vortex's stem region) and at $y = 1.50\delta_L$ (the mushroom head region), as shown in Figs. 5.3(a) and (e) respectively. Corresponding to these normal (y) locations, the $u(z)$ are still in the form of uninflected sinusoidal patterns. The velocity distribution at the stem region is narrow and sharp at upwash while at downwash is wide and flat. In contrast, the velocity distribution at the mushroom head region is wide and flat at upwash and narrow and sharp at downwash.

The spanwise distributions of $u(z)$ shown in Fig. 5.3 cover two pairs of vortices. Those vortices should have the same profiles if the vortices grow at the same rate. However, at $y = 1.50\delta_L$ the first vortex (on the left hand side) seems to have a sinusoidal pattern while there is still a kink observed at the upwash region of the

second vortex (on the right hand side). The kink seen in the second vortex disappears at a slightly higher normal (y) distance at $y \approx 1.70\delta_L$. This suggests that the growth of the second vortex seems to be somewhat faster than the first vortex. The difference in size of the vortices is also shown in the mean streamwise velocity contours (Fig. 4.1(i)). It is observed that there is an alternate size of the mushroom-like structures in the spanwise direction. The structures of the larger vortices are later dispersed earlier than the smaller vortices.

To have a closer look at the spanwise distribution of $u(z)$, streamwise developments of the velocity distribution of the second pair of the vortices (on the right hand side of Fig. 5.3) for three normal (y) locations are plotted in Figs. 5.4 – 5.6. The locations correspond to the normal (y) locations of the first peak, the second peak, and between the peaks of the disturbance amplitude κ_u profile (Fig. 5.2), respectively.

There is no inflection point observed in the spanwise distributions u(z) at both peaks of κ_u profile, as shown in Figs. 5.4 and 5.5. The first peak, which corresponds to the maximum disturbance amplitude $\kappa_{u,\max}$, appears as the Görtler instability occurs and is located at the vortex's stem region. Whilst the second peak is initiated near the boundary layer edge and corresponds to the mushroom head region. The velocity distribution at the first peak seems to grow (Fig. 5.4) only in the normal (y) direction until x = 350 mm. Downstream of this location, the velocity distribution does not seem to further develop, indicating that the disturbances grow nonlinearly and saturation level is about to be reached. The second peak, which begins to appear at x = 400 mm, seems to be damped in the normal (y) direction further downstream. The velocity distribution at this location (Fig. 5.5.) becomes wide and flat at upwash and its amplitude becomes smaller further downstream. This signifies the energy conversion mechanism from the primary motion to the secondary instability motion

via rate of strain $\partial u/\partial y$ which occurs mainly near the boundary layer edge (Yu and Liu, 1994).

Comparing the spanwise distributions $u(z)$ at the stem and mushroom head regions in Figs. 5.4 and 5.5 respectively, it is noticed that the velocity distribution at upwash transform from narrow and sharp near the wall surface into wide and flat near the boundary layer edge. The velocity distribution at the normal (y) distance between the first and the second peaks is shown in Fig. 5.6. The inflection points are clearly seen in the figure starting from x = 450 mm. However, the inflection points disappear further downstream as the transition to turbulence takes place. The amplitude of the inflected sinusoidal pattern becomes smaller, as well as the amplitude of the spanwise distribution u(z) at the second peak of κ_u profile. This finding suggests that the secondary instability mode that first appears near the boundary layer edge is more dominant in the flow and later leads the flow into turbulence.

The inflected sinusoidal pattern of u(z) distribution suggests that the disturbance quantities are periodic in the z-direction with streamwise independent wavelength. Spectral analysis was subsequently carried out for the spanwise distribution of $u(z)$. The periodic $u(z)$ at any particular streamwise and normal locations (x_0, y_0) can be described in terms of Fourier series expansion as:

$$u(x_0, y_0, z) = \tilde{u}_0 + \sum_{n=1}^{\infty} \left(a_n(x_0, y_0)\cos(n\alpha z) + b_n(x_0, y_0)\sin(n\alpha z) \right) \qquad (5.2)$$

where $\tilde{u}_0$ is the spanwise-average of $u(x_0, y_0, z)$, $\alpha = 2\pi/\lambda_m$ is the dimensional wavelength parameter, a_n and b_n are the Fourier coefficients which correspond to the amplitude of the disturbances modes, and n = 1, 2, 3, … is the spanwise harmonic modes. The spanwise distribution of $u(z)$ is an even function ($u_n = u_{-n}$), and thus only has cosine terms in its Fourier series. The spanwise harmonic modes therefore can be

obtained by calculating the corresponding Fourier coefficients at any particular streamwise and normal locations (x_0, y_0) from:

$$\tilde{u}_0 = \frac{1}{\lambda_m}\int_{-\lambda_m/2}^{\lambda_m/2} u(x_0, y_0, z)dz \tag{5.3a}$$

$$a_n = \frac{2}{\lambda_m}\int_{-\lambda_m/2}^{\lambda_m/2} u(x_0, y_0, z)\cos(n\alpha z)dz \tag{5.3b}$$

$$b_n = 0 \tag{5.3c}$$

The development of the normal distributions of spanwise-average velocity profile u/U_∞, which can also be interpreted as mode 0 in Fourier series ($\tilde{u}_0/U_\infty$), is shown in Fig. 5.7. The local velocity profiles at upwash and downwash are also included in the figure for comparison. Similar to the spanwise distribution of *u*, the normal distribution of *u* is also inflected. The inflection point is observed at upwash region, as well as the spanwise-average velocity profile, at *x* = 350 mm. Further downstream, the inflection points at upwash and spanwise-average velocity profiles move upward and the second inflection point subsequently appear near the wall to form an **S**-shape velocity profiles. On the other hand, no inflection point is observed at downwash until the mixing process due to transition to turbulence takes place at *x* = 750 mm.

Comparing the streamwise (*x*) locations where the inflection points were first found in the spanwise and normal velocity distributions in Figs. 5.6 and 5.7 respectively, it is noticed that the normal velocity distribution is inflected earlier than the spanwise velocity distribution. The inflected velocity profile in the normal direction is found at *x* = 350 mm, while in the spanwise direction is at *x* = 450 mm. The unstable inflectional spanwise velocity profile is correlated to the sinuous mode of secondary instability (Swearingen and Blackwelder, 1987), while the inflectional

normal velocity profile is more related to the varicose mode. Therefore, this finding implies that the varicose mode appears first in the flow. It is subsequently followed by sinuous mode which will become a dominant mode further downstream and lead the flow into turbulence.

The normal distributions of the amplitude of spanwise harmonic modes are presented in Fig. 5.8. The number of spanwise harmonics to be included in this analysis is limited by the spatial resolution of the hot-wire measurement in the spanwise direction. The streamwise velocity measurement was carried out with the traversing step size of 1.0 mm, and there are 12 data points measured for each pair of the vortex with the wavelength λ_m = 12 mm. The maximum number of harmonic modes obtained from the Fourier series that can be used to have a convergence results is therefore N = 6. Bottaro and Klingmann (1996) found that the reasonable convergence is obtained with $N \geq 3$. In the following analysis, N = 5 will be used throughout.

The characteristics of the spanwise harmonic modes presented in Fig. 5.8 agree very well with the numerical results of Bottaro and Klingmann (1996). The amplitude of the first spanwise harmonic mode ($n = 1$), which can be interpreted as the maximum disturbance amplitude $\kappa_{u,\max}$ in Fig. 5.2, splits into two peaks at x = 400 mm, as shown in Fig. 5.8(b). The first peak moves toward the wall, while the second peak is lifted up from the boundary layer edge as the mushroom head moves upward. The second peak is therefore associated with the velocity deficit at the head of mushroom-like structures.

A similar development, but in the opposite phase, can be seen for the second mode. As the first and second modes split into two peaks, higher modes seem to appear and contribute to the inflected spanwise velocity distribution. Up to x = 400

mm, $N = 2$ should be sufficient to represent the flow field. At $x = 450$ mm, the third mode appears in the form of **S**-shape. Two peaks with positive and negative amplitudes corresponding to this mode are found at the vortex stem and mushroom head regions, respectively. In addition, the fourth mode is also observed at this streamwise (x) location, although its amplitude is much smaller than the lower modes. At $x = 600$ mm, those modes die down leaving the first and second modes present in the flow field. All the harmonics will finally disappear as the flow becomes fully turbulent.

To provide a clearer view about the contribution of each spanwise harmonic mode to the spanwise distribution of $u(z)$, Fast Fourier Transform (FFT) algorithm was used to obtain the power spectra of the velocity distribution. The results showing the development of the power spectra of spanwise harmonic modes for several normal (y) locations are shown in Fig. 5.9. The y-axis in the figure is the absolute value of the amplitude of the harmonic modes, instead of the square of the amplitude (power).

The first spanwise harmonic mode, which increases exponentially in the linear region of Görtler vortices, seems to saturate as the instability reaches the nonlinear region. The discussion on the maximum disturbance amplitude $\kappa_{u,\max}$ reveals that this mode moves towards the wall in the nonlinear region. This may be the reason that the amplitude of the first harmonic at $y = 0.25\delta_L$ does not descend abruptly prior to transition to turbulence, as shown in Fig. 5.9(a). Figure 5.9 also show that the second harmonic is stronger at $y = 0.25\delta_L$ than at the other normal (y) locations. The contributions of the third and fourth harmonics become visible at $x = 450$ mm for all normal (y) locations, and they are relatively stronger at $y = 0.25\delta_L$ and $y = 0.50\delta_L$. The third harmonic still exists near the wall ($y = 0.25\delta_L$) at $x = 750$ mm, and it seems to be stronger than the second harmonic. However, a closer look to the normal distributions

of these modes reveals that the contribution of the second mode is still more significant than that of the third mode, both near the wall and near the boundary layer edge.

5.4 Frequency Characteristics of Görtler Vortices

Spectral analysis was performed to obtain the characteristic frequencies of the secondary instability of Görtler vortices. Since the vortex structures, as shown in streamwise velocity contours (Fig. 4.1), seems to develop in alternating size along the spanwise (z) direction in the nonlinear region, the spectral analysis is therefore carried out for two pairs of vortex structures with different sizes. The corresponding spanwise (z) locations of those vortices in Fig. 4.1 are $z \approx 0$ mm and $z \approx 12$ mm for the first (smaller) and second (larger) vortices, respectively. The raw data were high-pass filtered at 60 Hz to remove electrical noise and low-frequency fluctuations. To reduce the uncorrelated statistical fluctuations, the Welch's method was used in estimating the power spectral density from the raw data.

Figure 5.10 shows the most dominant frequency of secondary instability modes at several streamwise locations for the first vortex. The spectra were obtained from the point of the maximum power within the vortex structure. This location corresponds to the location of the intense turbulence of coherent structure near the wall in Fig. 4.6. Three peaks corresponding to the secondary instability modes are observed in the spectral distributions at the frequencies of 140, 180, and 280 Hz. The frequency of 140 Hz is observed initially at x = 650 mm followed by the other peaks of f = 180 and 280 Hz at x = 700 mm. The streamwise wavelengths of these modes are respectively 16.1, 12.6, and 8.1 mm for the frequencies of 140, 180, and 280 Hz.

Further downstream, the frequency of 180 Hz is found to be the most unstable mode, while the other two frequencies seem to be damped out.

Different spectral distributions are observed for the second vortex, as shown in Fig. 5.11. The frequency of 140 Hz seems to be very dominant in all streamwise (x) locations since its first appearing at x = 650 mm. The other frequencies observed in the first vortex (180 Hz and 280 Hz), are believed to exist. However, these peaks are masked by the dominance of f = 140 Hz. Compared to other frequencies, including the ones observed in the first vortex, the instability mode corresponding to frequency of 140 Hz has the largest power spectral density. Therefore, this secondary instability mode can be considered as the most unstable mode in the flow. This frequency is higher than the theoretical value of 110 Hz of Hall and Horseman (1991) and the experimental value of 130 Hz measured by Swearingen and Blackwelder (1987). These frequencies correspond to the sinuous mode of secondary instability. However, further analysis need to be carried out to ascertain the type of instability mode of the frequencies obtained in the present experiments.

It is interesting to note from Figs. 5.10 and 5.11 that the dominant frequency is different between two adjacent vortices at the same streamwise (x) location, and both frequencies are preserved further downstream leading the flow into turbulence. This finding suggests that it is possible to have two different secondary instability modes to dominate the flow at the same time, but at different vortex structures.

In addition to the streamwise development of the most unstable secondary instability mode, the following discussions are focused on the spectral distributions of the mode for several spanwise (z) and normal (y) locations. The most unstable mode in the present case is the one corresponds to the frequency of 140 Hz, which is found in the second (larger) vortex structure. The streamwise location x = 750 mm was

chosen to describe the spatial distributions of the most unstable secondary instability mode.

Figure 5.12 shows the power spectral density of secondary instability modes at several spanwise (z) locations. Those spectra were obtained at the same normal (y) location, which corresponds to the location of the most unstable mode at y/δ_L = 0.30 for the streamwise location x = 750 mm. The z = 0 mm corresponds to the middle of upwash region, which is also the line of symmetry in z about the upwash region (vortex structure). It can be seen clearly from the figures that the most unstable mode of f = 140 Hz occurs at the sides of the vortices at z = -1 mm and z = 1 mm, instead of the middle of upwash region (z = 0 mm). The second harmonic of the most unstable mode with f = 280 Hz is prominent at z = 0 mm, and it becomes more important at y = $0.40\delta_L$, as shown in Fig. 5.13(b). This indicates that there is a pair of the most unstable modes in each vortex, and likewise the intense turbulent region in Fig. 4.6, these modes are symmetric about z = 0 mm.

The power spectral density of secondary instability at various normal (y) locations at the middle of upwash region for x = 750 mm are shown in Fig. 5.13. The power spectral density at the middle of upwash region is relatively small compared to that at the side of the vortex structure. In contrast to the first harmonic of the most unstable frequency (f = 140 Hz), the power spectral density of the second harmonic (f = 280 Hz) is larger at the middle of upwash region than at the side of vortex structure. At y = $0.20\delta_L$, the first harmonic of the most unstable mode dominates the flow. However, the second harmonic becomes important near the half boundary layer thickness, as shown in Fig. 5.13(b) and (c) for y = $0.40\delta_L$ and y = $0.60\delta_L$, respectively. Near the boundary layer edge (y = $0.80\delta_L$), all instability modes seem to be insignificant compared to those near the wall and half boundary layer thickness

regions. Similarly, the second harmonic for the first (smaller) vortex structure (f = 360 Hz) also has a larger power spectral density at the middle of upwash region than at the side of the vortex structure, even though the power is relative small compared to that of $f \approx 280$ Hz which is also present in the spectral distribution.

5.5 Concluding Remarks

The spectral analysis has been performed for the streamwise velocity data obtained from hot-wire anemometer measurements in the nonlinear region of Görtler vortices of case 1 (λ_m = 12 mm and U_∞ = 2.8 m/s). Fast Fourier Transform (FFT) has been used to investigate the spanwise harmonics of streamwise velocity and frequency characteristics of Görtler vortices at several streamwise (x) locations.

The nonlinear region of Görtler vortices is initiated by the departure of the perturbation energy from its quasi-exponential growth to reach a saturation level. The secondary instability subsequently appears in the flow. The streamwise (x) locations where the perturbation energy begins to depart from a quasi-exponential growth until reaching the saturation level corresponds to the formation of the second peak near the boundary layer edge in the normal distribution of disturbance amplitude κ_u. Once the perturbation energy reaches its saturation level, the second peak seems to be damped.

The spanwise distribution of streamwise velocity $u(z)$ at the vortex stem region is narrow and sharp at upwash and wide and flat at downwash. In contrast, the velocity distribution at mushroom head region becomes wide and flat at upwash further downstream. However, no inflection points are observed at both sinusoidal patterns of the velocity distributions. The inflection points are found only between the stem and mushroom head regions.

The periodic $u(z)$ at any particular streamwise and normal locations (x_0, y_0) can be described in terms of Fourier series expansion. In the linear region, it is found that the first two modes (N = 2) have been sufficient to represent the flow field. Higher modes will become significant only in the nonlinear region before finally all modes disappear as the flow becomes fully turbulent.

The spanwise distribution of $u(z)$, as well as the mean streamwise velocity contours, show an alternating size of the mushroom-like structures along the spanwise (z) direction in the nonlinear region. Two different dominant frequencies are observed in two different vortex structures. The frequency of 180 Hz is dominant in the smaller vortices, while the dominant frequency in the larger vortices is 140 Hz. The frequency 140 Hz has the largest power spectral density, so this frequency can be considered as the most unstable mode in the flow.

In contrast to the first harmonic of the most unstable frequency (f = 140 Hz), the power spectral density of the second harmonic (f = 280 Hz) is larger at the middle of upwash region than at the side of vortex structure, especially at normal (y) locations near the half boundary layer thickness.

CHAPTER 6

SPANWISE VELOCITY COMPONENT IN NONLINEAR REGION OF GÖRTLER VORTICES

6.1 Introduction

After initial onset of Görtler instability, hot-wire measurements show that a finite-amplitude state, which evolves in the flow direction, is generated as the boundary layer grows. The flow becomes susceptible to secondary instability in the nonlinear region. This instability leads to the appearance of horseshoe vortices and mushroom-like structures. In some cases, the vortices become time-dependent and they meander as they develop further downstream (Hall, 1985). The meandering process may signify the importance of the spanwise velocity component in the Görtler vortex flow in the nonlinear region.

Most studies of Görtler vortices were concerned with the streamwise velocity component. The contribution of spanwise velocity component in the development of Görtler instability seems to have received very little or no attention. Based on their numerical study, Yu and Liu (1994) explained the features of secondary instabilities via energy balancing mechanisms, in which the Reynolds stress-conversion mechanism, thus the spanwise velocity component, was also included in the discussion. However, no experimental result can be found in the literatures to confirm their numerical results. The measurement of spanwise velocity component is necessary in order to study the Reynolds stress, as well as other flow properties, in Görtler vortex boundary layer flow.

Although the spanwise velocity component w is relatively very small compared with the streamwise velocity component u, it is believed to take part in the

appearance of secondary instability in the nonlinear region of Görtler vortices. Therefore, velocity measurements were carried out to obtain spanwise velocity data, especially the fluctuating component w'.

The discussion in this chapter focuses on the flow characteristics related to the spanwise velocity component in the nonlinear region of Görtler vortices. Streamwise and spanwise velocity components in the boundary layer on a concave surface of 1.0 m radius of curvature for case 1 (λ_m = 12 mm and U_∞ = 2.8 m/s) were measured by an *X*-wire probe. The discussion in this chapter is limited only for the flow properties related to the spanwise velocity component, as the streamwise velocity component has been discussed in the earlier chapters.

6.2 Mean Statistics

Figure 6.1 shows the mean spanwise velocity (*w*) contours for several streamwise (*x*) locations in the *y*-*z* plane. The velocity is presented in the normalized spanwise velocity w/U_∞ for three pairs of vortex structures. The velocity contours are dominated by the regions of negative *w*, which are found near the wall and the head of the vortex structures. This may be because the center line of the wind tunnel is not exactly parallel with the center line of the concave surface test section. Therefore, the vortex structures, as shown in the streamwise velocity u/U_∞ contour in Fig. 6.2(i), are slightly skewed to the left. In addition to the regions of negative *w*, a region of positive *w* is found on the left of the vortex stem. It is believed that there is another region of negative *w* on the right of the vortex stem. However, since the vortex structures are skewed to the left, the region of negative *w* is therefore affected by the region of positive *w* from its vicinity. Consequently, the region of negative *w* is covered up by the region of positive *w*, and the secondary flow is formed in the head

of mushroom-like structures. As the vortices develop further downstream, the regions of negative w at the vortex's heads are lifted up while the regions of positive w near the wall are pushed downward, as shown in Fig. 6.1(a) and (b). At x = 850 mm, both regions of positive and negative w disappear and the w/U_∞ contours become unorganized as the flow becomes turbulent.

To confirm that there is a secondary flow in the vortex's head at the upwash region, the mean spanwise velocities w/U_∞ across boundary layer are plotted for several spanwise (z) locations. Figure 6.2 shows the spanwise velocity profiles at four spanwise (z) locations for x = 650 mm. The spanwise (z) locations, which are shown in the streamwise velocity u/U_∞ contour in Fig. 6.2, include: (a) at the middle of downwash region, (b) at the side of downwash region, (c) at the side of upwash region, and (d) at the middle of upwash region.

In concave surface boundary layer flow, the appearance of counter-rotating vortices are indicated by the positive w near the wall and negative w just above it for the region on the left of the vortex structure, to form an **S** shape spanwise velocity profiles. Such velocity profiles can be seen clearly in Figs. 6.2(b) and (c), which show the spanwise velocity profile at downwash and upwash regions, respectively. These shapes agree very well with the analytical results of Smith (1955) and the experimental results of Bippes (1978), especially at the downwash region.

Since the streamwise counter-rotating vortices are symmetric in z-direction about the middle of upwash and downwash regions, the spanwise velocity across boundary layer should be zero at these spanwise (z) locations. However, the spanwise velocity at the middle of upwash that corresponds to the region of vortex's head is to form a negative peak region, as shown in Fig. 6.2(d). This may be explained by the asymmetry of the vortices, which is slightly skewed to the left. The skewness of the

vortices is amplified by the secondary instability to produce a secondary motion in the vortex's head region. At the vortex' stems and the middle of downwash regions, the spanwise velocity profiles are not too affected by the asymmetry of the flow. These suggest that the region of vortex's head is the most prone to the flow disturbances. The secondary instability, which is initiated at the boundary layer edge, amplifies the asymmetry of the free-stream flow. This also confirms the significance of the free-stream disturbances in generating the vortex modes (Bassom and Hall, 1994).

Since the raw spanwise velocity data can be fitted with a spline and calculated for a fine mesh grid by interpolation, its derivatives can also be calculated in y-z plane and thus the iso-shear contours. Figures 6.3 and 6.4 show the $\partial w/\partial y$ and $\partial w/\partial z$ iso-shear contours for some streamwise (x) locations in the nonlinear region.

The alternate positive and negative $\partial w/\partial y$ shear regions are found at the upwash region across the boundary layer, as shown in Fig. 6.3. The positive $\partial w/\partial y$ shear is dominant near the wall and the vortex's head, while the negative $\partial w/\partial y$ is dominant between those regions at the vortex's body. Further downstream, the positive shear region at the vortex's body is damped by the negative shears on its top and bottom. The negative shear regions are subsequently merged and lifted up to occupy the vortex's head just below the positive shear region. As the vortex' structures disperse due to turbulence, the shear regions also vanish.

Unlike the symmetrical contours in z about the upwash region of the $\partial w/\partial y$ iso-shear contours, the $\partial w/\partial z$ iso-shear contours are anti-symmetry in z about the line between upwash and downwash regions, as shown in Fig. 6.4. Two pairs of anti-symmetric structures are found in the $\partial w/\partial z$ iso-shear contours. Near the wall, positive and negative shear regions are found at downwash and upwash regions,

respectively. In contrast, at the vortex's head, a positive shear is found at upwash and a negative shear is found at downwash. Although the values of $\partial w/\partial z$ and $\partial w/\partial y$ shears are comparable, they are at least an order smaller than the streamwise shear stresses ($\partial u/\partial y$ and $\partial u/\partial z$).

6.3 Fluctuating Components

It is evident from the flow visualizations that the low-speed streaks developed by the vortex field will experience periodic oscillations prior to transition (Swearingen and Blackwelder, 1987). The primary aim of the spanwise velocity measurement is to investigate the frequency characteristics of the spanwise velocity fluctuating component in the nonlinear region of Görtler vortices. It is believed that the frequencies of the spanwise oscillations are relatively lower than those of the streamwise velocity fluctuating component. The sampling rate in the hot-wire measurement was therefore reduced to 600 Hz to capture smaller frequency of the spanwise fluctuations up to 300 Hz. Spectral analysis was performed to obtain the characteristic frequencies of the spanwise oscillations. The raw data were high-pass filtered at 10 Hz to remove the very low-frequency fluctuations. The Welch's method was subsequently used to estimate the power spectral density from the raw data and at the same time to reduce the uncorrelated statistical fluctuations.

Figure 6.5 shows the power spectral density of the spanwise velocity component w for several streamwise (x) locations. Two dominant peaks corresponding to frequencies of 70 Hz and 90 Hz are observed at x = 650 mm, as shown in Fig. 6.5(a). Although it is not clear, the frequency of 140 Hz also appears at this streamwise location. The frequency of 140 Hz becomes dominant at x = 700 mm, and it is subsequently followed by the appearance of another unstable frequency of

180 Hz at x = 750 mm. The last two frequencies are believed to correspond to the streamwise velocity fluctuating component, as discussed in the previous chapter. Further downstream, all peaks in the spectral distribution die down and the power spectral density is distributed uniformly along the frequency band between 20 Hz to 100 Hz, indicating the turbulence flow field, as shown in Fig. 6.5(e).

The contours of Reynolds normal stress $\overline{w'^2}$ on the y-z plane are shown in Fig. 6.6. Two intense regions are found at the stem and head of the vortex structures. This suggests that the mushroom-like structures oscillate in the spanwise direction, intensely at the head and stem of the vortices. As the vortices grow in the normal (y) direction further downstream, the intense region at the vortex's head also moves upward, while the intense region at the stem moves towards the surface. At the vortex's stem, the contours resemble closely to the normalized r.m.s spanwise velocity field of the most amplified sinuous mode computed by the linear viscous secondary instability analysis (Yu and Liu, 1994). However, the contours at the vortex's head resemble more closely to the varicose mode although the intense region is only found on the left, instead of both shoulders of the vortices, due to the skewness of the vortex's structures.

The rate of total integrated kinetic energy of secondary perturbations, which is derived from the continuity and momentum equation, comprises the energy-conversion mechanism from the primary instability and the rate of viscous dissipation (Yu and Liu, 1994). The energy-conversion mechanism from the primary to the secondary instability is accomplished through the work of the shear stresses $-\overline{u'v'}$ and $-\overline{u'w'}$ against the rates of strain of the primary motion, $\partial u/\partial y$ and $\partial u/\partial z$. The present velocity measurements by means of X-wire provide the spanwise and streamwise velocity components, u and w. Therefore, the Reynolds stress $-\overline{u'w'}$, as well as the

corresponding energy conversion from the primary to the secondary motion $-\overline{u'w'}\,\partial u/\partial z$, can be calculated from the experimental data.

The contours of Reynolds shear stress $-\overline{u'w'}$ for several streamwise (x) locations are shown in Fig. 6.7. The Reynolds stress $-\overline{u'w'}$ is anti-symmetric in z-direction, and it agrees with the computational result of Yu and Liu (1994). The structures resemble the $\partial u/\partial z$ iso-shear contours (Fig. 4.5). Two intense regions of positive and negative shears are found at both the stem and head of the vortices. The intense values are more concentrated at the vortex's stem than at the vortex's head. Therefore, the energy conversion mechanism $-\overline{u'w'}\,\partial u/\partial z$ occurs at the stem and head of the vortices, in which the most intense values are on the sides of the vortex's stem. The locations of the most intense of $-\overline{u'w'}\,\partial u/\partial z$ and its values (Yu and Liu, 1994) correlate well with the r.m.s values of u'. This may explain the less intense turbulence, relative to the stem region, at the head of mushroom-like structures (Fig. 4.9).

The comparison of Reynolds shear stress $-\overline{u'w'}$ between the present experimental results and the computational results of Yu and Liu (1994) is shown in Fig. 6.8. The computational shear stress contours are given for both sinuous and varicose modes, as shown in Fig. 6.8(b) and (c). The contours were evaluated at the streamwise (x) location where secondary instability fluctuations are observed to grow rapidly compared to the saturated primary Görtler instability. In the present experiment, the secondary instability grows rapidly at Görtler number G_θ = 7.7 – 9.5 (Fig. 4.9), which corresponds to the streamwise location of x = 600 – 800 mm. The Reynolds shear stress $-\overline{u'w'}$ at x = 700 mm in the present experiments is therefore chosen for comparison, as shown in Fig. 6.8(a).

It is clearly seen in Fig. 6.8 that both sinuous and varicose modes appear in the present experiment. Similar to $\overline{w'^2}$, the Reynolds shear stress $-\overline{u'w'}$ contour also shows the resemblance with the sinuous mode at the stem region and with the varicose mode at the shoulders of mushroom structures. Since the intense values are more concentrated at the stem region, the Görtler instability in the present case (λ_m = 12 mm and U_∞ = 2.8 m/s) is therefore confirmed to be dominated by the sinuous mode. This also agrees with the analysis of the streamwise velocity component *u*, as discussed in Chapter 4.

6.4 Concluding Remarks

The characteristics of Görtler vortex boundary layer flow related to the spanwise velocity component has been investigated by *X*-wire measurements of the streamwise and spanwise velocity components, *u* and *w*, along a concave surface of *R* = 1.0 m for the nonlinear region of case 1 (λ_m = 12 mm and U_∞ = 2.8 m/s). The vortex structures obtained are slightly skewed to the left, so the contours are dominated by the regions of negative *w*. The appearance of streamwise counter-rotating vortices is also shown by the spanwise velocity profiles across the boundary layer. The secondary motion appears in the vortex head region as an amplification of the free-stream disturbances by the secondary instability.

The $\partial w/\partial y$ iso-shear contours are symmetrical in *z* about the upwash, while the $\partial w/\partial z$ iso-shear contours are anti-symmetrical in *z* about the line between upwash and downwash regions. In addition to the high-shear region near the wall, an alternate positive and negative $\partial w/\partial y$ shears are found at the upwash region across the boundary layer. Unlike the $\partial w/\partial y$ shear, two pairs of anti-symmetry structures are

found in the $\partial w/\partial z$ iso-shear contours. At upwash region, positive and negative shear regions are found at the vortex head and near the wall, respectively. In contrast, positive and negative shear regions are respectively found near the wall and vortex's head at the downwash region.

Two dominant peaks corresponding to frequencies of 70 Hz and 90 Hz are initially observed in the spectral distribution of spanwise velocity *w*. The frequencies of 140 Hz and 180 Hz consecutively appear further downstream and they dominate the flow. The last two frequencies are believed to correspond to the streamwise velocity fluctuating component. When the flow becomes turbulent, the all peaks in the spectral distribution die down and the power spectral density is distributed uniformly along the frequency band between 20 Hz to 100 Hz. The most unstable frequency observed in the power spectral density is found exactly at the maxima of the $\overline{w'^2}$ -contours. Two intense regions of $\overline{w'^2}$ are found at the stem and head of the vortex structures, with the most intense region is at the vortex's stem. This implies that the mushroom-like structures oscillate in the spanwise direction, intensely at the stem and head of the vortices.

The Reynolds shear stress $-\overline{u'w'}$ contour is anti-symmetric in *z*-direction, which resembles the $\partial u/\partial z$ iso-shear contours. The contour comprises two intense regions of positive and negative shears at both the stem and head of the vortices. The energy conversion mechanism $-\overline{u'w'}\,\partial u/\partial z$ also occurs at the stem and head of the vortices, in which the most intense values are on the sides of the vortex's stem. Comparison with $-\overline{u'w'}$ contour obtained from computation shows that the contours obtained from experiment are more dominated by the sinuous mode of secondary

instability than that of varicose mode. This confirms the dominance of the sinuous mode in the present experiment.

CHAPTER 7

WALL SHEAR STRESS IN GÖRTLER VORTEX FLOW*

7.1 Introduction

Unlike wall shear stress measurement in flat plate boundary layer, there is dearth of reported wall shear stress results (either experimental or numerical) in concave surface boundary layer flows. Experimental data on wall shear stress along concave surface boundary layer are scarce, which can be due to the difficulties associated with direct measurement of wall shear stress on concave surface.

The available data (Swearingen and Blackwelder, 1987; Ajakh *et al*., 1996) were obtained from curve-fitting wherein only few points near the wall were considered so that the wall shear stress may not be accurately estimated. In addition, analytical and numerical studies cannot provide reliable solutions to understand the physics of Görtler instability problem without accurate experimental data. Therefore, the present study is focused on providing more extensive experimental wall shear stress data in the presence of Görtler instability. These experimental data will be useful for comparison with future analytical or numerical study of Görtler instability.

The wall shear stress will be obtained from the near-wall hot-wire measurements using the near-wall velocity gradient technique (Hutchins and Choi, 2002). The streamwise velocity was obtained for the first 2.00 mm of the normal (y) distance from the wall with the step size of 50 μm. Three pairs of vortices were captured in the measurement with 2.0 mm traversing step along the spanwise (z) direction. Three cases of different wavelengths and free-stream velocities were

* Parts of this Chapter have been published in *Physics of Fluids* (Tandiono *et al*., 2009b).

considered in the measurements: (1) λ_m = 12 mm, U_∞ = 2.8 m/s, (2) λ_m = 15 mm, U_∞ = 2.1 m/s, and (3) λ_m = 20 mm, U_∞ = 1.3 m/s.

7.2 Near-Wall Velocity Gradient Technique

Measuring wall shear stress in the boundary layer using the mean velocity gradient at the wall is essentially a matter of accurately obtaining the velocity profile near the wall. The gradient of the line fitted to the linear portion of the velocity profile is assumed to be the same as the gradient at the wall, and it is then used to calculate the wall shear stress τ_w from the following expression:

$$\tau_w = \mu \left(\frac{du}{dy} \right)_{y=0} \tag{7.1}$$

where μ is the fluid dynamic viscosity, u the streamwise velocity, and y the normal distance from the wall. It is well established that the viscous sublayer, which extends to a value of $y^+ \approx 5$, exists in all turbulent flows and the velocity gradient in this region is linear (Azad and Burhanuddin, 1983). Hence, Eq. (7.1) can be used to estimate the wall shear stress in concave surface laminar and turbulent boundary layer flows.

To accurately measure the velocity near the wall, some difficulties may arise, for example, when the hot-wire probe is traversed into near-wall proximity, the undesired conductive heat transfer from the hot-wire to the wall and the aerodynamic interference to the flow due to the presence of the probe may give rise to the spurious increase in velocity. The wall effect on the spurious velocity measurements extends to a certain distance from the wall depending on the thermal conductivity of the wall material and the dimension of the hot-wire probe. For a low thermal conductivity material, for example plexiglass, the wall effect extends to $y^+ \approx$ 2.0-3.5 (Polyakov

and Shindin, 1978; Ligrani and Bradshaw, 1987b; Park and Wallace, 1993; Hutchins and Choi, 2002) in turbulent boundary layer, and higher for the material with a larger thermal conductivity. On the other hand, the velocity profile in a turbulent boundary layer is believed to be linear only up to $y^+ \approx 5$. Therefore, the remaining "linear" layer that is useful for estimating the wall shear stress from the velocity gradient becomes very thin.

Previous experimental results (Swearingen and Blackwelder, 1987; Ajakh *et al*., 1996) show that the velocity profiles across boundary layer in the presence of Görtler vortices at both upwash and downwash do not follow either the laminar (Blasius) or turbulent (one-seventh power law) profiles. This fact gives rise to a difficulty in determining the useful linear region to estimate the velocity gradient at the wall. Fortunately, the region with the linear velocity profile in the concave surface boundary layer prior to turbulence, as shown in Fig. 7.1, is sufficiently thick to estimate the wall shear stress by near-wall velocity gradient technique. The least-squares linear fit was then used to estimate the velocity gradient of the "useful" linear region.

Figure 7.1 shows typical velocity data within 2.0 mm from the wall at upwash and downwash for x = 200 mm of case 2 (λ_m = 15 mm and U_∞ = 2.1 m/s). At this particular streamwise (x) location, the useful linear region can be seen to exist for 0.65 mm $\leq y \leq$ 2.00 mm and 0.50 mm $\leq y \leq$ 1.50 mm for upwash and downwash respectively, which correspond to $3 \leq y^+ \leq 8$ in wall units for both upwash and downwash. These limits were determined based on the highest value of the Pearson product-moment correlation coefficient (r) with at least 10 data points involved in the least-square linear fitting. The minimum value of r for these experimental data is 0.99.

Unlike some other wall shear stress measurement methods, for example, sublayer fence, wall hot-wire, and wall pulsed wire, which require the information of the normal (y) position of the sensing element in the viscous sublayer to obtain an accurate reading, the near-wall velocity gradient technique only needs the velocity gradient in the linear region to calculate the wall shear stress. The error due to the probe wall positioning is therefore insignificant in this method, and the main contribution to the error will be due to the gradient fit.

An error analysis was conducted on the least-square linear fit as applied to the near-wall velocity gradient technique to obtain the standard skin friction coefficient error. The standard error in velocity gradient was estimated following Box *et al*. (1978). The present experimental results give a maximum standard gradient error of 3.3 %.

To estimate the positional accuracy of the hot-wire probe in this measurement, the probe positioning was carried out by means of a camera equipped with zoom facility to ensure that the hot-wire probe starts from very near to the concave surface. Then one can rely on the fine-scale traverse mechanism for the subsequent velocity measurement across boundary layer. The positional accuracy of the hot-wire probe was approximated by the intercept of the line fitted from the linear region of the velocity profile with the x-axis (normal distance). It is found to be within ±28 μm at x = 200 mm for case 2, which is similar to the errors of ±25 μm reported (Orlando *et al*., 1974; Brunn, 1995) using positioning method by mechanical probe stop.

7.3 Boundary Layer Development

The presence of Görtler vortices in concave surface boundary layer will give rise to thicker boundary layer at the upwash and thinner boundary layer at the

downwash. In the case of naturally developed Görtler vortices, the boundary layer displacement thickness initially follows the Blasius (flat plate laminar boundary layer) growth until a certain distance from the leading edge where the spanwise wavy profile becomes prominent (Swearingen and Blackwelder, 1987). Figure 7.2 shows the streamwise development of the boundary layer displacement thickness δ^* for the pre-set wavelength Görtler vortices at upwash and downwash, as well as that obtained from the spanwise-averaged velocity profile at each streamwise (x) location for case 2. The Blasius boundary layer displacement thickness is also included in the figure for comparison.

The initial departure of δ^* at upwash from the Blasius curve, as shown in Fig. 7.2, is due to the perturbation wires placed prior to the leading edge at the upwash. Apart from this, the development of δ^* in the present study is similar to that of the naturally developed Görtler vortices (Swearingen and Blackwelder, 1987). At the upwash, δ^* increases considerably from x = 250 mm and continues till it reaches a peak at x = 850 mm. In contrast, δ^* at downwash starts to decrease at x = 300 mm until reaching a minimum value at x = 550 mm. After reaching the maximum and minimum, δ^* at upwash and downwash begin to converge to the same value as a consequence of increased mixing due to the onset of transition to turbulence. Despite the large departures of δ^* at upwash and downwash from the Blasius curve, the streamwise development of the spanwise-averaged δ^* seems to follow the Blasius curve, although it is slightly thicker, especially in the upstream region. Similarly, the streamwise developments of boundary layer momentum thickness θ show approximately the same patterns as those of δ^*, as shown in Fig. 7.3.

The thickening of δ^* implies that more fluid from the outer flow is caught up by the retardation due to friction effect, which is given by viscous effect term

($v\partial^2 u/\partial y^2$) in the momentum equation. The viscous effect also causes outward momentum transport from the wall. These phenomena are shown in the development of the spanwise-averaged δ^* and θ in Figs. 7.2 and 7.3, respectively. The spanwise-averaged δ^* increases further downstream at a rate approximately the same with that of the Blasius curve, while the spanwise-averaged θ increases faster than the Blasius curve showing more momentum deficits in the concave surface boundary layer due to Görtler instability. However, the spanwise variation of both spanwise-averaged δ^* and θ, which is shown in Figs. 7.4 and 7.5 respectively, suggests that, unlike in flat-plate boundary layer, the viscous term in the spanwise direction ($v\partial^2 u/\partial z^2$) in the momentum equation cannot be ignored for concave surface boundary layer. This term, which is derived from the rate of strain $\partial u/\partial z$, appears in the momentum equation for the concave surface boundary layer flow as a result of the interaction between centrifugal force and the viscous effect, as well as radial pressure gradient. It is responsible for the thicker and thinner boundary layers at upwash and downwash, respectively, in addition to the Reynolds stresses. Girgis and Liu (2006) found that the mechanism of the normal (y) transport of streamwise momentum due to the secondary instabilty is that of Reynolds stress $-\overline{u'v'}$, in addition to the viscous diffusion.

The Reynolds stresses are important features in explaining the nonlinear secondary instability structures. The positive value of Reynolds stress $-\overline{u'v'}$ indicates that the high-momentum fluid is transported toward the wall from the outer flow giving rise to the y steepening of the steady flow streamwise velocity profile in the nonlinear region (Girgis and Liu, 2006). This suggests that the appearance of the secondary instability will inhibit the normal (y) development of the vortex structures, thus the displacement thickness at the upwash. If this is true, the sudden decrease of

the growth rate of the displacement thickness at x = 400 mm of the upwash curve, as shown in Fig. 7.2, may be explained by the effect of the Reynolds stress $-\overline{u'v'}$ as the secondary instability modes arise.

As discussed earlier, high-shear stress at downwash and low-shear stress at upwash will give rise to spanwise variation of boundary layer thickness. The distributions of both δ^* and θ, as shown in Figs. 7.4 and 7.5 respectively, are quite similar, that is, wavy profiles with the peaks at the upwash regions. At x = 200 mm, where Görtler instability is still in its linear development, the boundary layer thickness at downwash regions are spanwisely uniform. As a result of low-momentum fluid moving away from the wall at upwash, the mass and momentum deficits increase, as shown by thicker δ^* and θ respectively. Further downstream, as the velocity difference between the downwash and upwash increases, the rate of strain $\partial u/\partial z$ increases too. This may explain the sharper wavy profile at downwash and the inflected wavy profile at upwash further downstream, as shown in Figs. 7.4 and 7.5.

7.4 Wall Shear Stress Development

For a flat plate laminar boundary layer, the wall shear stress τ_w decreases with $x^{1/2}$ as the boundary layer grows, and increases with $U_\infty^{1.5}$ (see White (1999), for example). However, for a concave surface boundary layer in the presence of Görtler vortices, the wall shear stress varies in the spanwise (z) direction like the velocity profiles. The streamwise developments of τ_w in term of its coefficient C_f ($\equiv \tau_w/0.5\rho U_\infty^2$, where ρ is the fluid density) for case 2 (λ_m = 12 mm and U_∞ = 2.1 m/s) are presented in Fig. 7.6 at upwash and downwash together with the spanwise-averaged values. The wall shear stress curves for the Blasius and turbulent boundary

layer flows in a flat plate are also included in the figure for comparison. The turbulent curve was obtained from the semi-empirical equation of Blasius for turbulent boundary layer on smooth surface using one-seventh power law velocity profile, that is: $C_f = 0.0576/\mathrm{Re}_x^{1/5}$.

The wall shear stress at upwash decreases at a rate faster than the Blasius curve until x = 350 mm, as shown in Fig. 7.6. After reaching its minimum point, that is 59% of Blasius value at that position, it increases downstream to reach the Blasius curve. This slight increase of the wall shear stress may be due to the effect of the secondary instability which occurs slightly before the location of the minimum wall shear stress (Bottaro and Klingmann, 1996). Further downstream, the wall shear stress follows the Blasius curve closely until the decay of the mushroom-like structures at x = 850 mm. Cases 1 and 3 also show the similar trend that there is a range of streamwise (x) distance in the nonlinear region where the wall shear stress at upwash follows the Blasius curve. In contrast to the present results, the wall shear stress obtained by Swearingen and Blackwelder (1987) at upwash simply crossed the Blasius curve after reaching its minimum point, instead of following the curve. This might be due to their coarse hot-wire measurements, where only 10 streamwise velocities were measured across boundary layer and the nearest point to the wall was 1.0 mm. Please also note that Swearingen and Blackwelder (1987) measured in naturally developed Görtler vortices, while the present work deals with pre-set wavelength Görtler vortices.

At downwash, the wall shear stress initially decreases at the rate slightly lower than the Blasius curve, but at x = 250 mm it starts to increase significantly downstream until x = 550 mm. Subsequently, the increasing rate reduces abruptly further downstream. The streamwise (x) location where the increasing rate of the wall

shear stress starts to reduce corresponds to the turning point in the boundary layer displacement thickness (δ^*) curve at the downwash (Fig. 7.2). Downstream of this location, in contrast to a flat-plate boundary layer, the wall shear stress increases with increasing δ^*.

The spanwise-averaged curve in Fig. 7.6 also shows increasing wall shear stress from x = 300 mm. Computational studies (Sabry and Liu, 1991; Li and Liu, 1992; Girgis and Liu, 2006) explained that further enhancement of the wall shear stress is due to the effect of nonlinear steady streamwise Görtler vortices. In the absence of secondary instability, the spanwise-averaged wall shear stress coefficient $\overline{C}_f$ has already appeared to a large extent to bridge the Blasius curve and the flat-plate turbulent boundary layer curve. The presence of the secondary instability is to further increase $\overline{C}_f$ well beyond the turbulent values (Girgis and Liu, 2006). This finding may be useful in some engineering applications as increasing of wall shear stress suggests enhancement of heat transfer. In addition, the increasing wall shear stress, which is also observed in the transition region of flat-plate boundary layer flow, suggests that the growth and breakdown of Görtler vortices are quite similar to those in transitional and turbulent flow fields. Therefore, they can be used to experimentally model the eddy structures found in transitional and turbulent boundary layers (Bippes, 1978).

Görtler instability is considered to be in the nonlinear region when the horseshoe vortices are observed in the iso-velocity contours (Mitsudharmadi *et al*., 2004). The vortices are evolved from the wavy velocity profiles and subsequently transformed into the mushroom-like structures further downstream. The inflection points in both normal and spanwise directions, as a result of increasing shear stresses $\partial u/\partial y$ and $\partial u/\partial z$ respectively, are observed in the streamwise velocity profiles. The

nonlinear development also leads to an initial decrease of wall shear stress at the upwash (at upstream of x = 350 mm), prior to the subsequent slight increase due to the secondary instability, and an increase at the downwash (Bottaro and Klingmann, 1996), as also revealed in Fig. 7.6. However, the spanwise-averaged wall shear stress coefficient $\overline{C}_f$ is larger than that in the flat-plate boundary layer. As the flow becomes nonlinear, it is more susceptible to the secondary instability which will further increase $\overline{C}_f$. Girgis and Liu (2006) used the concept of Reynolds stresses to explain the nonlinear secondary instability of Görtler vortices. They concluded that the further enhancement of $\overline{C}_f$ is contributed by the Reynolds stress $-\overline{u'v'}$ in much the same way as in turbulent boundary layer, although they possess different fluctuation mechanisms.

As discussed earlier, the minimum wall shear stress at upwash occurs at x = 350 mm (Fig. 7.6), which is coincidentally the same location where the growth of the maximum disturbance amplitude $\kappa_{u,\max}$ [Eq. (4.1)] ceases and approaches a plateau. This streamwise location is assumed to be the onset of the nonlinear region of Görtler vortices (Mitsudharmadi *et al*., 2004), as shown in the Fig. 7.7. However, Bottaro and Klingmann (1996) showed that the secondary instability occurs slightly upstream of the location where the wall shear stress at upwash is minimum, which is at slightly upstream of x = 350 mm. These two findings seem to contradict since it is not possible that the secondary instability occurs before the onset of the nonlinear region. The flow becomes susceptible to the secondary instability only after it is sufficiently nonlinear and the energy saturates at a constant level. Therefore, the use of the maximum disturbance amplitude curve, as shown in Fig. 7.7 for case 2 of the present work, to predict the linear and nonlinear regions of Görtler instability may not be as

accurate. The wall shear stress data may provide a better indication of the onset of the nonlinear region since it is more sensitive than the $\kappa_{u,\max}$.

Based on the streamwise development of spanwise-averaged wall shear stress coefficient $\overline{C}_f$, three different regions can be identified, namely linear, nonlinear, and transition to turbulence regions, as shown in Fig. 7.6. In the linear region, $\overline{C}_f$ still follows the Blasius curve. In this region, the instability, as well as the perturbation energy, grows linearly, and therefore the linear stability analysis can still provide the satisfactory results. The nonlinear region is defined from the streamwise distance where $\overline{C}_f$ begins to depart from the Blasius curve (at x = 250 mm). The perturbation energy grows nonlinearly and finally reaches a saturation level where the flow becomes susceptible to the secondary instability. Lastly, the transition to turbulence region is shown by the increase and decrease of C_f at upwash and downwash respectively, eventually to converge to the same value, indicating the onset of the transition to turbulence and its consequence of increased mixing. The $\overline{C}_f$, as well as the turbulence intensity at upwash and downwash, in this region increase significantly.

The streamwise developments of the spanwise-averaged wall shear stress for all three cases are shown in Fig. 7.8. As the wall shear stress is presented in non-dimensional form (spanwise-averaged wall shear stress coefficient $\overline{C}_f$), the streamwise (x) distance is also presented in non-dimensional Görtler number G_θ. The results for all cases show the same development of $\overline{C}_f$, where it first decreases and then increases further downstream. The minima in all cases occur at about the same Görtler number G_θ = 4.0. After reaching its minimum point, it increases dramatically

with downstream distance until $G_\theta \approx 6.0$. Downstream of this streamwise (x) distance, the increasing rate of $\overline{C}_f$ reduces for a finite range of G_θ before a substantial increase occurs again as a result of increased mixing due to the onset of flow transition to turbulence.

As discussed earlier, the increase of $\overline{C}_f$ well above the local flat plate turbulent boundary layer value is due to the secondary instabilities. Furthermore, the secondary instabilities possess a close correlation with the rates of strain in which there is direct energy conversion from the primary motion to the secondary instability through the rates of strain, in addition to viscous dissipation. The motion of the sinuous mode is strongly correlated to the rate of strain $\partial u/\partial z$ of the primary motion, while the varicose mode is more related to the rate of strain $\partial u/\partial y$ (Yu and Liu, 1994). The energy conversion mechanism from the primary motion to the secondary instabilities is performed via the work of Reynolds stresses $-\overline{u'v'}$ and $-\overline{u'w'}$ against the rates of strain of the primary motion $\partial u/\partial y$ and $\partial u/\partial z$, respectively. Bottaro *et al*. (1996) found that the growth of the perturbation kinetic energy will level off in the nonlinear region, and finally lead to a state where the energy saturates at a constant level. It explains why the increasing rate of $\overline{C}_f$ reduces in a finite range of Görtler number prior to the flow transition to turbulence.

It is evident that the type of the secondary instability mode, which of course affects the development of the wall shear stress, is directly influenced by Görtler vortex wavelength (Li and Malik, 1995). Additionally, the Görtler number distribution may have some bearing on the secondary instability mechanism indirectly through its effect on the development of Görtler vortices and their wavelengths relative to the boundary layer thickness. These evidences may explain the difference

in increasing rate of $\overline{C}_f$ among the three cases downstream of $G_\theta \approx 6.0$. Furthermore, it would be interesting to investigate the influence of each mode of secondary instability to the increasing rate of wall shear stress in concave surface boundary layer.

Although it follows the same trend as those in case 1 (λ_m = 12 mm and U_∞ = 2.8 m/s) and case 2 (λ_m = 15 mm and U_∞ = 2.1 m/s), $\overline{C}_f$ in case 3 (λ_m = 20 mm and U_∞ = 1.3 m/s) is larger than those in cases 1 and 2 for the same Görtler number. To explain this phenomenon, $\overline{C}_f$ is plotted against Reynolds number Re_θ ($\equiv U_\infty \theta / \nu$), as shown in Fig. 7.9. Before reaching their minima, $\overline{C}_f$ for all cases seems to follow the same line. The values of Re_θ at the minima are respectively 150, 140, and 110 for case 1, 2, and 3. Larger vortices reach their minima at lower Re_θ values which could be because larger vortices are more "vigorous" (Bottaro *et al*., 1996). In the nonlinear region, larger vortices consistently produce higher wall shear stress at any value of Re_θ.

Associated with the nonlinear region of Görtler vortices, the spanwise distributions of the mean velocity u/U_∞ become distorted such that the downwash becomes flat and the upwash becomes narrow and sharp (Aihara, 1976; Aihara and Koyama, 1981), as shown in Fig. 7.10 at a distance $y = 0.5\delta_L$ (where δ_L is Blasius boundary layer thickness) at several streamwise positions. The broken-line refers to the spanwise-averaged value of u/U_∞ at the corresponding streamwise (x) position. There is a tendency of wavy velocity distribution to approach a finite amplitude, which can be quantified by the maximum disturbance amplitude $\kappa_{u,\max}$, as the flow becomes sufficiently nonlinear.

The spanwise distributions of u/U_∞ at downwash region at x = 200 mm (Fig. 7.10(a)) and 300 mm (Fig. 7.10(b)) are not as flat as that at x = 400 mm (Fig. 7.10(c)). The "kinks" at the downwash indicate that other disturbances, besides the one generated by thin vertical wires, are present in the flow. However, at x = 400 mm the "kinks" disappear, resulting in a flat spanwise distribution at downwash region before being inflected due to the secondary instability. The appearance of the "kinks" in the spanwise distributions of u/U_∞ at the early stage of boundary layer indicates that Görtler instability amplifies the disturbances imposed by the rig facilities on the incoming flow (Kottke, 1988), including the disturbances generated by the perturbation wires. A competition of disturbances of different amplification rates, as the only wavelength selection mechanism of Görtler vortices, damps the disturbances other than the one generated by the wires, resulting in a uniform wavelength of Görtler vortices that preserves itself downstream.

As the growth of the vortices in the y direction reaches a finite amplitude, the spanwise distribution of u/U_∞ is then inflected, as shown in Fig. 7.10(d) to (h), and the flow is dominated by the mushroom-like structures. The inflected velocity profiles in the spanwise direction, as well as the inflected velocity profiles across the boundary layer which occur earlier, indicate the appearance of the secondary instability. Further investigation reveals that it is related to the sinuous mode of secondary instability (Swearingen and Blackwelder, 1987).

The spanwise distributions of the wall shear stress in term of C_f for several streamwise positions are presented in Fig. 7.11, where the broken-line is the spanwise-averaged value $\overline{C}_f$ at the corresponding streamwise position. Initially, the spanwise distribution of C_f seems to correlate with the spanwise distribution of

u/U_∞ until x = 300 mm. Further downstream, there is no indication of the spanwise distribution of C_f to become flat at the downwash and narrow or sharp at the upwash, as observed in the spanwise distribution of u/U_∞. Instead, the C_f distribution at the downwash region becomes narrower, and there is no inflection point found in the distribution. This may be because the sinuous mode of secondary instability, which is initiated near the boundary layer edge, is not strong enough to alter the distribution of the wall shear stress. This also explains why the increasing rate of $\overline{C}_f$ (in Fig. 7.6) reduces significantly prior to the flow transition to turbulence. The main contribution to the wall shear stress enhancement in a concave surface boundary layer flow may be attributed to the varicose mode of the secondary instability. This is concluded from the fact that the waviness in C_f distribution becomes more pronounced and the spanwise-averaged value $\overline{C}_f$ increases significantly at the early stage of the nonlinear region where the flow instability, in the present work, is still dominated by the varicose mode.

7.5 Concluding Remarks

The streamwise development of wall shear stress in Görtler vortex boundary layer flows has been experimentally studied on a concave surface of radius of curvature R = 1.0 m for three different cases of different wire spacing and different free-stream velocities. The wall shear stress was estimated by using the near-wall velocity gradient technique. Near-wall velocity measurements with a very fine step-size were carried out to obtain sufficient streamwise velocity data within the “linear” layer.

The boundary layer displacement and momentum thicknesses develop further downstream in a similar pattern. Initially, both boundary layer displacement and momentum thicknesses increase at the rate similar to the Blasius curve until a certain streamwise location for both upwash and downwash. Further downstream, they depart from the Blasius curve in such a way that they increase at upwash and decrease at downwash before finally converging to the same value due to the enhanced mixing as a consequence of the transition to turbulence. The streamwise development of the spanwise-averaged boundary layer displacement thickness seems to follow the Blasius curve indicating that the net mass transport from the outer flow into the boundary layer is somewhat similar to that of the flat-plate boundary layer. However, the spanwise-averaged momentum thickness increases at the rate higher than the Blasius curve, showing more momentum deficits in the concave surface boundary layer, compared with the flat-plate boundary layer, due to the Görtler instability.

The wall shear stress at downwash initially decreases at a slightly lower rate than the Blasius curve, and subsequently increases after reaching its minimum point. In contrast, the wall shear stress at upwash region decreases at a higher rate than the Blasius curve. The minimum wall shear stress is found to be 59% of the Blasius value at that position. After reaching its minimum point, the wall shear stress increases slightly due to the secondary instability as the onset of secondary instability is just slightly before the location of the minimum wall shear stress at the upwash. The spanwise-averaged wall shear stress coefficient $\overline{C}_f$, which initially follows the Blasius curve, increases well above the local turbulent boundary layer value further downstream due to the nonlinear effects of Görtler instability and the secondary instability modes.

The wall shear stress data provides a more accurate indication of the onset of nonlinear region than the $\kappa_{u,\max}$ criterion (Mitsudharmadi *et al*., 2004). Three different regions can be identified based on the streamwise development of spanwise-averaged wall shear stress coefficient $\overline{C}_f$, namely linear, nonlinear, and transition to turbulence. The onset of the nonlinear region is defined as the streamwise location where $\overline{C}_f$ starts to depart from the Blasius curve. The transition to turbulence is initiated by a significant increase in $\overline{C}_f$. At the same time, the wall shear stress at upwash also drastically increases, but it decreases at downwash as a result of increased mixing due to turbulence.

Unlike the spanwise distribution of streamwise velocity, the spanwise distribution of C_f becomes narrower at the downwash in the nonlinear region, and there is no inflection point found further downstream. This may be because the sinuous mode of the secondary instability is not strong enough to alter the spanwise distribution of the wall shear stress. The reduction in the increasing rate of $\overline{C}_f$ in the later part of the nonlinear region, where the instability is dominated by the sinuous mode, seems to suggest that the main contribution to the wall shear stress enhancement in a concave surface boundary layer flow may come from the varicose mode of the secondary instability.

CHAPTER 8

CONCLUSIONS AND RECOMMENDATIONS

8.1 Conclusions

The development of the most amplified wavelength Görtler vortices has been experimentally studied by means of hot-wire anemometer measurements. Three different cases were investigated on a concave surface of 1.0 m radius of curvature by using different vortex wavelengths and different free-stream velocities but keeping the wavelength parameter Λ = 250 to produce the most amplified wavelength Görtler vortices. The three cases include: (1) λ_m = 12 mm and U_∞ = 2.8 m/s, (2) λ_m = 15 mm and U_∞ = 2.1 m/s, and (3) λ_m = 20 mm and U_∞ = 1.3 m/s. The wavelengths of the vortices were "forced" or pre-set by means of a series of 0.2 mm diameter vertical perturbation wires positioned 10 mm prior and perpendicular to the concave surface leading edge.

The streamwise velocity measurements have been carried out by means of a single-normal (*SN*) hot-wire probe. The vortex wavelengths were observed to preserve downstream for all cases. This shows that the vertical perturbation wires can be effectively used to pre-set the wavelength of Görtler vortices and confirms the most amplified wavelength Görtler vortices as predicted by Görtler vortex stability diagram. The wavy profiles caused by the perturbation wires are amplified downstream to form "horseshoe" vortices and subsequently "mushroom-like" structures in the nonlinear region before turbulence sets in. The onset of nonlinear region is initiated by the departure of the perturbation energy from its quasi-

exponential growth to reach a saturation level. As the flow is sufficiently nonlinear, it becomes susceptible to the secondary instability.

Two inflection points were observed in the velocity profiles across the boundary layer in the nonlinear region. The first inflection point appears in the velocity profile at the upwash near the boundary layer edge. The location of the inflection point corresponds to the region where intense turbulence is found in the turbulence intensity (Tu) contours. As the velocity defect grows progressively upward, a second inflection point subsequently appears in the region between the concave surface and the boundary layer edge, and the velocity profile evolves to become an **S**-shape. The appearance of the first inflection point implies that high-shear layer occurs near the boundary layer edge. The high-shear layer subsequently triggers the appearance of horseshoe vortices as the secondary instability of Görtler vortices.

The spanwise distribution of streamwise velocity $u(z)$ at the vortex stem region is narrow and sharp at upwash and wide and flat at downwash. In contrast, the velocity distribution at mushroom head region becomes wide and flat at upwash further downstream. However, no inflection points are observed at both sinusoidal patterns of the velocity distributions. The inflection points are found only in the region between the stem and mushroom head regions. The appearance of the second inflection point in the normal velocity profile is followed by the appearance of the inflection point in the spanwise distribution of $u(z)$. These inflection points are related to the sinuous mode of secondary instability that leads the flow into turbulence.

Comparison of the present results with the previous results of different radii of curvature has been carried out. The vortex growth rate is expressed in term of maximum disturbance amplitude $\kappa_{u,\max}$, which is also the amplitude of the first mode

of the spanwise harmonics of streamwise velocity. For smaller radius of curvature, the vortices are found to grow faster in the linear region due to the stronger centrifugal force. The onset of nonlinear region therefore occurs at a more upstream streamwise location for the case of smaller radius of curvature, and it is independent of free-stream velocity. When $\kappa_{u,\max}$ is plotted against the Görtler number G_θ, all data obtained from the same experimental set-up seem to lie on a single line, regardless of the values of free-stream velocity and concave surface radius of curvature.

The spectral analysis was performed by using Fast Fourier Transform (FFT) to investigate the spanwise harmonics of streamwise velocity and frequency characteristics of Görtler vortices for case 1. The periodic streamwise velocity along spanwise can be represented by at least two first modes (N = 2) of the Fourier series. Higher modes will appear only in the nonlinear region before finally all modes die down as a consequence of transition to turbulence. Two dominant frequencies of 140 Hz and 180 Hz were observed in the power spectral density of streamwise velocity at the side of vortex stems in the nonlinear region. The second harmonics of these frequencies are found to be significant at the middle of upwash, especially at normal (y) locations near half bondary layer thickness.

Streamwise and spanwise velocity components, u and w, have been maeasured by means of X-wire for the nonlinear region of case 1 (λ_m = 12 mm and U_∞ = 2.8 m/s). The appearance of streamwise counter-rotating vortices is shown clearly in the spanwise velocity profiles across the boundary layer, as well as the spanwise velocity contours in the y-z plane, in which the regions of positive and negative w are observed across the boundary layer in an alternate way. The secondary motion, as a result of the amplification of free-stream disturbances, appears in the vortex's head due to the secondary instability.

Two dominant peaks correspond to the frequencies of 70 Hz and 90 Hz initially appear in the spectra of *w*. The frequencies of 140 Hz and 180 Hz, which are found earlier to be related with the streamwise velocity, consecutively appear and dominate the flow further downstream. All peaks in the spectral distributions die down as the flow turns into turbulent, and the power spectral density is distributed uniformly along the frequency band of 20 Hz to 100 Hz. The most unstable frequencies are found exactly at the intense region of $\overline{w'^2}$-contours. Two intense regions of $\overline{w'^2}$ are found at the stem and head of the vortex structures, with the most intense region is at the vortex's stem. This implies that the mushroom-like structures oscillate in the spanwise direction, intensely at the stem and head of the vortices. The Reynolds shear stress $-\overline{u'w'}$ contour, which resembles the $\partial u/\partial z$ iso-shear contours, suggests that the energy conversion mechanism from primary to secondary motions $-\overline{u'w'}\,\partial u/\partial z$ also occurs at the stem and head of the vortices, in which the most intense values are on the sides of the stem region.

Near wall velocity measurements have also been carried out by means of single-normal (*SN*) hot-wire probe to study the streamwise development of wall shear stress in Görtler vortex boundary layer flows. The region with the "linear" velocity profile in the concave surface boundary layer prior to turbulence is sufficiently thick to estimate the wall shear stress. Therefore, the near-wall velocity gradient technique (Hutchins and Choi, 2002) has been used to estimate the wall shear stress based on the slope of the "linear" layer.

The wall shear stress at downwash decreases at a slightly lower rate than the Blasius curve and it subsequently increases after reaching its minimum point. In contrast, the wall shear stress at upwash decreases at a higher rate than the Blasius curve. After reaching its minimum point, it increases slightly due to secondary

instability as the onset of secondary instability occurs slightly before the location of the minimum wall shear stress at the upwash. The spanwise-averaged wall shear stress, which initially follows the Blasius curve, increases well above the value of the local flat plate turbulent boundary layer further downstream. This may be attributed to the nonlinear effect of Görtler instability and the secondary instability modes.

The spanwise distribution of wall shear stress coefficient C_f exhibits a sinusoidal pattern with lower C_f at upwash and higher at downwash. Unlike the spanwise distribution of streamwise velocity, the spanwise distribution of C_f becomes narrower at downwash in the nonlinear region, and there is no inflection point found further downstream. This may be because the sinuous mode of secondary instability is not strong enough to alter the spanwise distribution of the wall shear stress.

The wall shear stress data provides a more accurate indication of the onset of nonlinear region than the $\kappa_{u,\max}$ criterion (Mitsudharmadi *et al*., 2004). Three different regions can be identified based on the streamwise development of spanwise-averaged wall shear stress coefficient $\overline{C}_f$, namely linear, nonlinear, and transition to turbulence. The onset of the nonlinear region is defined as the streamwise location where $\overline{C}_f$ starts to depart from the Blasius curve. The transition to turbulence is initiated by a significant increase in $\overline{C}_f$. At the same time, the wall shear stress at upwash also drastically increases, but it decreases at downwash as a result of increased mixing due to turbulence.

8.2 Recommendations

The following recommendations can be considered for future works:

1. The success of pre-setting the wavelength of Görtler vortices by means of a series of vertical wires make it possible to control and study the development of Görtler vortices. Other methods to pre-set Görtler vortex wavelength may also be considered, for example, by introducing saw-tooth pattern at the leading edge of concave surface as recently reported by Akaishi *et al*. (2007).
2. The resulting wavelength of Görtler vortices follows the spanwise distance between the wires, and preserves downstream. It will be interesting to concurrently pre-set the Görtler vortices with the different wavelengths near the leading edge. The development of the vortices can be subsequently investigated. This may give a clearer picture about the wavelength selection mechanism of Görtler vortices that is still not understood yet.
3. The physical flow visualizations, for example: smoke visualization, can be tried to compliment the present quantitative data obtained by hot-wire anemometer. However, the safety regulations in the laboratory made it not possible to carry out the smoke visualization. An attempt will be worthy to be made in the future to provide more detailed pictures of the development of the most amplified wavelength Görtler vortices.
4. The wall shear stress results estimated from the near-wall velocity gradient technique confirm a substantial increase of wall shear stress, thus heat transfer enhancement, at the downwash of the nonlinear region of Görtler vortices. Further investigation on wall shear stress, as well as heat transfer enhancement, in Görtler vortex flows can therefore be considered. Velocity and temperature measurements inside the concave surface boundary layer can be carried out in the future.
5. Comparison between computational simulations and experimental studies is very important, in order to gain a better understanding on the physical insights of the

phenomenon. Hence, computational simulations on Görtler vortex boundary layer flows should be attempted. The flow simulation and modeling can be carried out by a computational fluid dynamics (CFD) software, such as ANSYS Fluent or ANSYS CFX, coupled with the user-defined functions (UDF) that allow us to enhance the standard features of the software.

REFERENCES

Aihara, Y., "Nonlinear analysis of Görtler vortices," *Physics of Fluids*, **19**, 1655 (1976).

Aihara, Y., "Görtler vortices in the nonlinear region," in *Recent developments in theoretical and experimental fluid mechanics: Compressible and incompressible flows*, edited by Muller, U., Roesner, K. G., and Schmidt, B. (Springer-Verlag, Berlin, 1979), pp. 331-338.

Aihara, Y. and Koyama, H., "Secondary instability of Görtler vortices: Formation of periodic three-dimensional coherent structure," *Transactions of the Japan Society for Aeronautical and Space Sciences*, **24**, 78 (1981).

Ajakh, A., Kestoras, M., and Peerhossaini, H., "Experiments on the Görtler instability: its relation to transition to turbulence," in *Proceedings of the 1996 ASME Fluids Engineering Division Summer Meeting. Part 2 (of 3)*, San Diego, 1996, (ASME, New York, 1996), pp. 613-621.

Ajakh, A., Kestoras, M. D., Toe, R., and Peerhossaini, H., "Influence of forced perturbations in the stagnation region on Görtler instability," *AIAA Journal*, **37**, 1572 (1999).

Akaishi, K., Nishikawa, H., Jumonji, K., and Ito, A., "Visualization of secondary instability flows generated between forced wavelength Görtler vortices," *The 9th Asian Symposium on Visualization*, 4-8 June 2007, Hong Kong, ASV0008-002.

Alfredsson, P. H., Johansson, A. V., Haritonidis, J. H., and Eckelmann, H., "The fluctuating wall-shear stress and the velocity field in the viscous sublayer," *Physics of Fluids*, **31**, 1026 (1988).

Azad, R. S. and Burhanuddin, S., "Measurements of some features of turbulence in wall-proximity," *Experiments in Fluids*, **1**, 149 (1983).

Bassom, A. P. and Hall, P., "Receptivity problem for O(1) wavelength Goertler vortices," *Proceedings of the Royal Society of London, Series A: Mathematical, Physical and Engineering Sciences*, **446**, 499 (1994).

Bhatia, J. C., Durst, F., and Jovanovic, J., "Corrections of hot-wire anemometer measurements near walls," *Journal of Fluid Mechanics*, **122**, 411 (1982).

Bippes, H., "Experimental study of the laminar-turbulent transition of a concave wall in a parallel flow," NASA TM-75243 (1978).

Blackwelder, R. F. and Haritonidis, J. H., "Scaling of the bursting frequency in turbulent boundary layers," *Journal of Fluid Mechanics*, **132**, 87 (1983).

Bottaro, A. and Klingmann, B. G. B., "On the linear breakdown of Görtler vortices," *European Journal of Mechanics, B/Fluids*, **15**, 301 (1996).

Bottaro, A., Klingmann, B. G. B., and Zebib, A., "Goertler vortices with system rotation," *Theoretical and Computational Fluid Dynamics*, **8**, 325 (1996).

Box, G. E. P., Hunter, W. G., and Hunter, J. S., *Statistics for experimenters: an introduction to design, data analysis, and model building* (John Wiley & Sons, Inc., New York, 1978).

Bruun, H. H., *Hot-wire anemometry: principles and signal analysis* (Oxford Unversity Press, Oxford, 1995).

Chew, Y. T., Khoo, B. C., and Li, G. L., "A time-resolved hot-wire shear stress probe for turbulent flow: use of laminar flow calibration," *Experiments in Fluids*, **17**, 75 (1994).

Dagenhart, J. R. and Mangalam, S. M., "Disturbance functions of the Görtler instability on an airfoil," AIAA Paper 86-1048, 1986.

Dean, W. R., "Fluid motion in a curved channel," *Proceedings of the Royal Society of London. Series A, Containing Papers of a Mathematical and Physical Character*, **121**, 402 (1928).

Denier, J. P., Hall, P., and Seddougui, O., "On the receptivity problem for Görtler vortices: vortex motions induced by wall roughness," *Philosophical Transactions of the Royal Society, Series A (Physical Sciences and Engineering)*, **335**, 51 (1991).

Finnis, M. V. and Brown, A., "Stability of a laminar boundary layer flowing along a concave surface," *Journal of Turbomachinery*, **111**, 376 (1989).

Finnis, M. V. and Brown, A., "The linear growth of Görtler vortices," **18**, 389 (1997).

Floryan, J. M., "Görtler instability of boundary layers over concave and convex walls," *Physics of Fluids*, **29**, 2380 (1986).

Floryan, J. M., "On the Görtler instability of boundary layers " *Progress in Aerospace Sciences*, **28**, 235 (1991).

Floryan, J. M. and Saric, W. S., "Stability of Görtler vortices in boundary layers," *AIAA Journal*, **20**, 316 (1982).

Girgis, I. G. and Liu, J. T. C., "Nonlinear mechanics of wavy instability of steady longitudinal vortices and its effect on skin friction rise in boundary layer flow," *Physics of Fluids*, **18**, 024102 (2006).

Görtler, H., "Über eine dreidimensionale Instabilität laminarer Grenzschichten an konkaven Wänden", Ges. D. Wiss. Göttingen, Nachr. a. d., Math., 2 (1) (1940); translated as "On the three-dimensional instability of laminar boundary layers on concave walls", NACA TM 1375 (1954).

Hall, P., "The linear development of Görtler vortices in growing boundary layers," *Journal of Fluid Mechanics*, **130**, 41 (1983).

Hall, P., "The Görtler vortex instability mechanism in three-dimensional boundary layers," *Proceedings of the Royal Society of London, Series A (Mathematical and Physical Sciences)*, **399**, 135 (1985).

Hall, P., "Görtler vortices in growing boundary layers: The leading edge receptivity problem, linear growth and the non-linear breakdown stage," NASA CR-181962 (ICASE Report No. 89-81) (1989).

Hall, P. and Horseman, N. J., "Linear inviscid secondary instability of longitudinal vortex structures in boundary layers," *Journal of Fluid Mechanics*, **232**, 357 (1991).

Hanratty, T. J. and Campbell, J. A., "Measurement of wall shear stress," in *Fluid mechanics measurements*, edited by Goldstein, R. J. (Hemisphere Publishing, Washington DC, 1983), pp. 559-615.

Herbert, T., "Higher eigenstates of Görtler vortices," in *Recent developments in theoretical and experimental fluid mechanics: Compressible and incompressible flows*, edited by Muller, U., Roesner, K. G., and Schmidt, B. (Springer-Verlag, Berlin, 1979), pp. 322-330.

Hinze, J. O., *Turbulence. An introduction to its mechanism and theory* (McGraw-Hill, New York, 1959).

Hutchins, N. and Choi, K.-S., "Accurate measurements of local skin friction coefficient using hot-wire anemometry," *Progress in Aerospace Sciences*, **38**, 421 (2002).

Kottke, V., "On the instability of laminar boundary layer along a concave wall towards Görtler vortices," in *Propagation and non equilibrium systems* (Springer, Berlin, 1988).

Kottke, V. and Mpourdis, B., "On the existence of Taylor-Görtler vortices on concave walls," in *Proceedings of the Fourth International Symposium*, Paris, 1986, (Hemisphere, Washington, 1987), pp. 475-480.

Li, F. and Malik, M. R., "Fundamental and subharmonic secondary instabilities of Görtler vortices," *Journal of Fluid Mechanics*, **297**, 77 (1995).

Liepmann, H. W., "Investigations on laminar boundary layer stability and transition on curved boundaries," NACA Wartime Report ACR No. 3H30 (1943).

Ligrani, P. M. and Bradshaw, P., "Spatial resolution and measurement of turbulence in the viscous sublayer using subminiature hot-wire probes," *Experiments in Fluids*, **5**, 407 (1987).

Ligrani, P. M. and Bradshaw, P., "Subminiature hot-wire sensors: development and use," *Journal of Physics E: Scientific Instruments*, **20**, 323 (1987).

Liu, J. T. C., "Nonlinear instability of developing streamwise vortices with applications to boundary layer heat transfer intensification through an extended Reynolds analogy," *Philosophical Transaction of The Royal Society A*, **366**, 2699 (2008).

Luchini, P. and Bottaro, A., "Görtler vortices: a backward-in-time approach to the receptivity problem," *Journal of Fluid Mechanics*, **363**, 1 (1998).

Mangalam, S. M., Dagenhart, J. R., Hepner, T. E., and Meyers, J. F., "Görtler instability on an airfoil," AIAA Paper 85-0491, 1985.

Matsson, O. J. E., "Experiments on streamwise vortices in curved wall jet flow," *Physics of Fluids*, **7**, 2978 (1995).

McCormack, P. D., Welker, H., and Kelleher, M., "Taylor-Goertler vortices and their effect on heat transfer," *Transactions of the ASME. Series C, Journal of Heat Transfer*, **92**, 101 (1970).

Meksyn, D., "Stability of viscous flow over concave cylindrical surfaces," *Proceedings of the Royal Society of London. Series A, Mathematical and Physical Sciences*, **203**, 253 (1950).

Mitsudharmadi, H., Winoto, S. H., and Shah, D. A., "Development of boundary-layer flow in the presence of forced wavelength Görtler vortices," *Physics of Fluids*, **16**, 3983 (2004).

Mitsudharmadi, H., Winoto, S. H., and Shah, D. A., "Secondary instability in forced wavelength Görtler vortices," *Physics of Fluids*, **17**, 074104 (2005a).

Mitsudharmadi, H., Winoto, S. H., and Shah, D. A., "Splitting and merging of Görtler vortices," *Physics of Fluids*, **17**, 124102 (2005b).

Mitsudharmadi, H., Winoto, S. H., and Shah, D. A., "Development of most amplified wavelength Görtler vortices," *Physics of Fluids*, **18**, 014101 (2006).

Momayez, L., Dupont, P., Delacourt, G., Lottin, O., and Peerhossaini, H., "Genetic algorithm based correlations for heat transfer calculation on concave surfaces," *Applied Thermal Engineering*, **29**, 3476 (2009).

Orlando, A. F., Moffat, R. J., and Kays, W. M., "Turbulent transport of heat and momentum in a boundary layer subject to deceleration, suction and variable wall temperature," NASA CR-139655 (1974).

Park, D. S. and Huerre, P., "Primary and secondary instabilities of the asymptotic suction boundary layer on a curved plate," *Journal of Fluid Mechanics*, **283**, 249 (1995).

Park, S. R. and Wallace, J. M., "Flow field alteration and viscous drag reduction by riblets in a turbulent boundary layer," in *Proceedings of the International Conference on Near-Wall Turbulent Flows*, Tempe, AZ, USA, 1993, (Elsevier Science Publishers B.V., Amsterdam, 1993), pp. 749-760.

Peerhossaini, H., "On the subject of Görtler vortex," in *Cellular structures in instability*, edited by Wesfreid, J. E. and Zaleski, S. (Springer, Berlin, 1984), pp. 376-384.

Peerhossaini, H. and Bahri, F., "On the spectral distribution of the modes in nonlinear Görtler instability," *Experimental Thermal and Fluid Science*, **16**, 195 (1998).

Polyakov, A. F. and Shindin, S. A., "Peculiarities of hot-wire measurements of mean velocity and temperature in the wall vicinity," *Heat and Mass Transfer*, **5**, 53 (1978).

Sabry, A. S. and Liu, J. T. C., "Longitudinal vorticity elements in boundary layers. Nonlinear development from initial Goertler vortices as a prototype problem," *Journal of Fluid Mechanics*, **231**, 615 (1991).

Schmidt, P. J. and Henningson, D. S., *Stability and transition in shear flows* (Springer, New York, 2001).

Shigemi, M., Johnson, M. W., and Gibbings, J. C., "Boundary layer transition on a concave surface," IMechE Paper No. C262/87, 1987.

Smith, A. M. O., "On the growth of Taylor-Görtler vortices along highly concave walls," *Quarterly of Applied Mathematics*, **13**, 233 (1955).

Swearingen, J. D. and Blackwelder, R. F., "Growth and breakdown of streamwise vortices in the presence of a wall," *Journal of Fluid Mechanics*, **182**, 255 (1987).

Syred, N., Khalatov, A., Kozlov, A., Shchukin, A., and Agachev, R., "Effect of surface curvature on heat transfer and hydrodynamics within a single hemispherical dimple," *ASME J. Turbomachinery*, **123**, 609 (2001).

Tandiono, Kelvin Neo C. T., Winoto, S. H., and Shah, D. A., "Pre-setting Görtler vortices using perturbation needles", *The 3rd International Symposium on*

Advanced Fluid/Solid Science and Technology in Experimental Mechanics, 7-10 December 2008, Tainan, Taiwan, Paper No. 122 (2008a).

Tandiono, Winoto, S. H., and Shah, D. A., "On the linear and nonlinear development of Görtler vortices", *Physics of Fluids*, **20**, 094103 (2008b).

Tandiono, Winoto, S. H., and Shah, D. A., "Visualizing shear stress in Görtler vortex flow", *Journal of Visualization*, **12**, 195 (2009a).

Tandiono, Winoto, S. H., and Shah, D. A., "Wall shear stress in Görtler vortex boundary layer flow", *Physics of Fluids*, **21**, 084106 (2009b).

Tani, I., "Production of longitudinal vortices in the boundary layer along a concave wall," *Journal of Geophysical Research*, **67**, 3075 (1962).

Taylor, G. I., "Experiments with rotating fluids," *Proceedings of the Royal Society of London. Series A, Containing Papers of a Mathematical and Physical Character*, **100**, 114 (1921).

Toe, R., Ajakh, A., and Peerhossaini, H., "Heat transfer enhancement by Görtler instability," *International Journal of Heat and Fluid Flow*, **23**, 194 (2002).

White, F. M., *Fluid Mechanics* (McGraw-Hill, Boston, 1999), 4 ed.

Winoto, S. H. and Crane, R. I., "Vortex structure in laminar boundary layers on a concave wall," *International Journal of Heat and Fluid Flow*, **2**, 221 (1980).

Winoto, S. H. and Low, H. T., "Transition of boundary layer flows in the presence of Goertler vortices," *Experiments in Fluids*, **8**, 41 (1989).

Winoto, S. H. and Low, H. T., "Transition of boundary layer flows in the presence of Goertler vortices," *Experiments in Fluids*, **10**, 281 (1991).

Winter, K. G., "An outline of the techniques available for the measurement of skin friction in turbulent boundary layers," *Progress in Aerospace Sciences*, **18**, 1 (1979).

Wortmann, F. X., "Visualization of transition," *Journal of Fluid Mechanics*, **38**, 473 (1969).

Yu, X. and Liu, J. T. C., "The secondary instability of Görtler flow," *Physics of Fluids A*, **3**, 1845 (1991).

Yu, X. and Liu, J. T. C., "On the mechanism of sinuous and varicose modes in three-dimensional viscous secondary instability of nonlinear Görtler rolls," *Physics of Fluids*, **6**, 736 (1994).

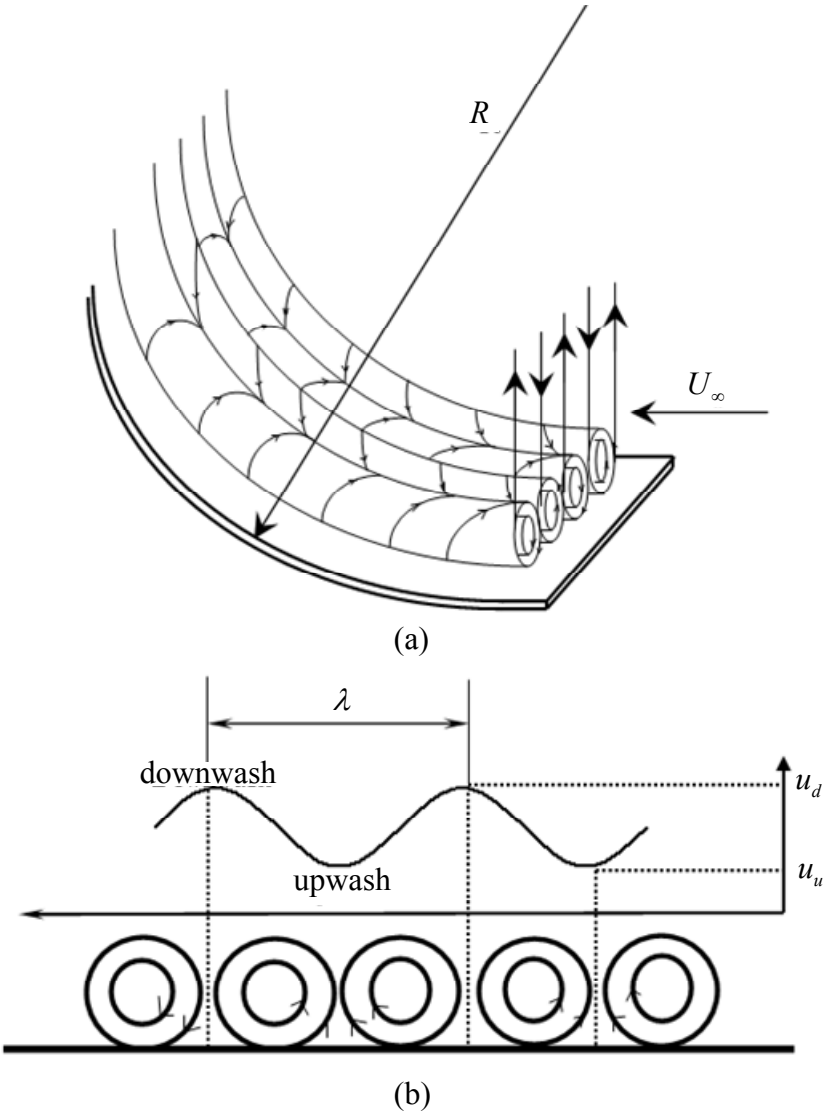

FIG. 1.1 Sketch of Görtler vortices and the definitions of upwash, downwash, and vortex wavelength.

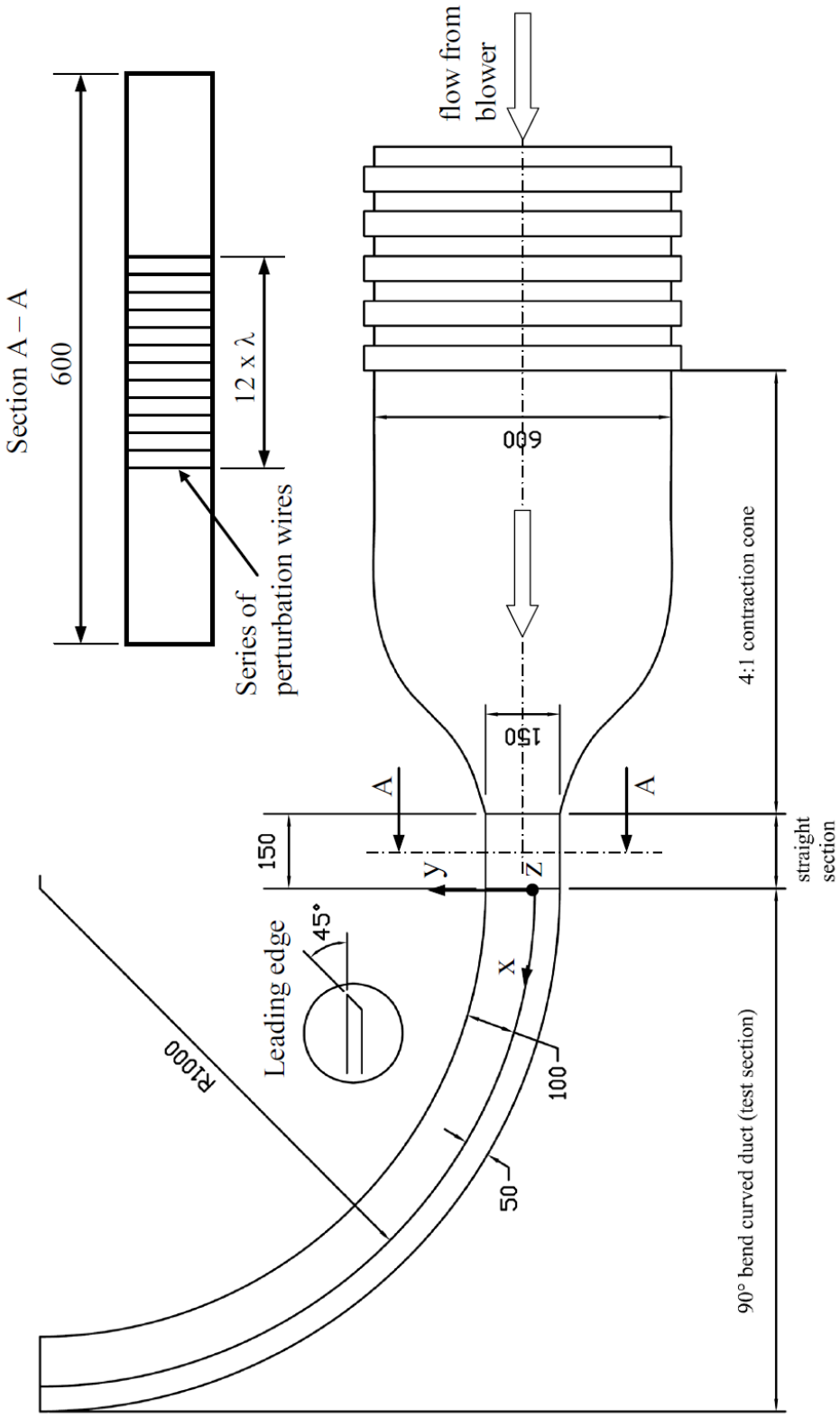

FIG. 3.1 Schematic of experimental set-up (all dimensions are in mm).

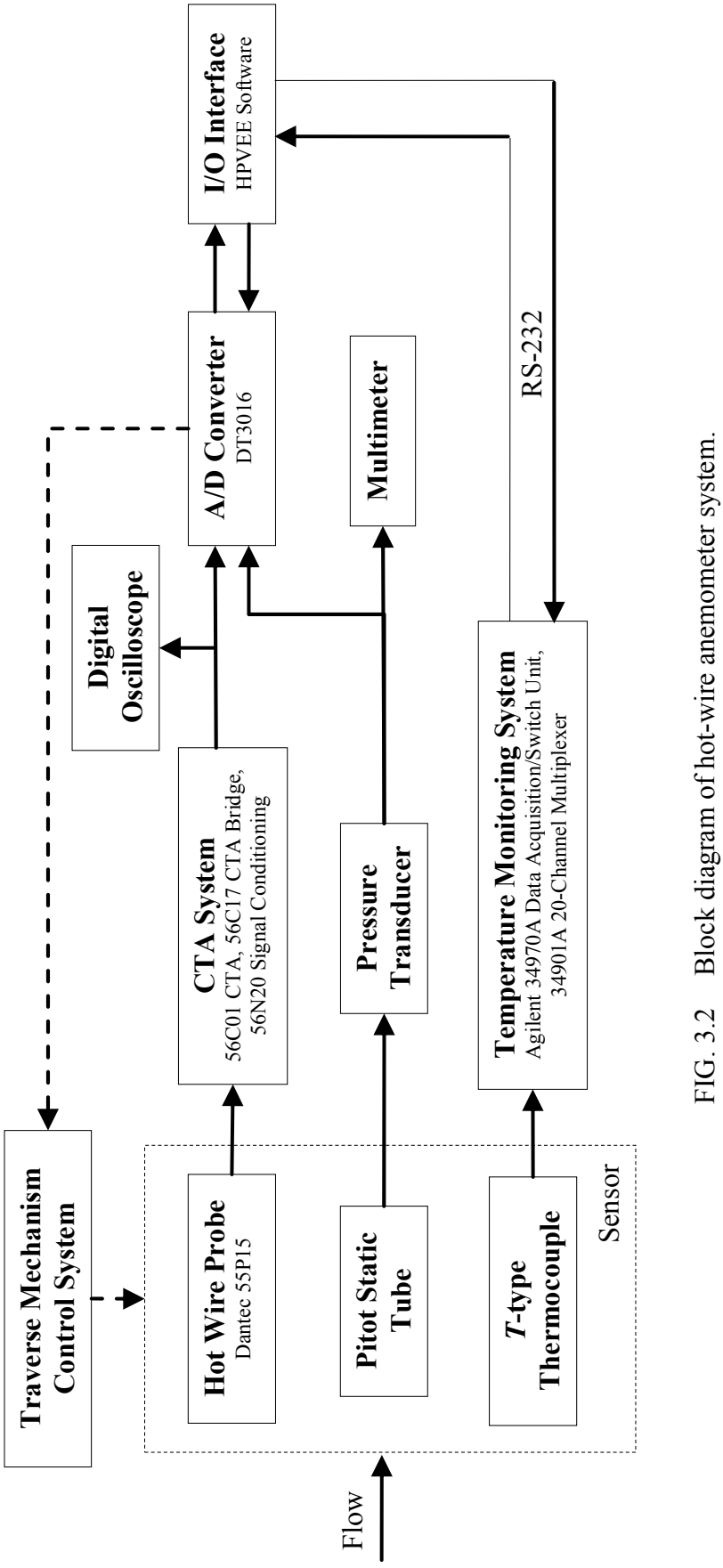

FIG. 3.2 Block diagram of hot-wire anemometer system.

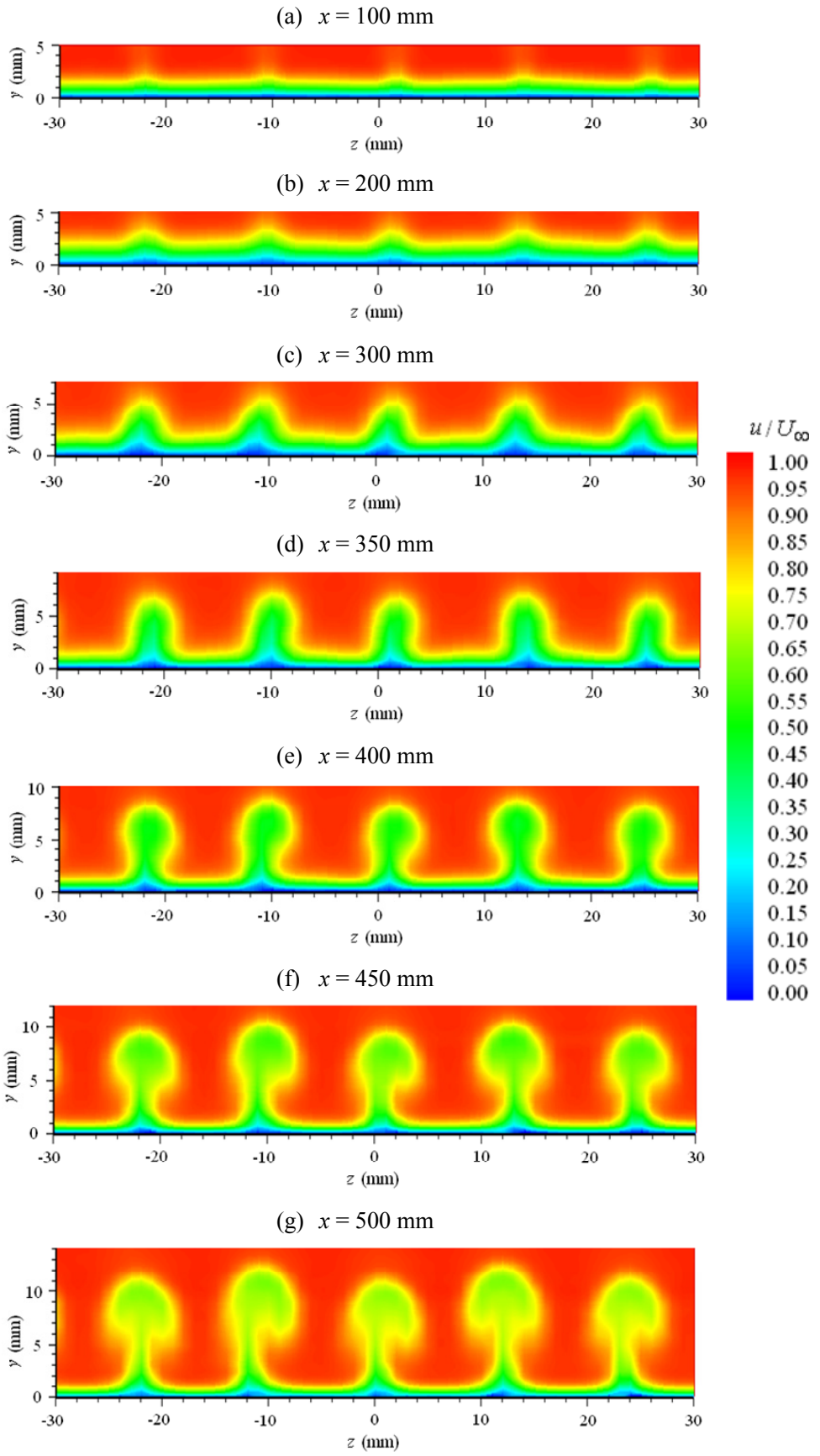

FIG. 4.1 Mean streamwise velocity (u/U_∞) contours on y-z plane for case 1 (λ_m = 12 mm and U_∞ = 2.8 m/s).

(h) x = 550 mm

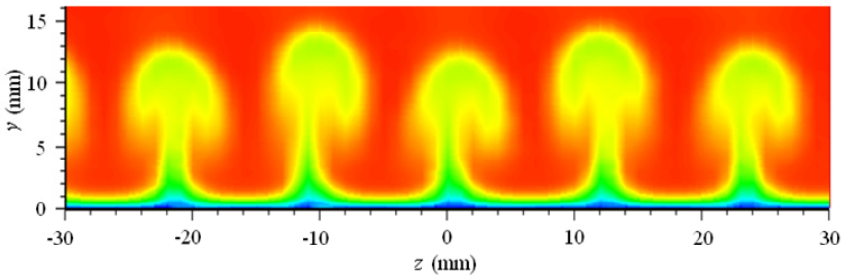

(i) x = 600 mm

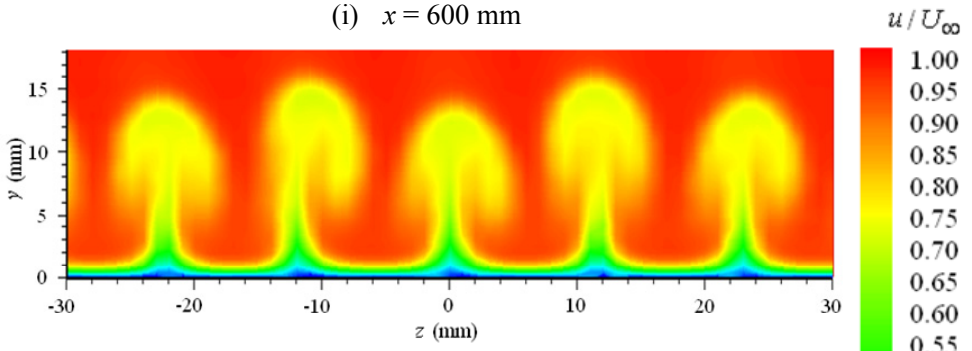

(j) x = 700 mm

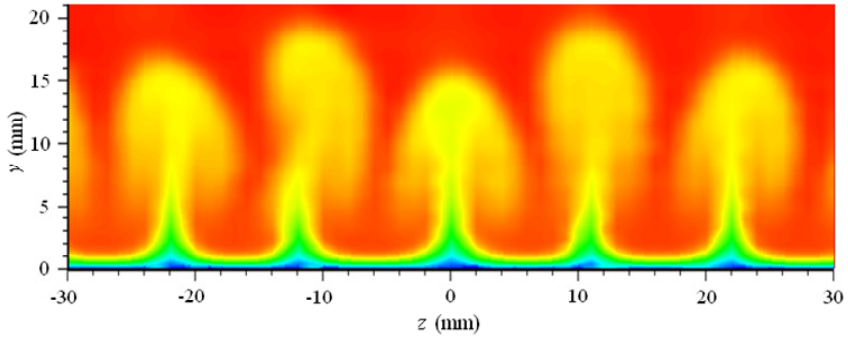

(k) x = 800 mm

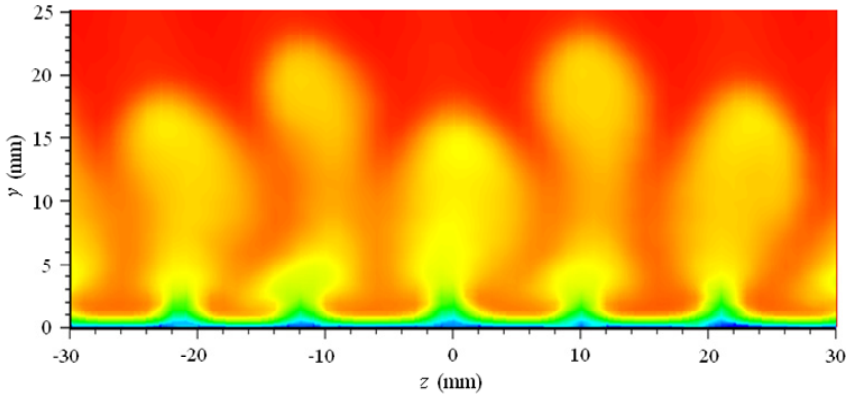

FIG. 4.1 Continued.

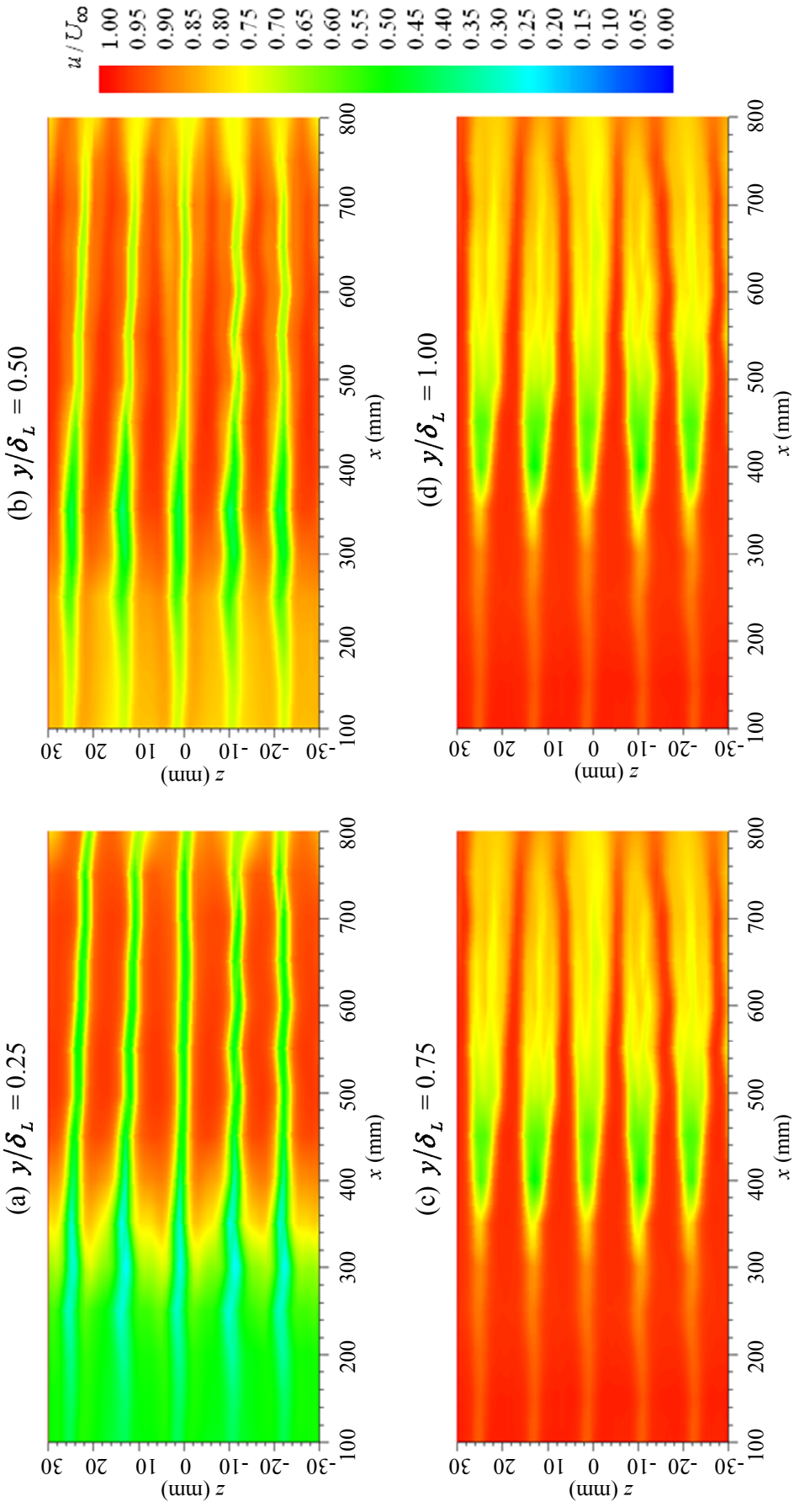

FIG. 4.2 Mean streamwise velocity (u/U_∞) contours on x-z plane for case 1 (λ_m = 12 mm and U_∞ = 2.8 m/s).

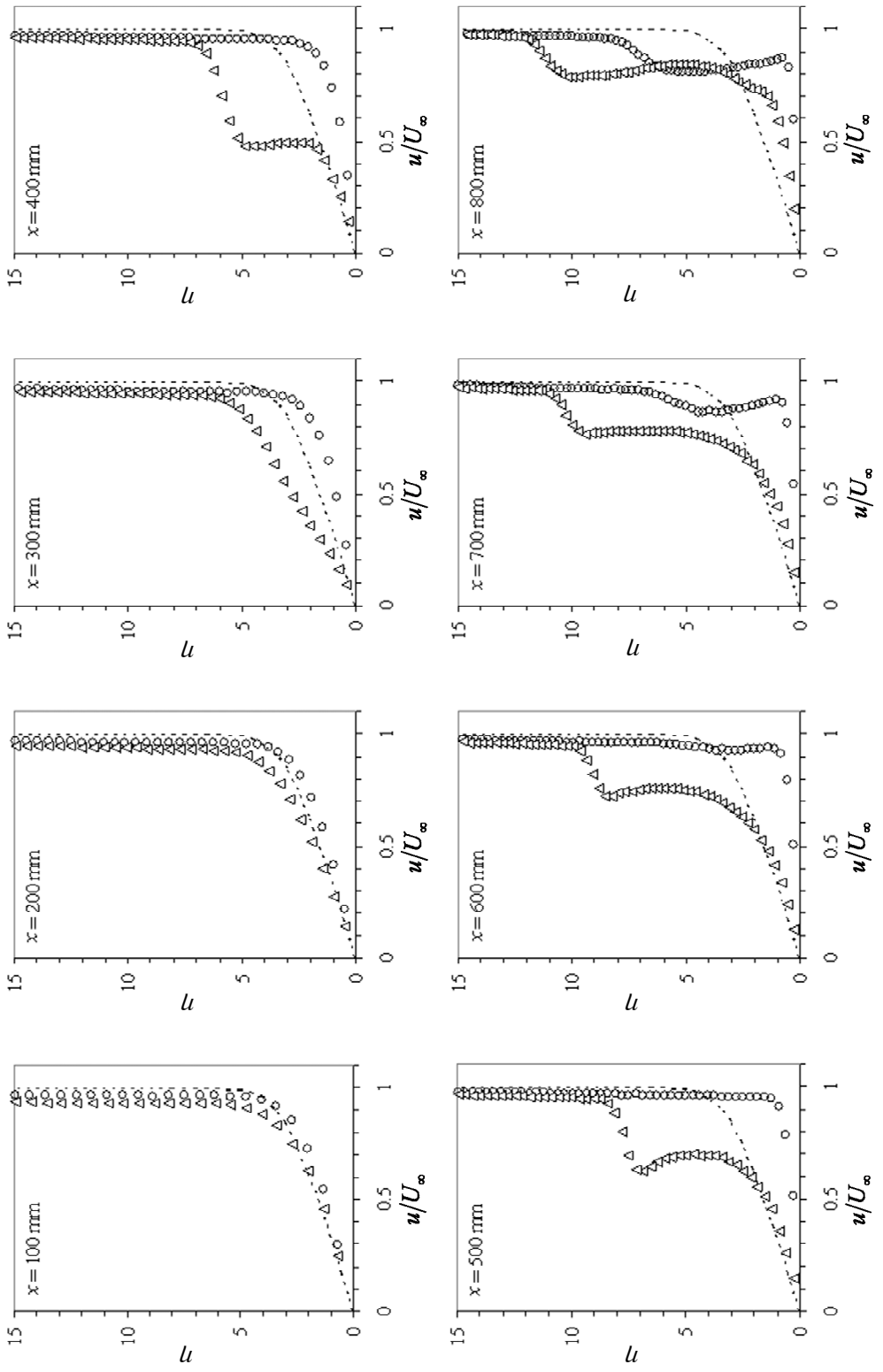

FIG. 4.3 Mean streamwise velocity (u/U_∞) profiles at the center of upwash (Δ) and downwash (O) for case 1 (λ_m = 12 mm and U_∞ = 2.8 m/s). ----- is Blasius solution for flat plate boundary layer velocity profile.

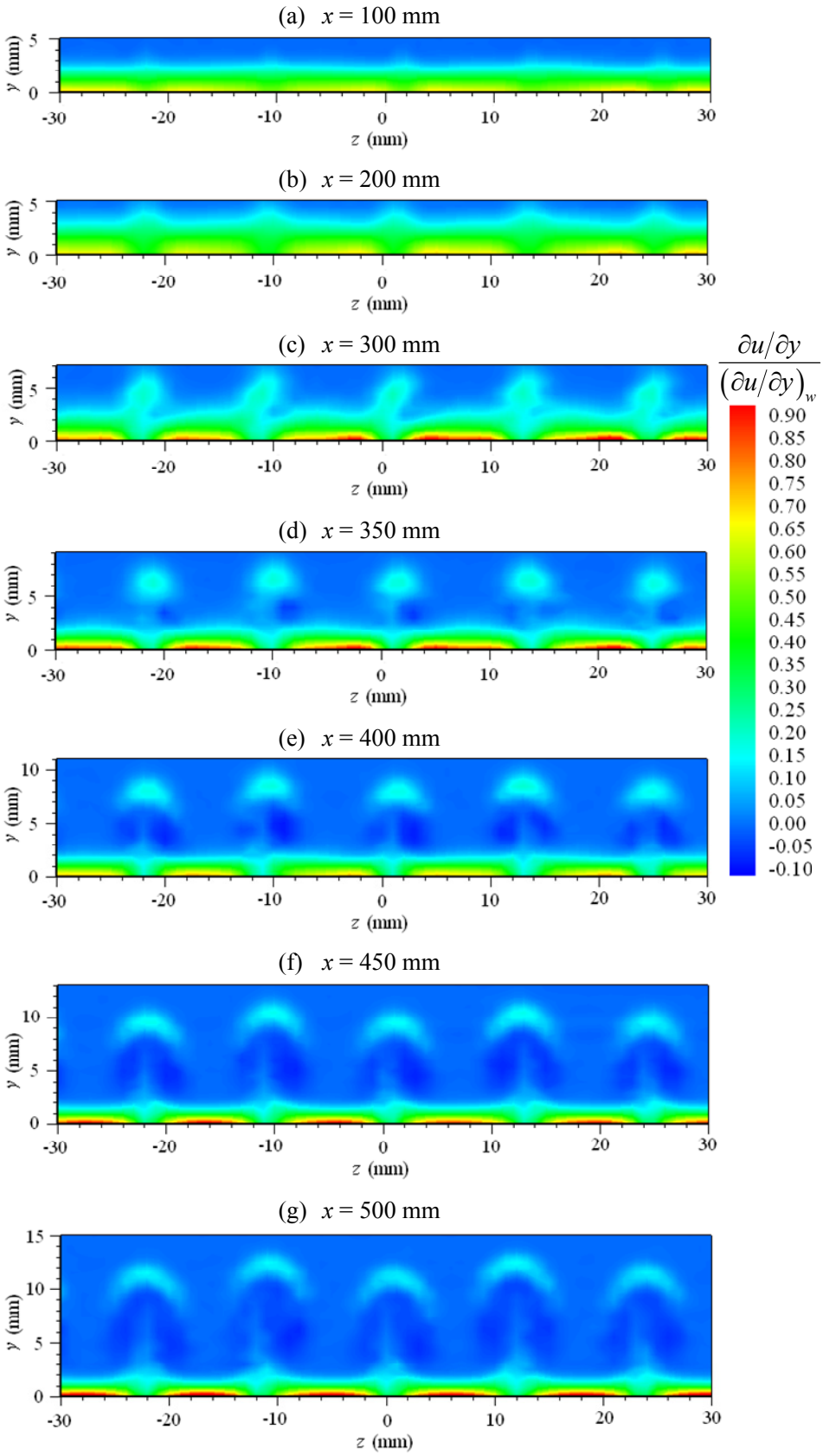

FIG. 4.4 Iso-shear ($\partial u/\partial y$) contours on y-z plane for case 1 (λ_m = 12 mm and U_∞ = 2.8 m/s).

(h) x = 550 mm

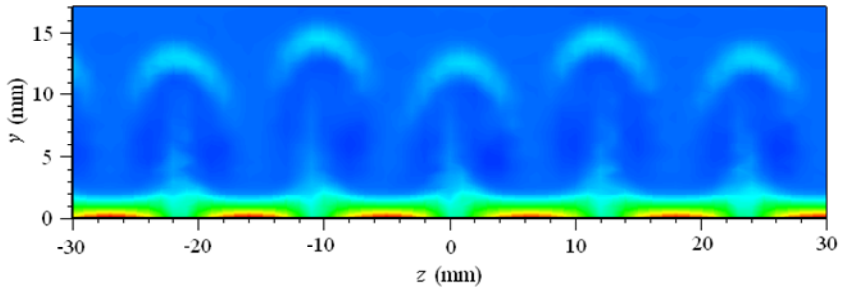

(i) x = 600 mm

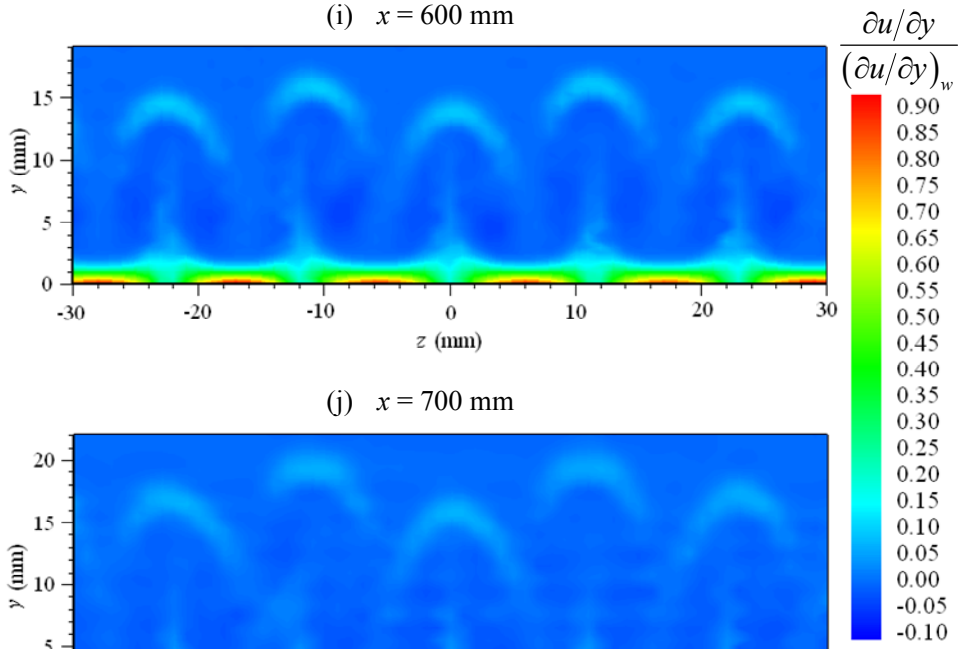

(j) x = 700 mm

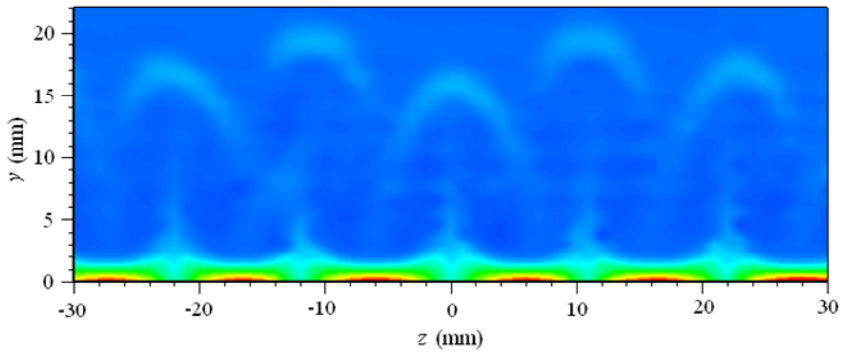

(k) x = 800 mm

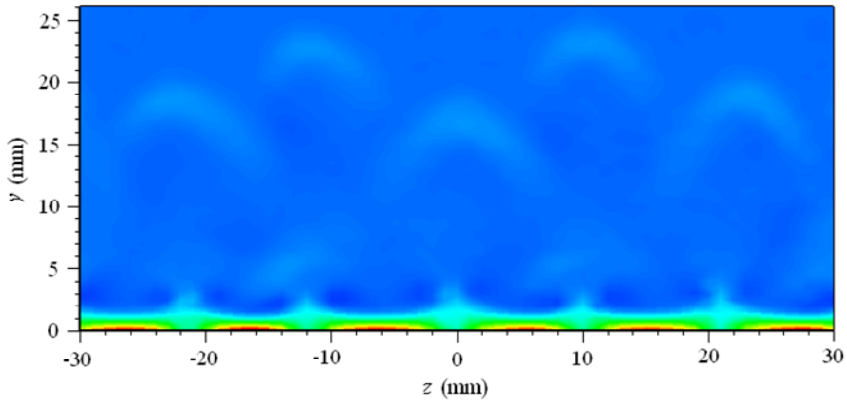

FIG. 4.4 Continued

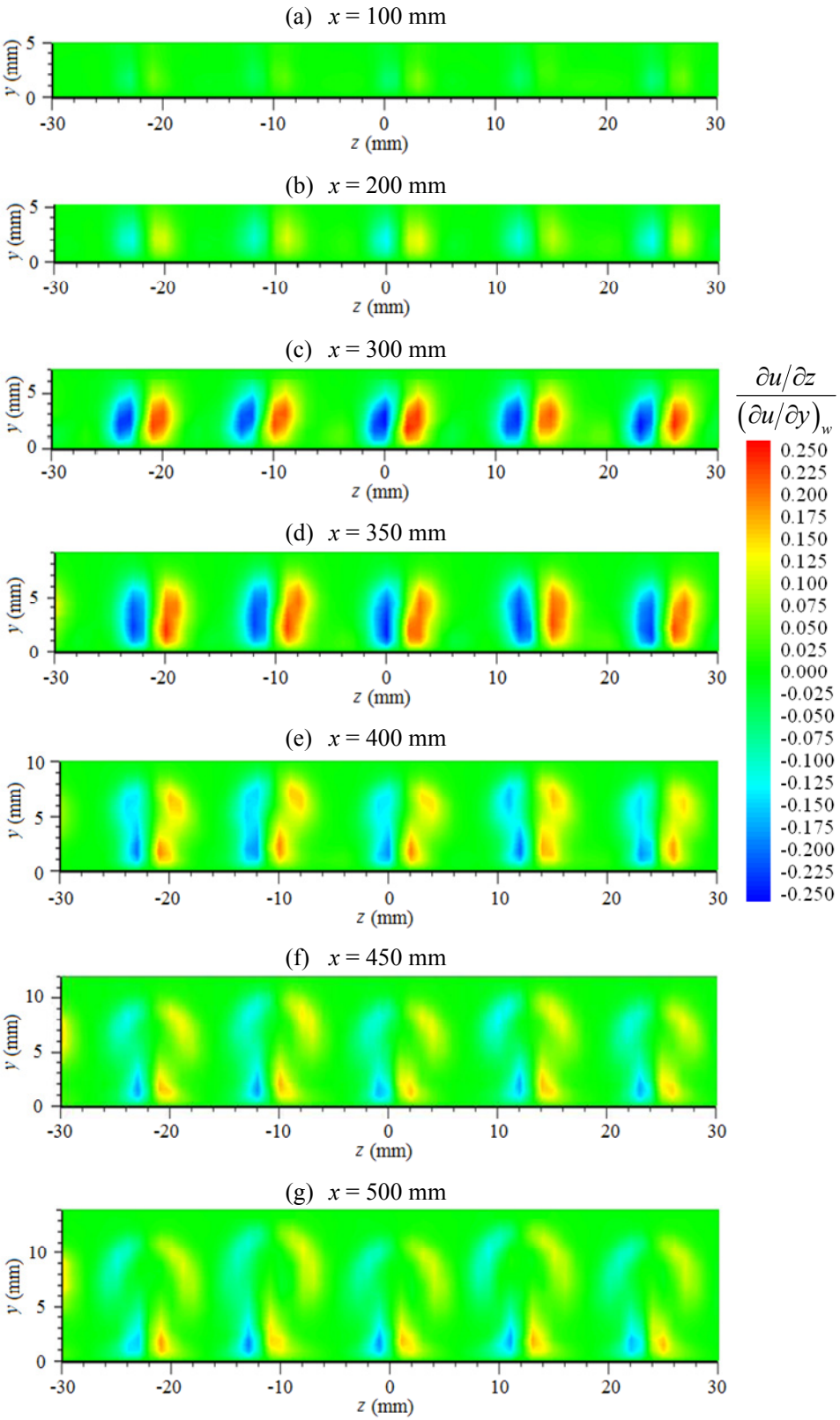

FIG. 4.5 Iso-shear ($\partial u/\partial z$) contours on *y*-*z* plane for case 1 (λ_m = 12 mm and U_∞ = 2.8 m/s).

(h) $x = 550$ mm

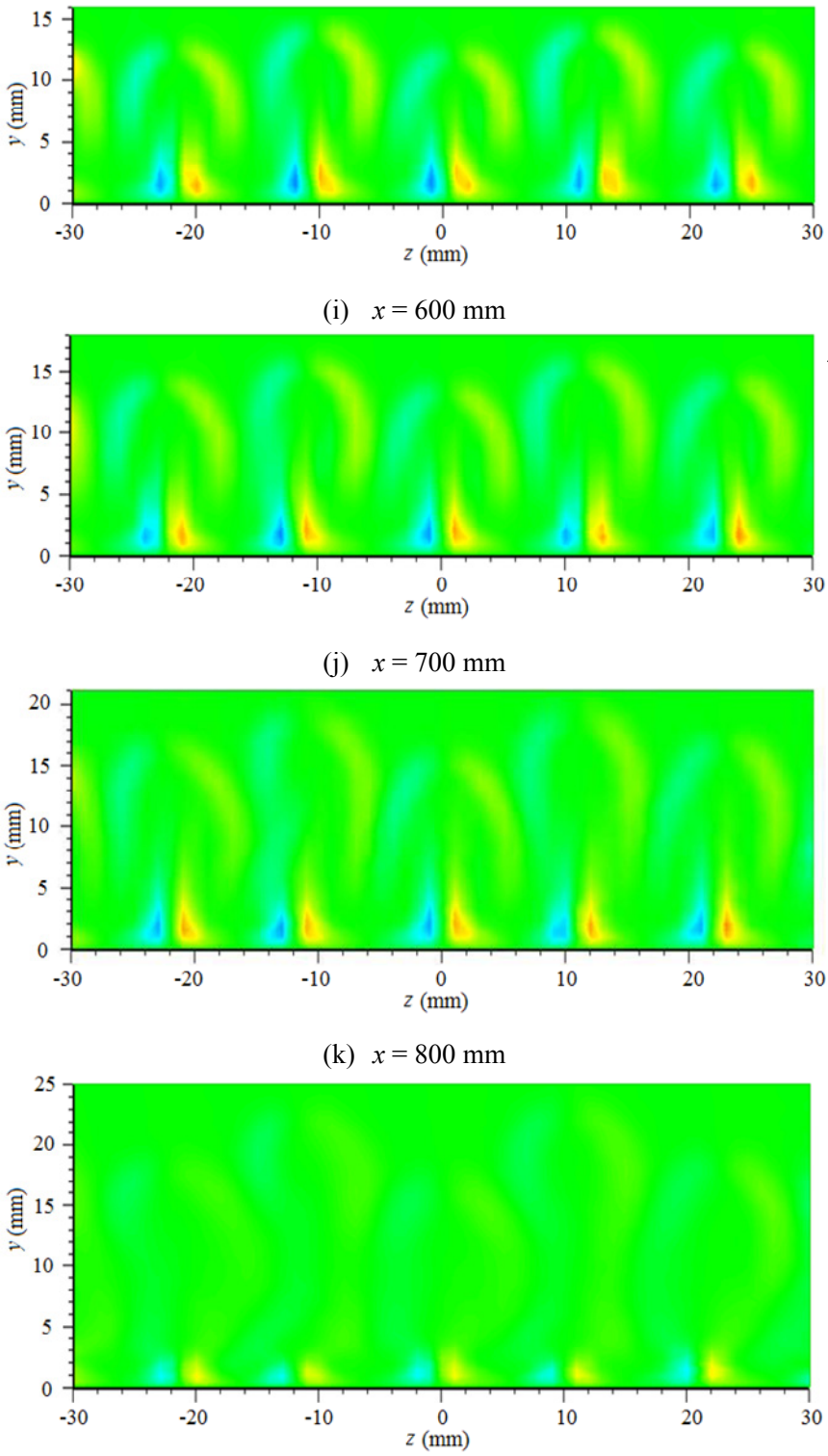

(i) $x = 600$ mm

(j) $x = 700$ mm

(k) $x = 800$ mm

FIG. 4.5 Continued.

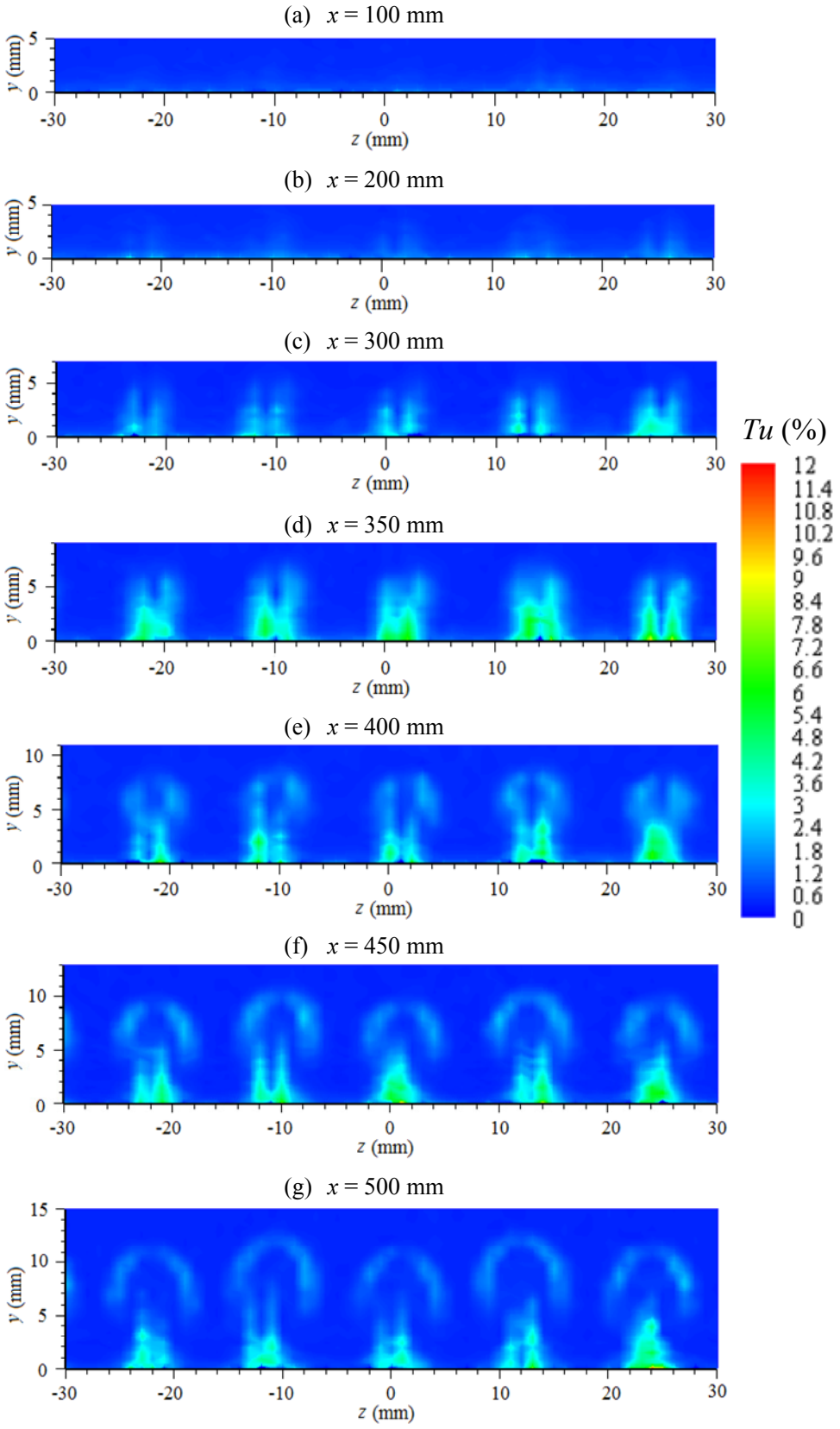

FIG. 4.6 Turbulence intensity (Tu) contours on y-z plane for case 1 (λ_m = 12 mm and U_∞ = 2.8 m/s).

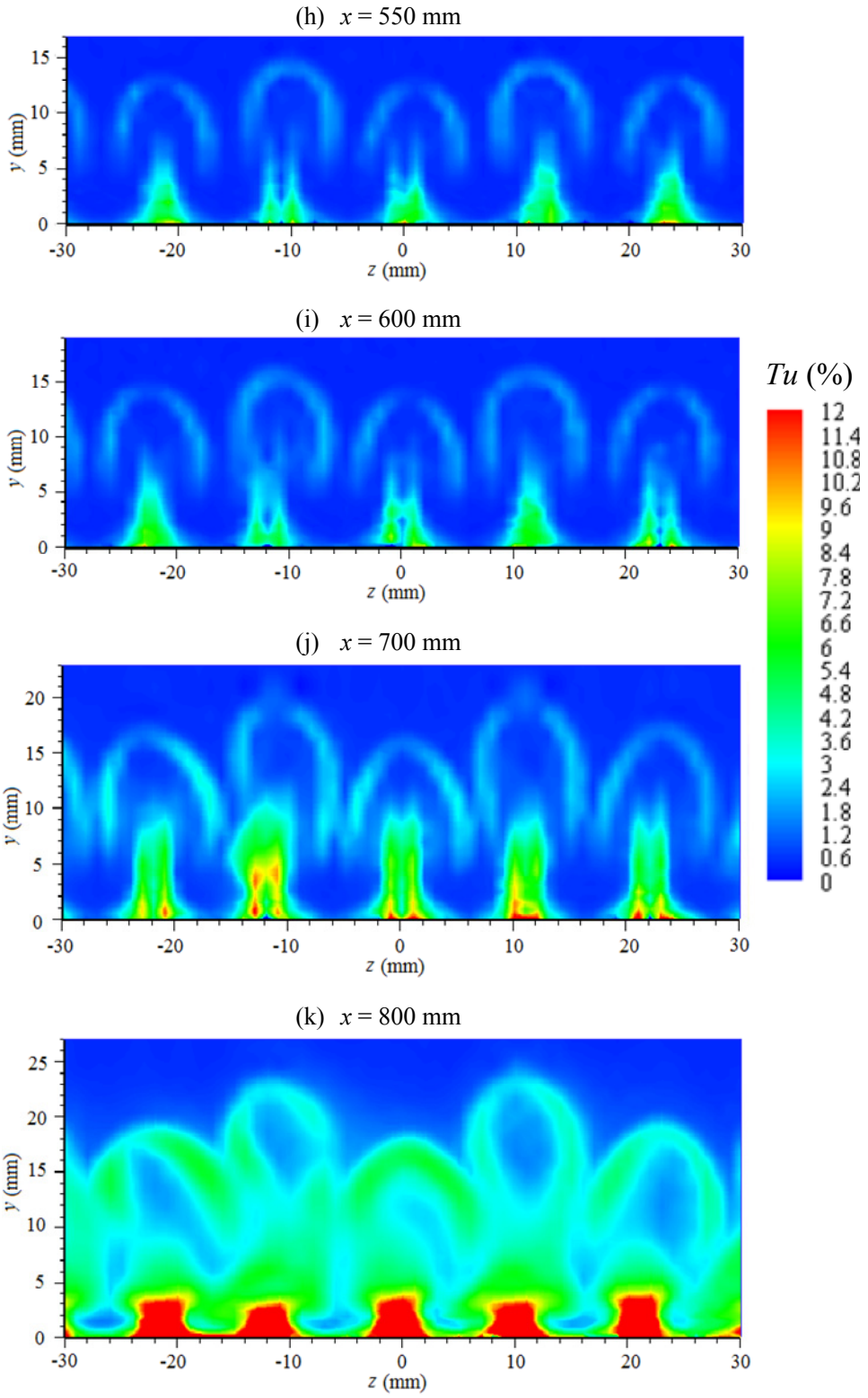

FIG. 4.6 Continued.

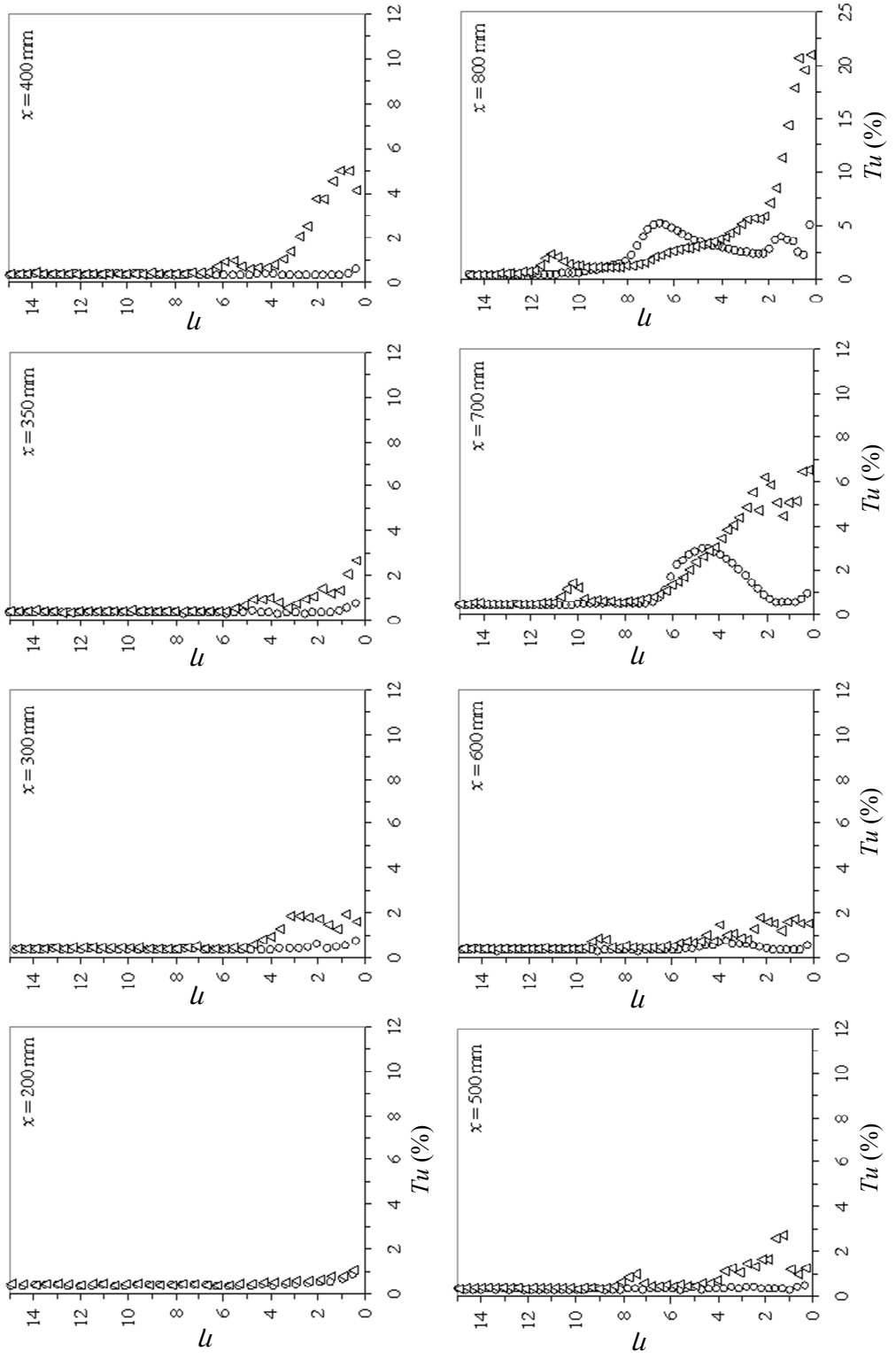

FIG. 4.7 Turbulence intensity (Tu) profiles at the center of upwash (Δ) and downwash (O) for case 1 (λ_m = 12 mm and U_∞ = 2.8 m/s).

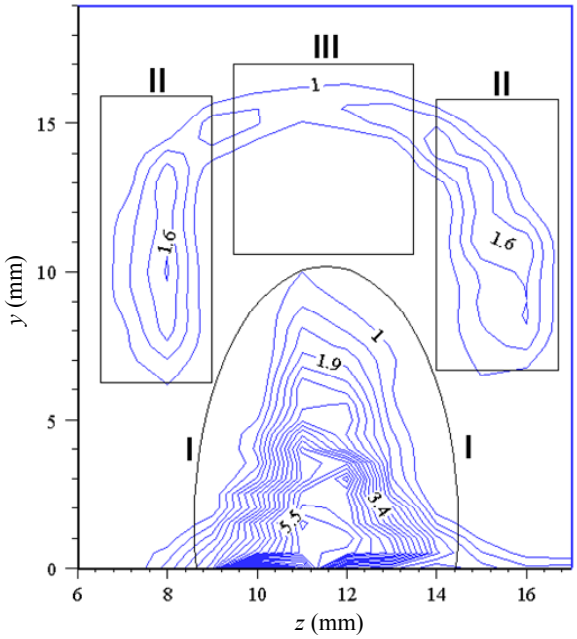

FIG. 4.8 Schematic of three regions representing the maxima of the intense turbulence intensity.

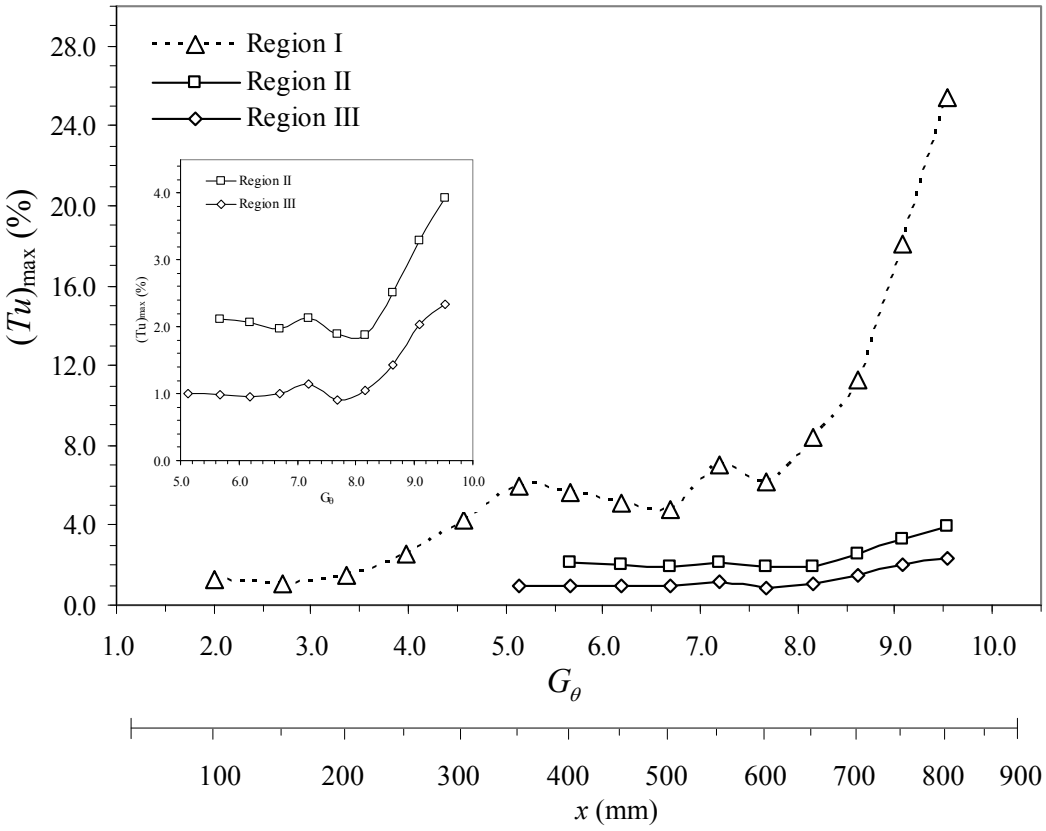

FIG. 4.9 Maxima of the intense turbulence versus G_θ at three defined regions (see Fig. 4.8) for case 1 (λ_m = 12 mm and U_∞ = 2.8 m/s).

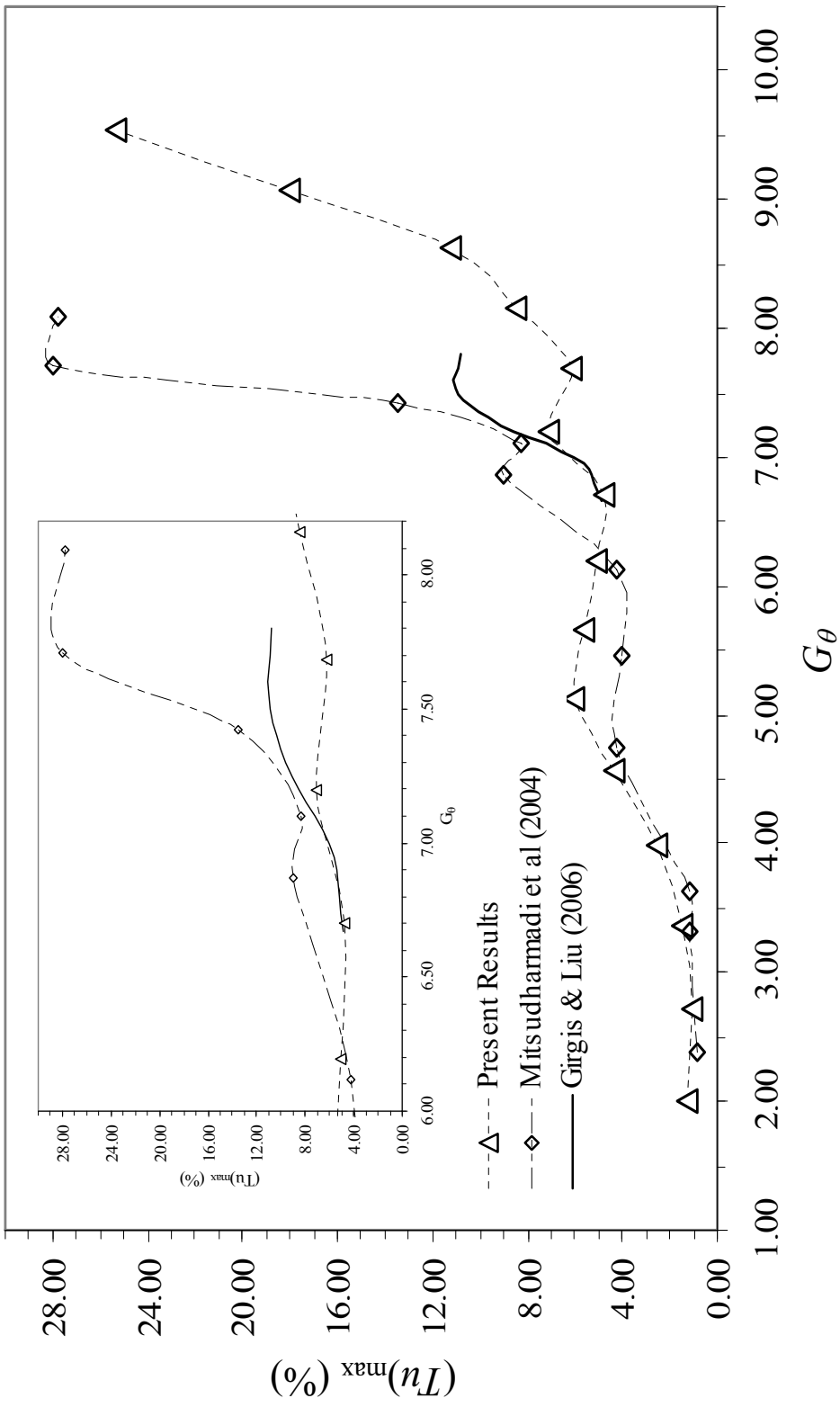

FIG. 4.10 Maximum turbulence intensity Tu_{max} versus G_θ for case 1 (λ_m = 12 mm and U_∞ = 2.8 m/s). The results of Mitsudharmadi *et al*. (2004) and Girgis and Liu (2006) are included for comparison.

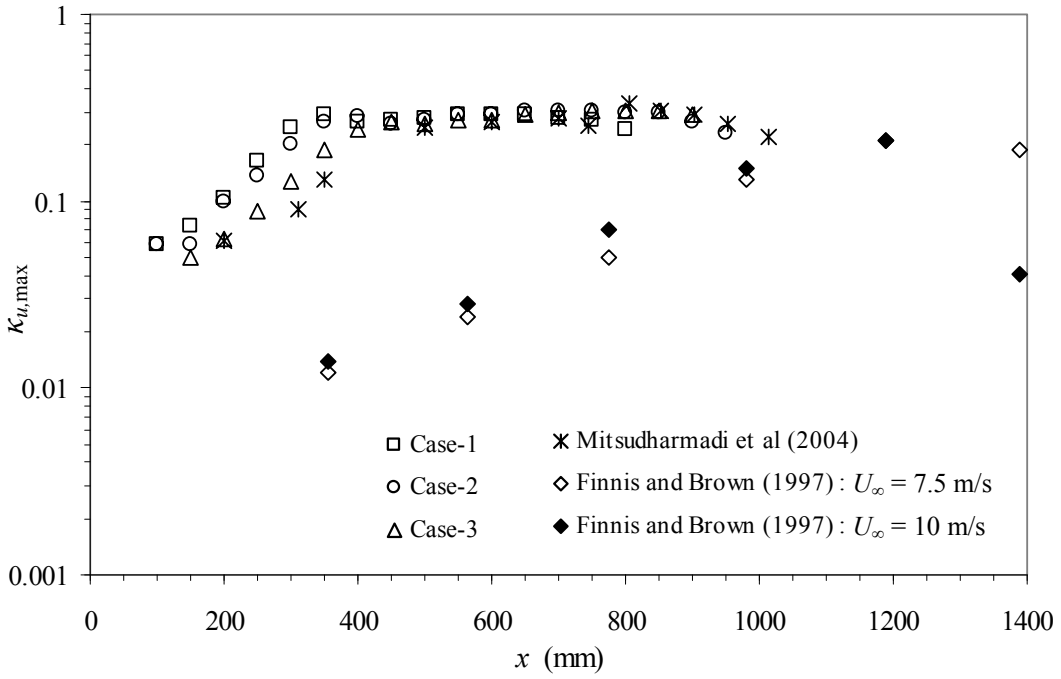

FIG. 4.11 Development of maximum disturbance amplitude $\kappa_{u,\max}$ for case 1: λ_m = 12 mm and U_∞ = 2.8 m/s, case 2: λ_m = 15 mm and U_∞ = 2.1 m/s, case 3: λ_m = 20 mm and U_∞ = 1.3 m/s. The results of Mitsudharmadi *et al.* (2004) and Finnis and Brown (1997) are included for comparison.

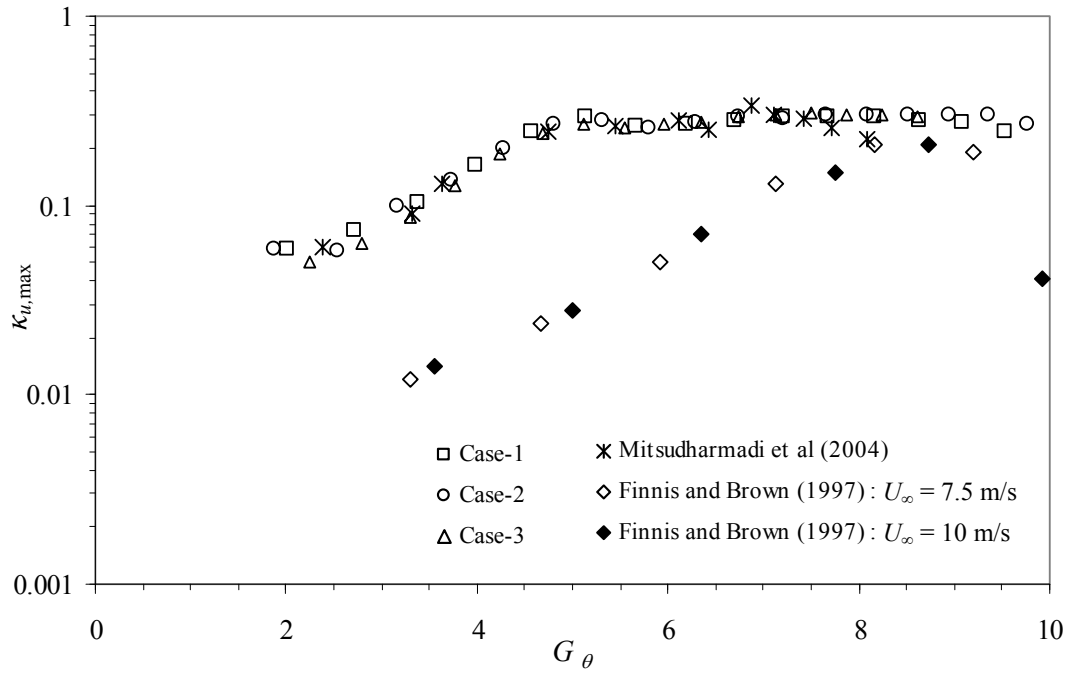

FIG. 4.12 Maximum disturbance amplitude $\kappa_{u,\max}$ versus G_θ for case 1: λ_m = 12 mm and U_∞ = 2.8 m/s, case 2: λ_m = 15 mm and U_∞ = 2.1 m/s, case 3: λ_m = 20 mm and U_∞ = 1.3 m/s. The results of Mitsudharmadi *et al.* (2004) and Finnis and Brown (1997) are included for comparison.

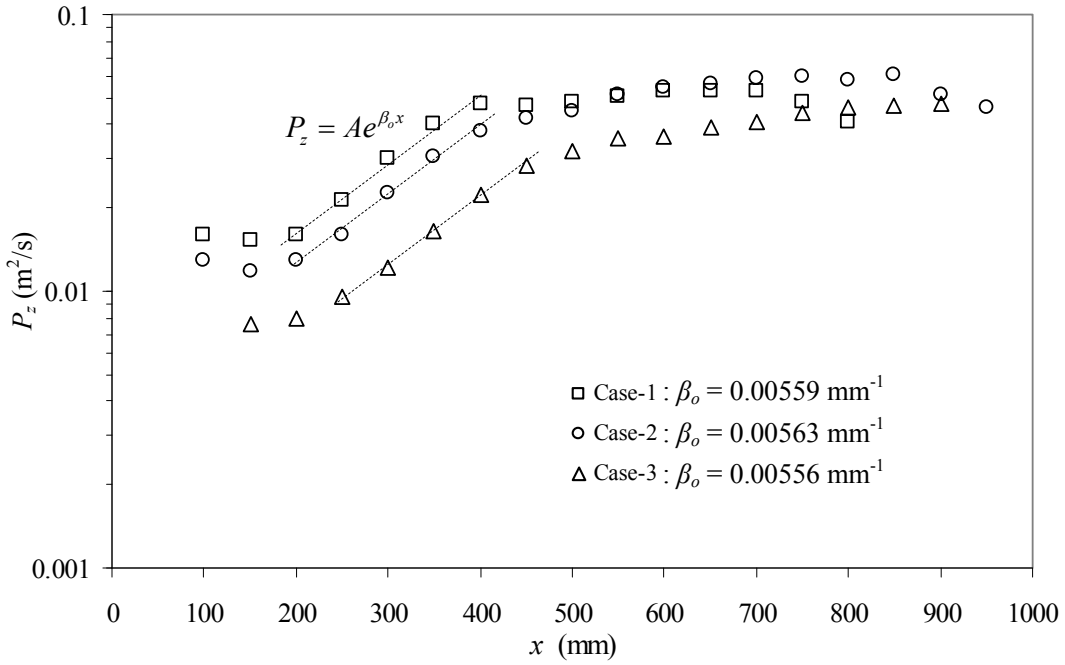

FIG. 4.13 Spatial amplification of perturbations P_z for case 1: λ_m = 12 mm and U_∞ = 2.8 m/s, case 2: λ_m = 15 mm and U_∞ = 2.1 m/s, case 3: λ_m = 20 mm and U_∞ = 1.3 m/s.

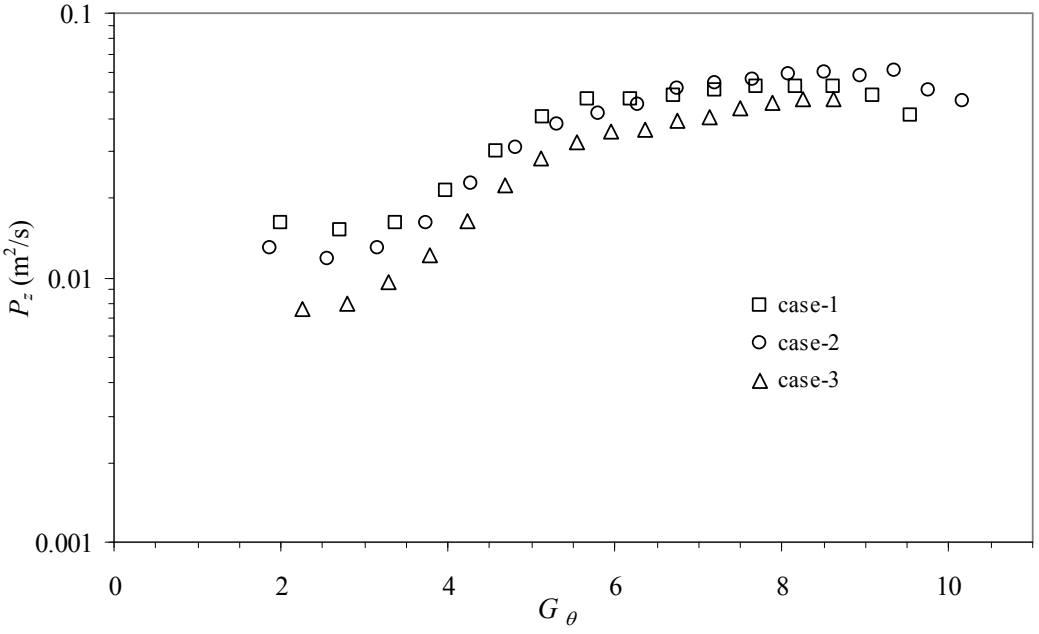

FIG. 4.14 Spatial amplification of perturbations P_z versus G_θ for case 1: λ_m = 12 mm and U_∞ = 2.8 m/s, case 2: λ_m = 15 mm and U_∞ = 2.1 m/s, case 3: λ_m = 20 mm and U_∞ = 1.3 m/s.

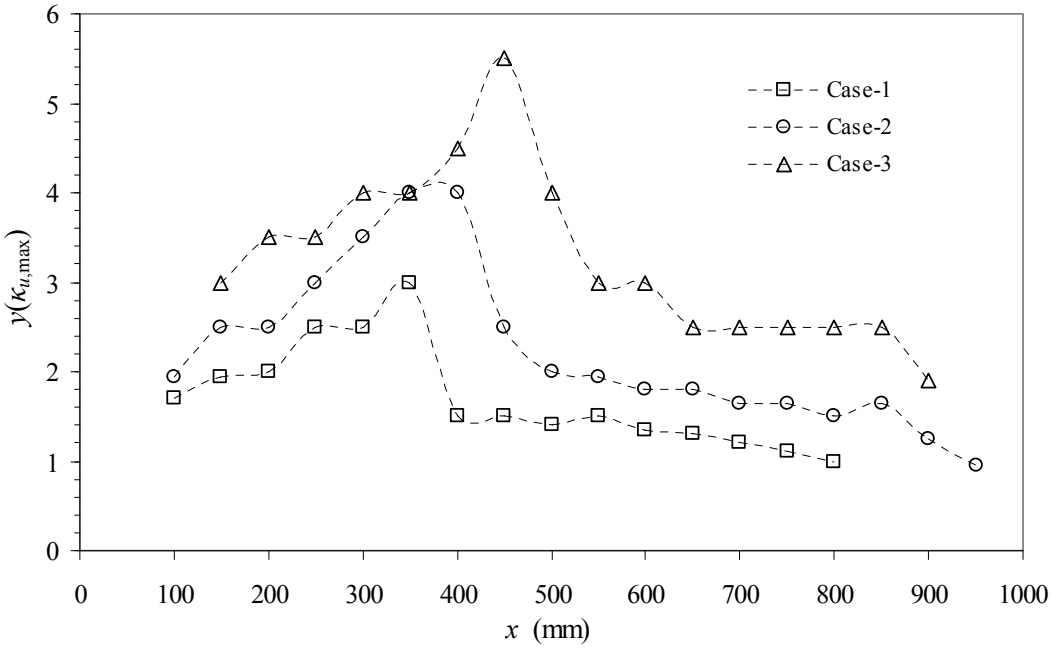

FIG. 4.15 The normal position of the maximum disturbance amplitude $y(\kappa_{u,\max})$ for case 1: λ_m = 12 mm and U_∞ = 2.8 m/s, case 2: λ_m = 15 mm and U_∞ = 2.1 m/s, case 3: λ_m = 20 mm and U_∞ = 1.3 m/s.

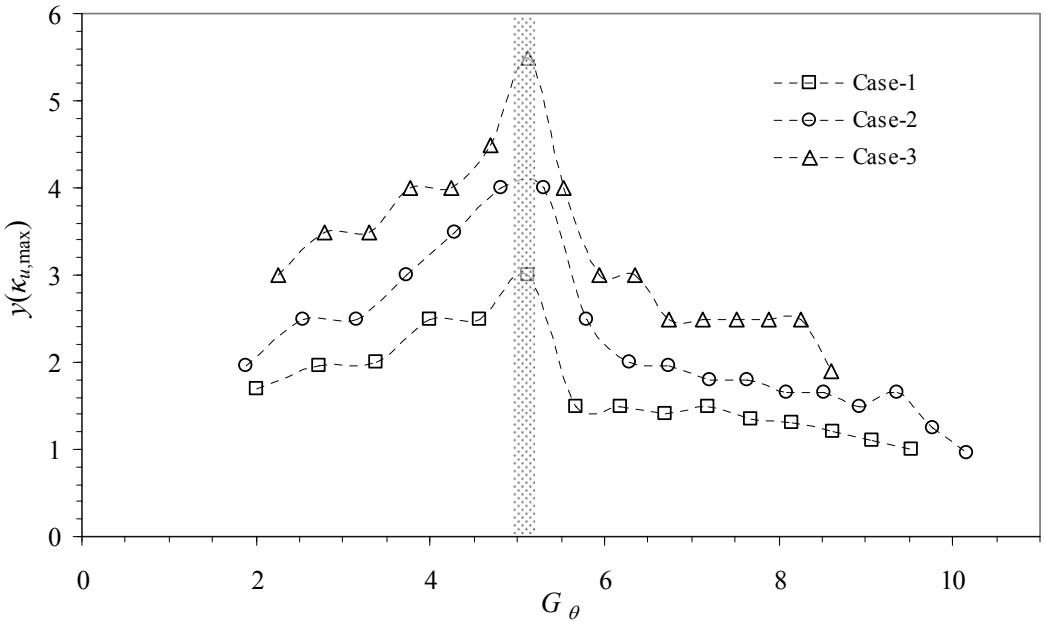

FIG. 4.16 The normal position of the maximum disturbance amplitude $y(\kappa_{u,\max})$ versus G_θ for case 1: λ_m = 12 mm and U_∞ = 2.8 m/s, case 2: λ_m = 15 mm and U_∞ = 2.1 m/s, case 3: λ_m = 20 mm and U_∞ = 1.3 m/s.

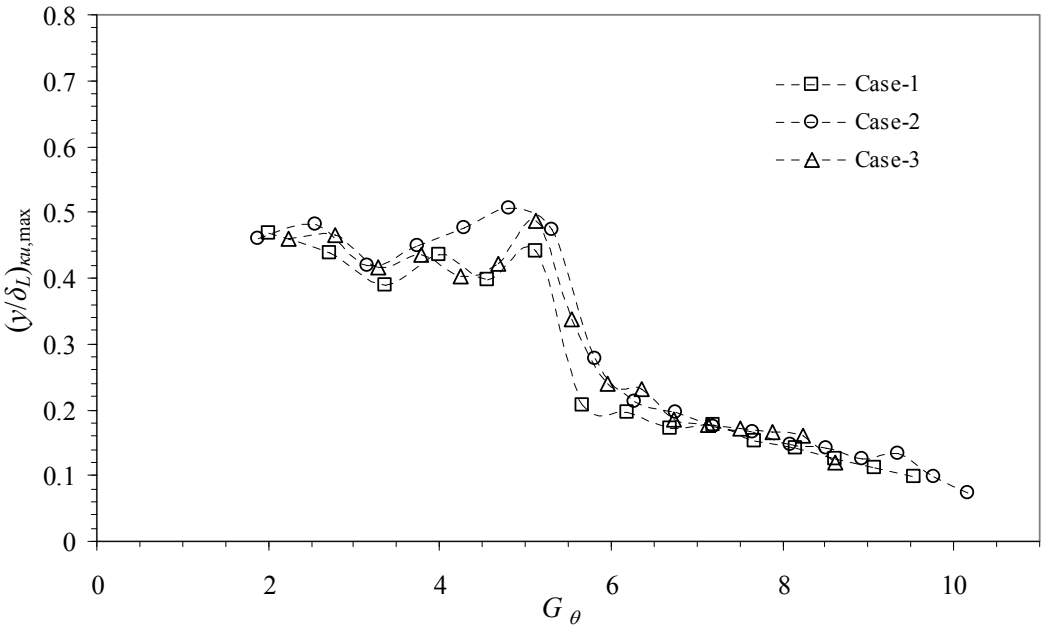

FIG. 4.17 The normal position of the maximum disturbance amplitude normalized with Blasius boundary layer thickness for laminar flow $\left(y/\delta_L\right)_{\kappa_{u,\max}}$ versus G_θ for case 1: λ_m = 12 mm and U_∞ = 2.8 m/s, case 2: λ_m = 15 mm and U_∞ = 2.1 m/s, case 3: λ_m = 20 mm and U_∞ = 1.3 m/s.

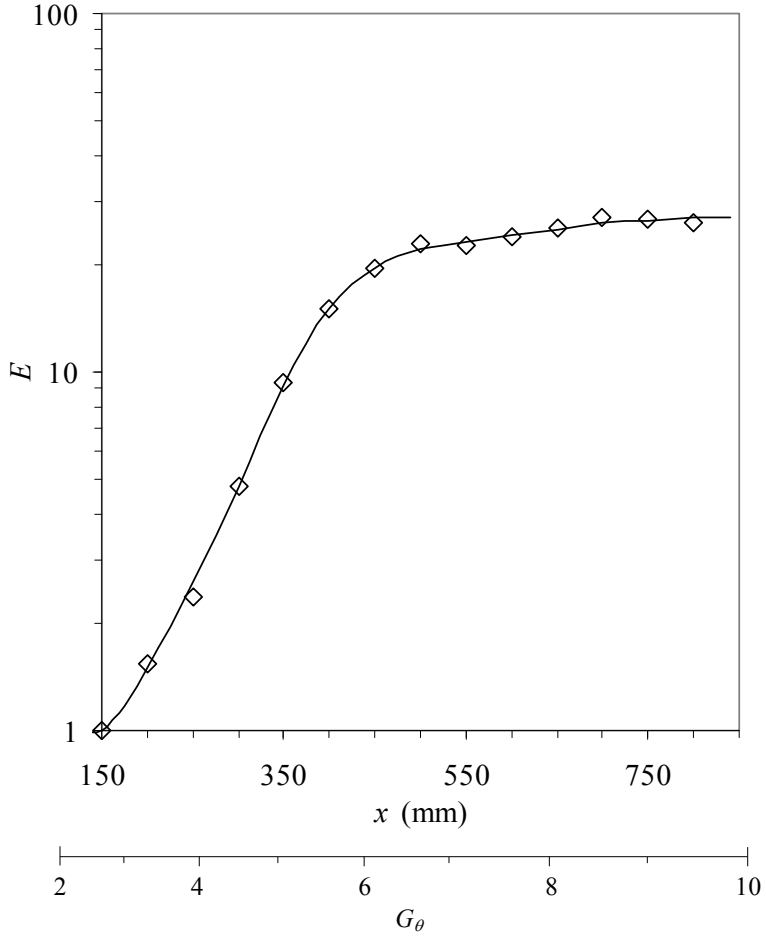

FIG. 5.1 Development of the relative perturbation energy $E = e/e_0$ showing the leveling off of the perturbation energy in the nonlinear region.

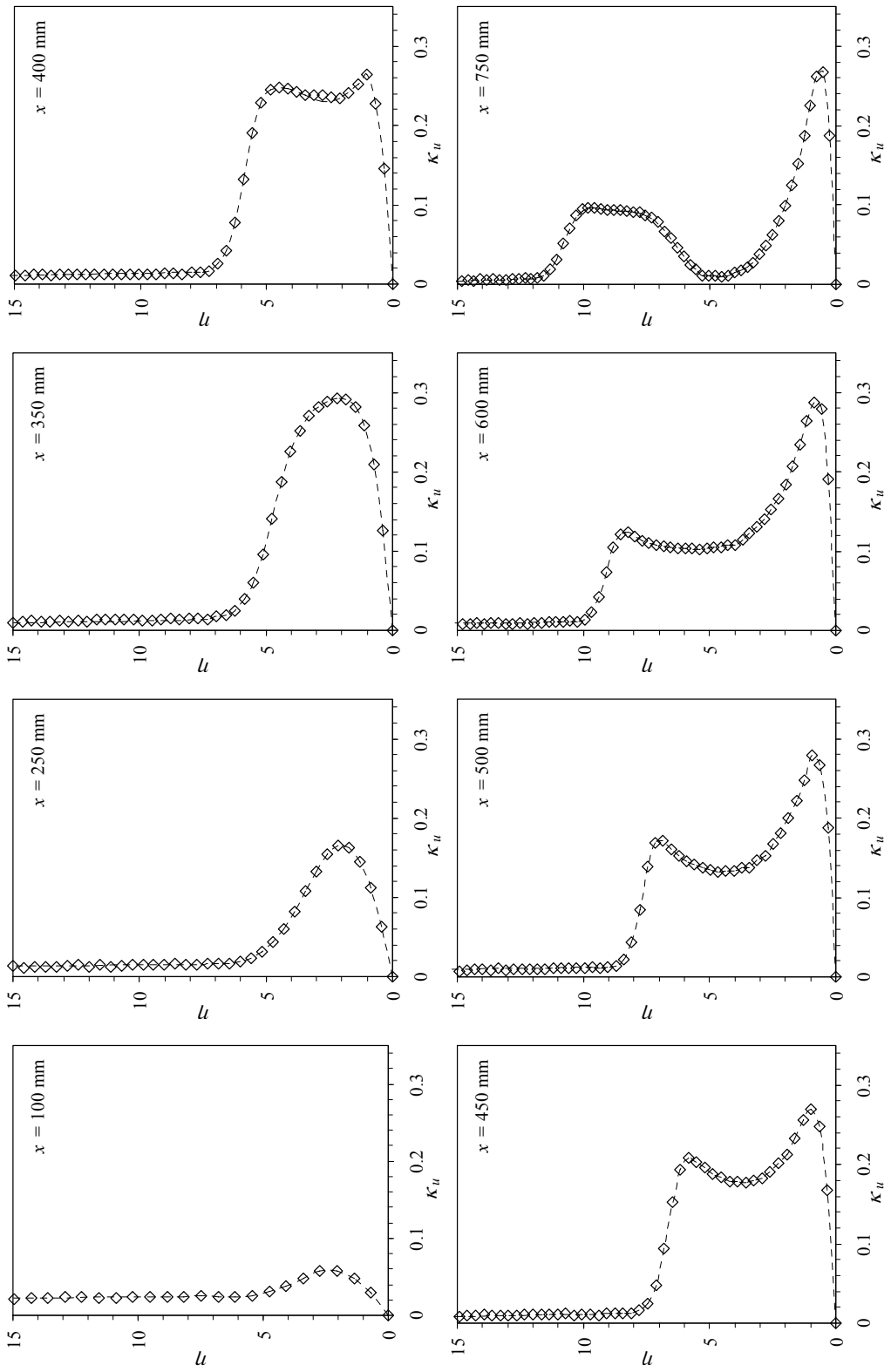

FIG. 5.2 Normal distributions of disturbance amplitude κ_u at several streamwise (x) locations.

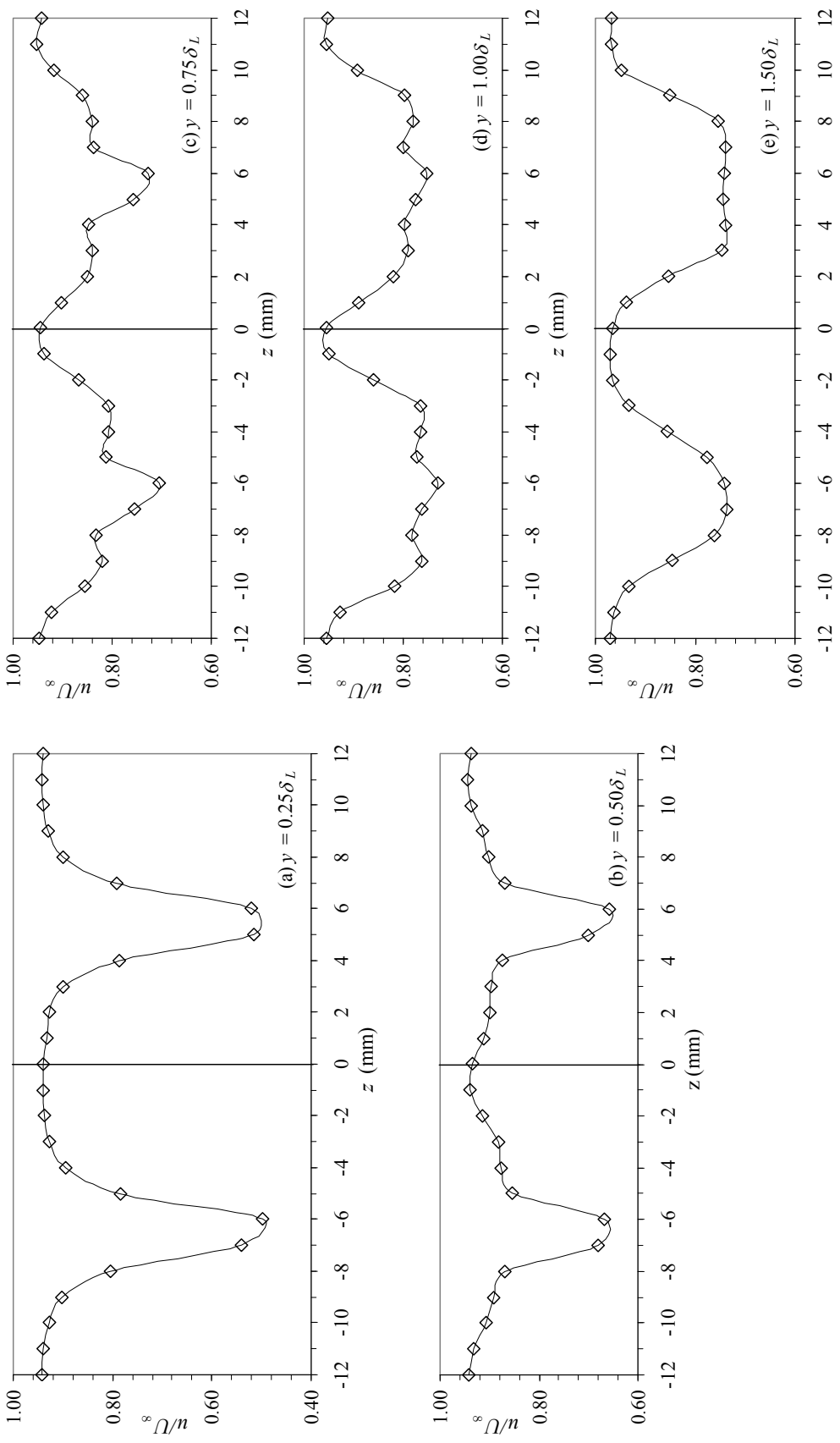

FIG. 5.3 Typical spanwise distributions of streamwise velocity u/U_∞ in nonlinear region (x = 600 mm) at several normal (y) locations.

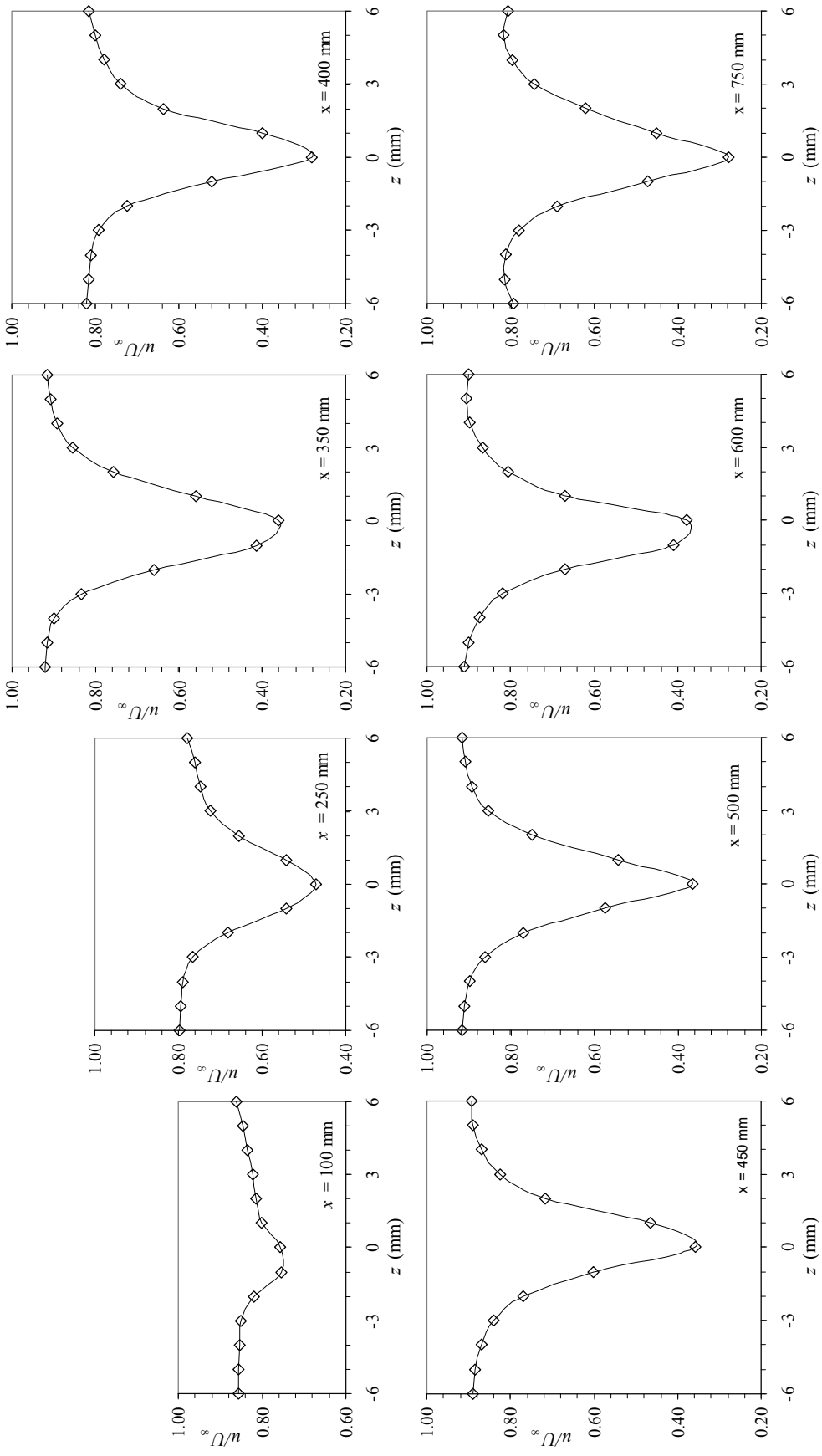

FIG. 5.4 Spanwise distributions of streamwise velocity u/U_∞ at the normal (y) location correspond to the first peak of the disturbance amplitude κ_u profile (see Fig. 5.2).

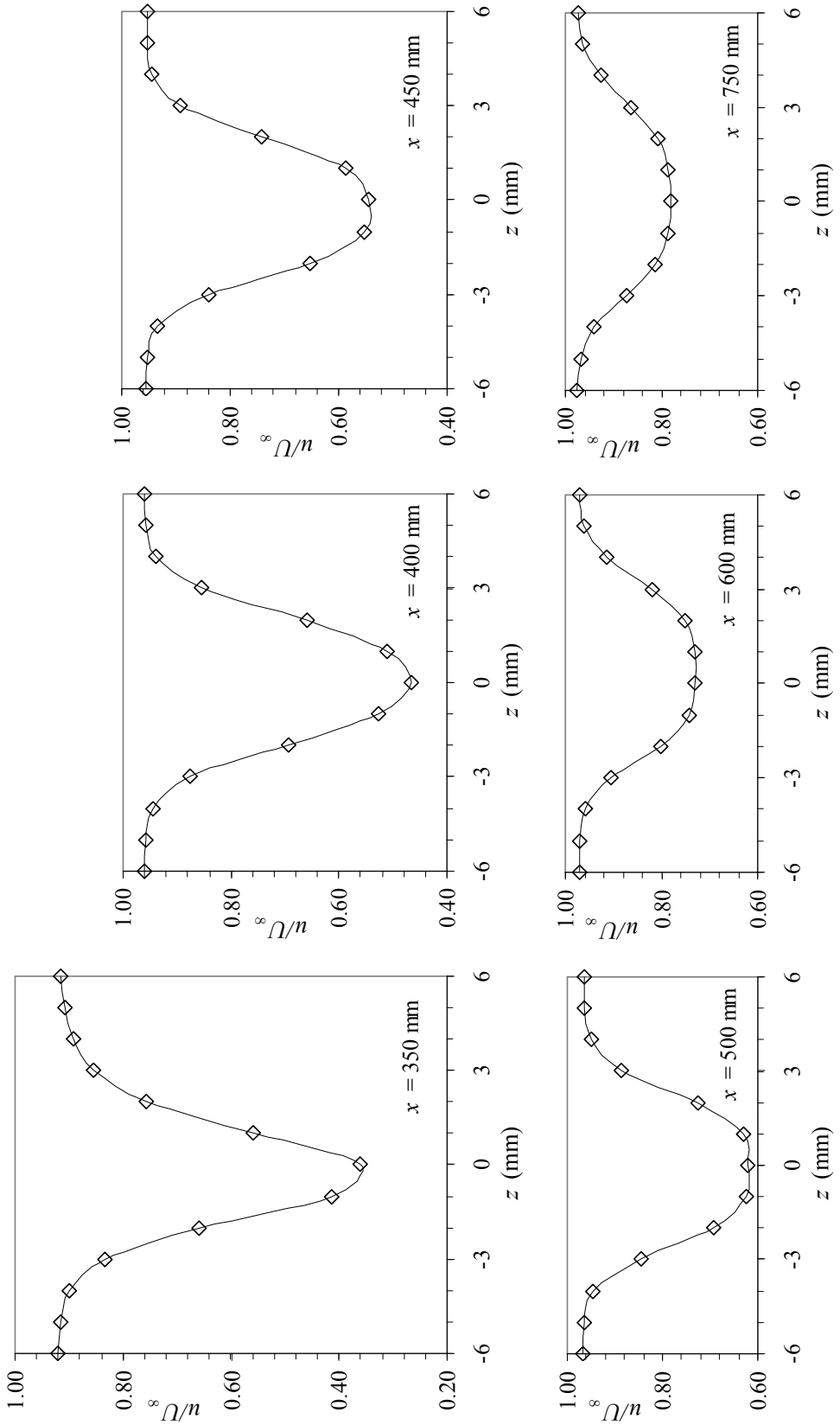

FIG. 5.5 Spanwise distributions of streamwise velocity u/U_∞ at the normal (y) location correspond to the second peak of the disturbance amplitude κ_u profile (see Fig. 5.2).

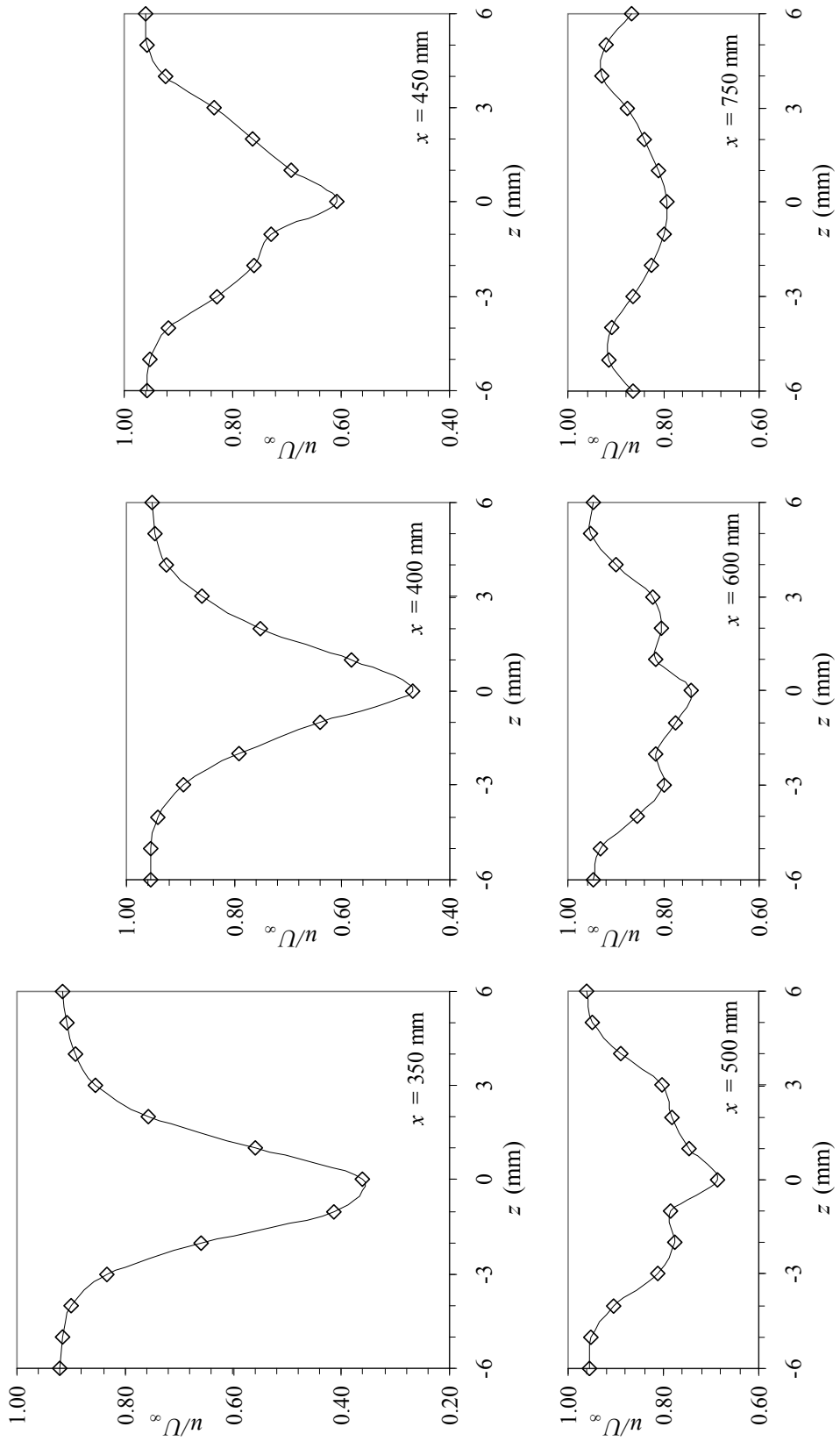

FIG. 5.6 Spanwise distributions of streamwise velocity u/U_∞ at the normal (y) location between the first and the second peaks of the disturbance amplitude κ_u profile (see Fig. 5.2).

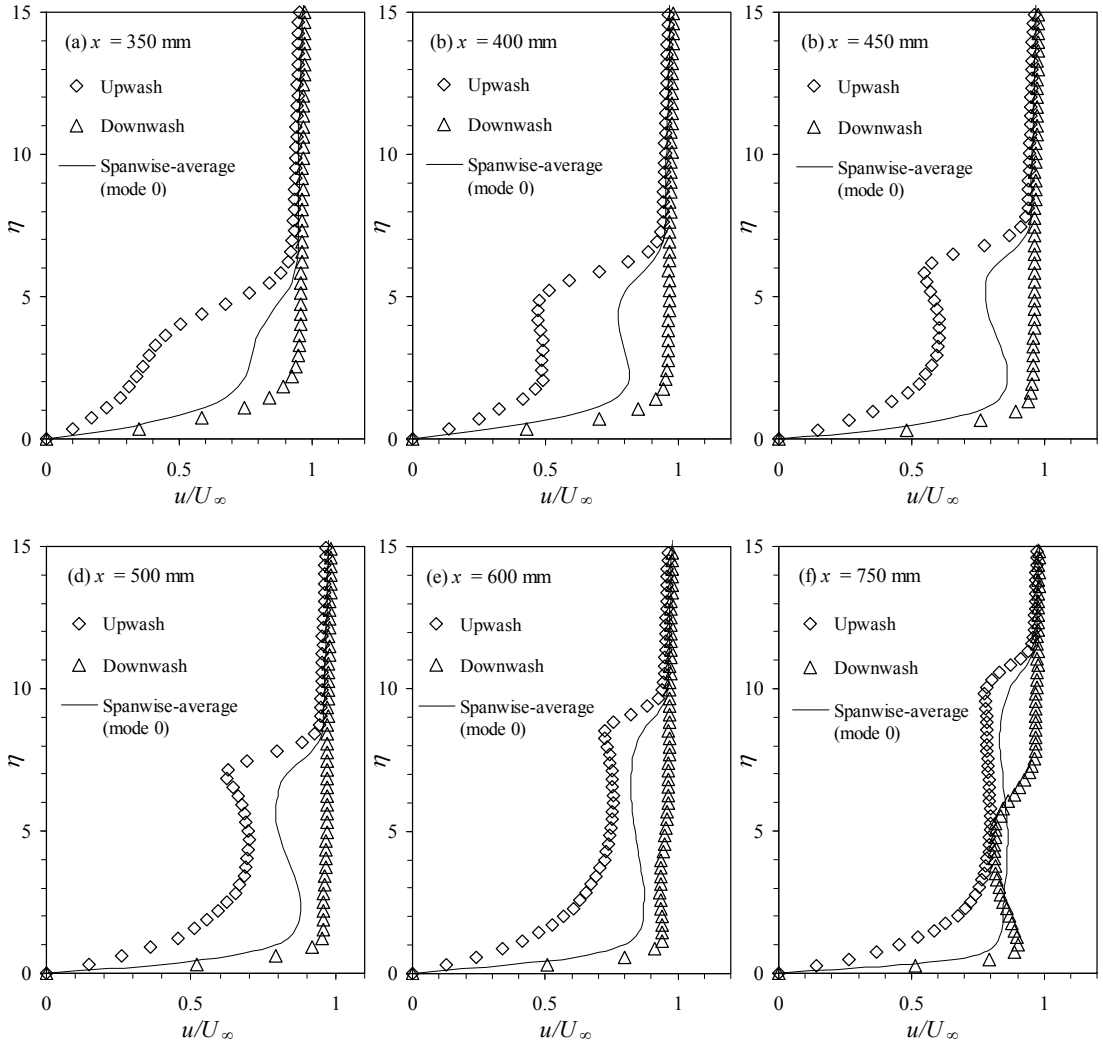

FIG. 5.7 Normal distributions of spanwise-average velocity ($\tilde{u}_0/U_\infty$) profile (mode 0) at several streamwise (x) locations. The corresponding velocity profiles at upwash and downwash are included for comparison.

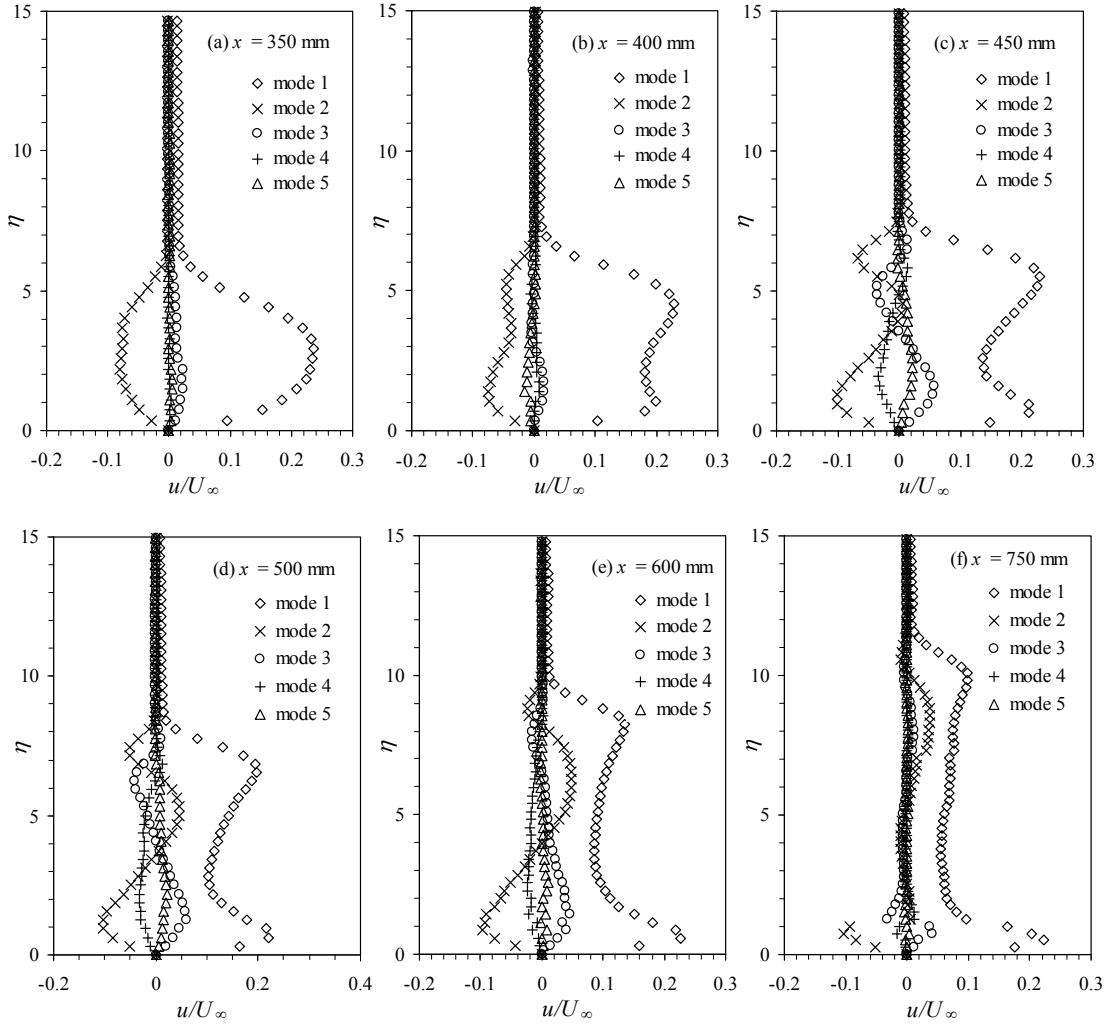

FIG. 5.8 Normal distributions of the amplitude of spanwise harmonic modes at several streamwise (x) locations.

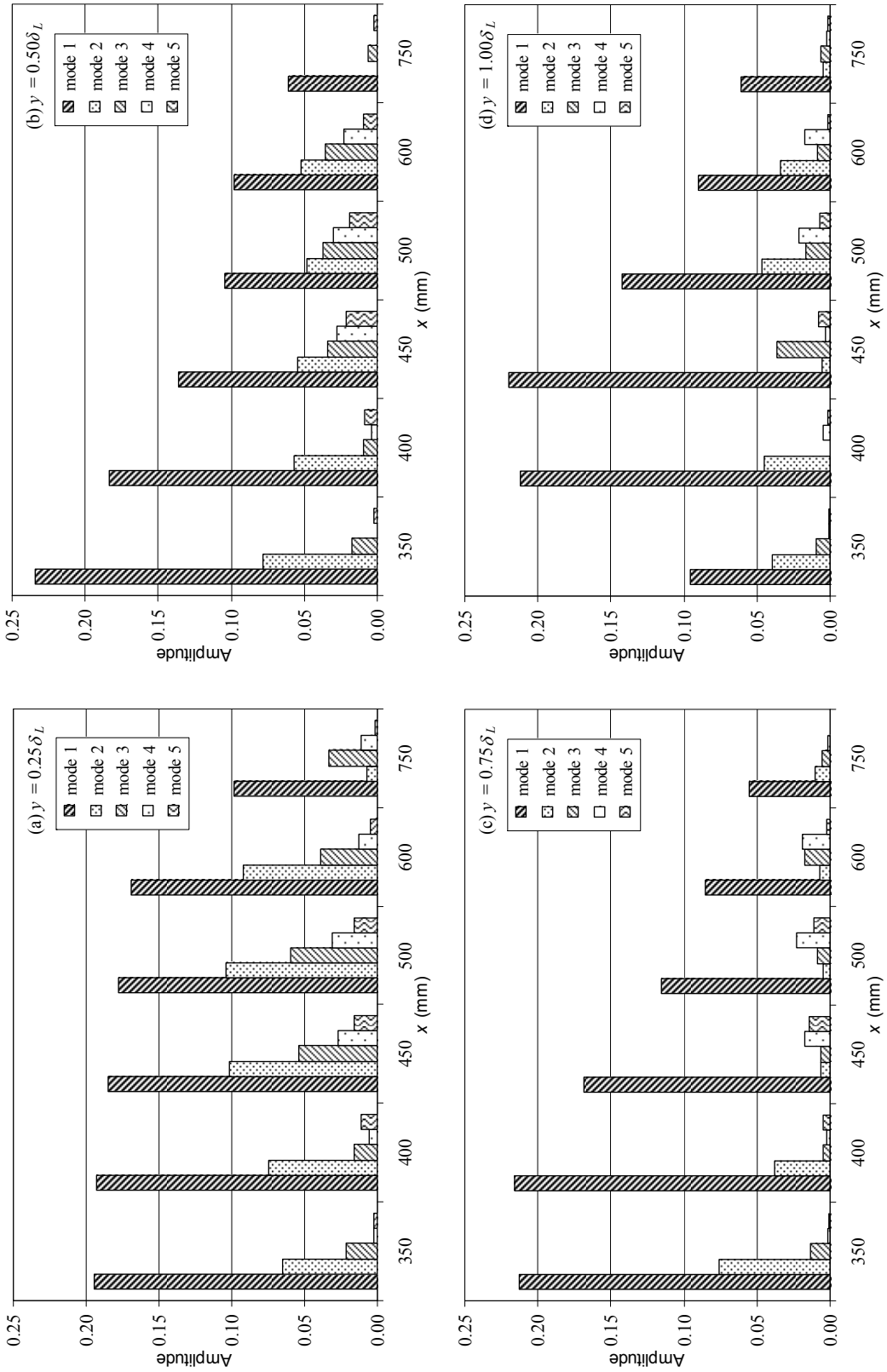

FIG. 5.9 Development of the power spectra of spanwise harmonic modes at several normal (y) locations.

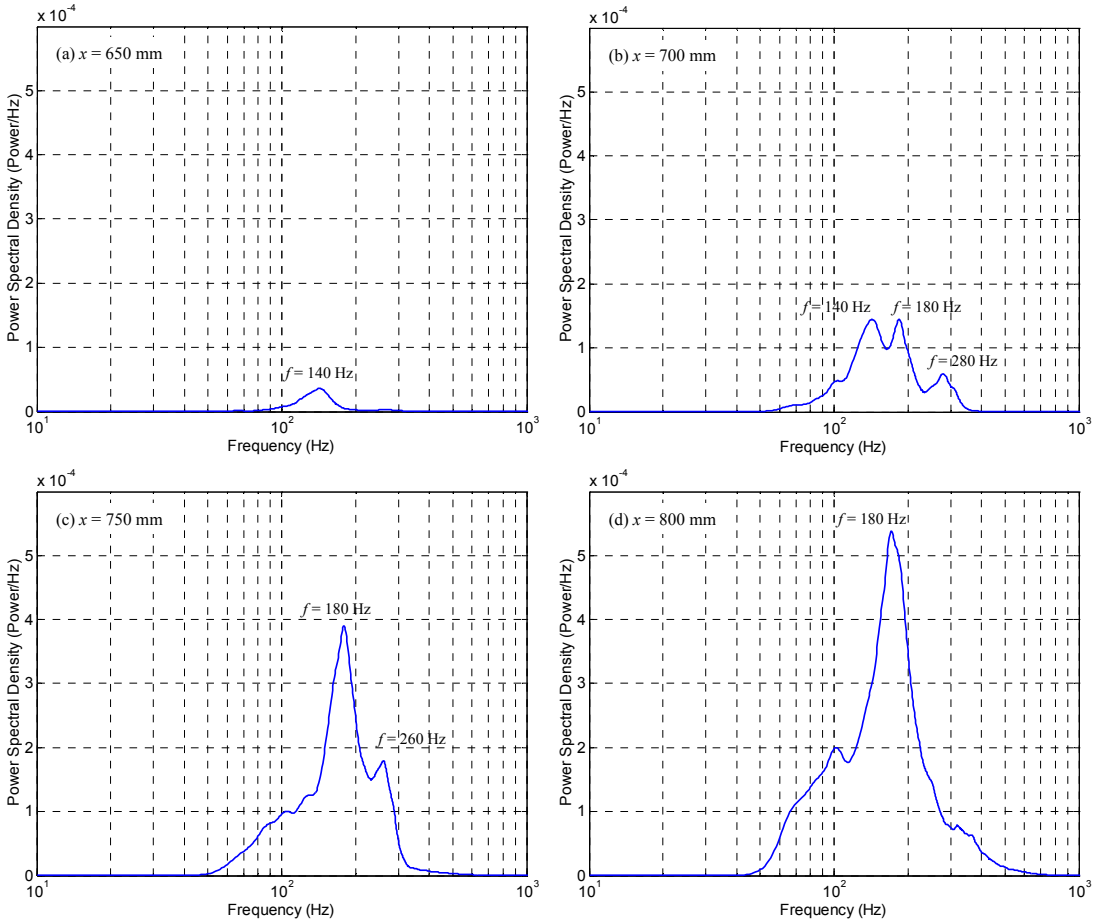

FIG. 5.10 The most dominant frequency of secondary instability modes at several streamwise (x) locations for first (smaller) vortex.

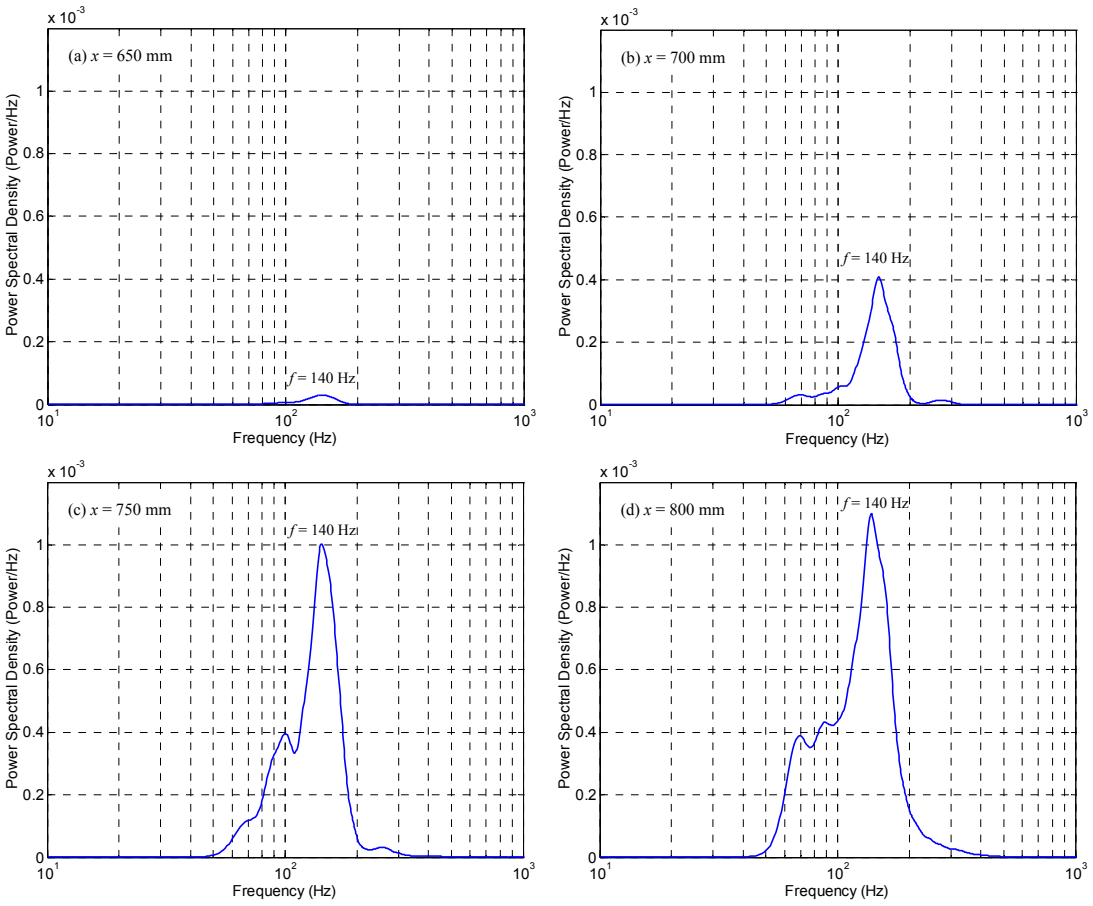

FIG. 5.11 The most dominant frequency of secondary instability modes at several streamwise (x) locations for second (larger) vortex.

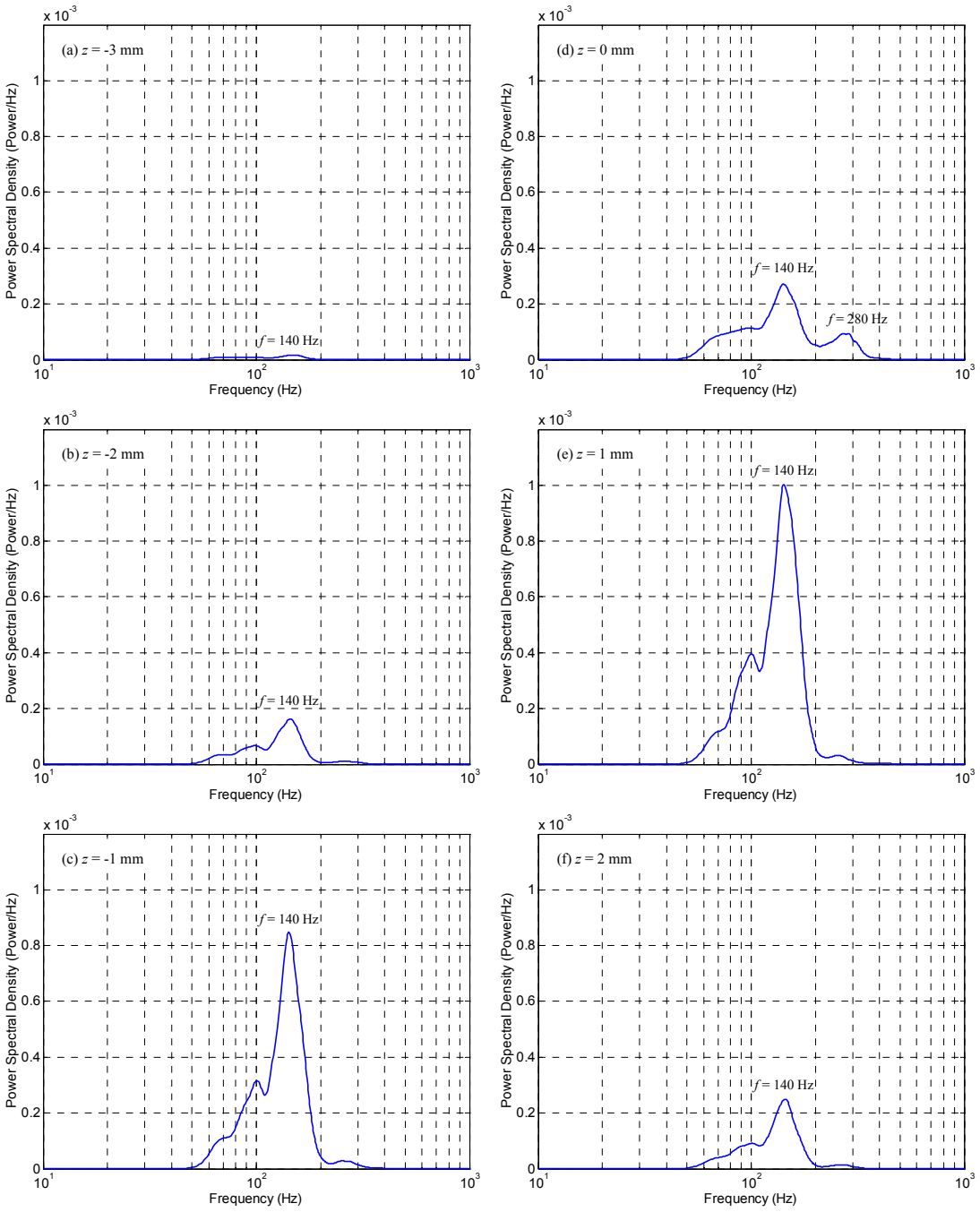

FIG. 5.12 Power spectral density of secondary instability modes at several spanwise (z) locations. The spectra are obtained from the location of the most unstable mode at y/δ_L = 0.30 for the streamwise location x = 750 mm.

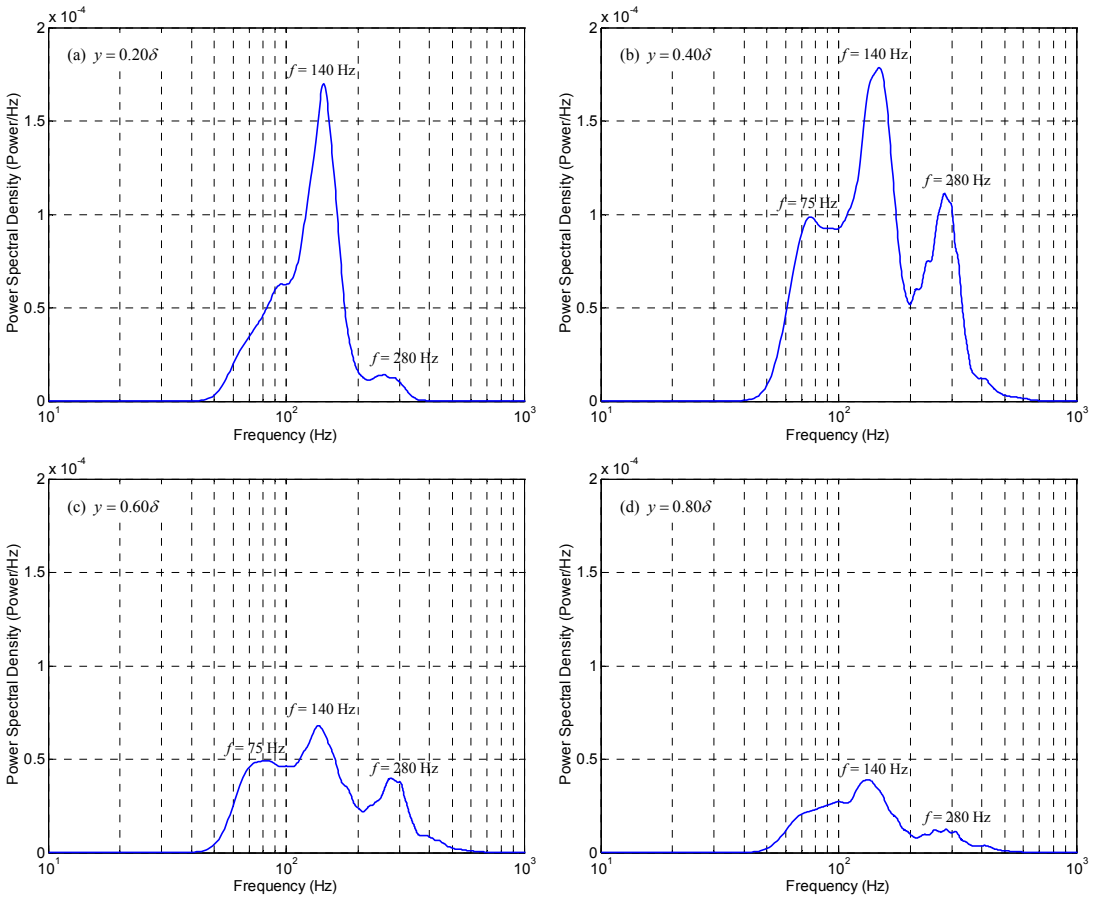

FIG. 5.13 Power spectral density of secondary instability at various normal (y) locations at the middle of upwash for x = 750 mm.

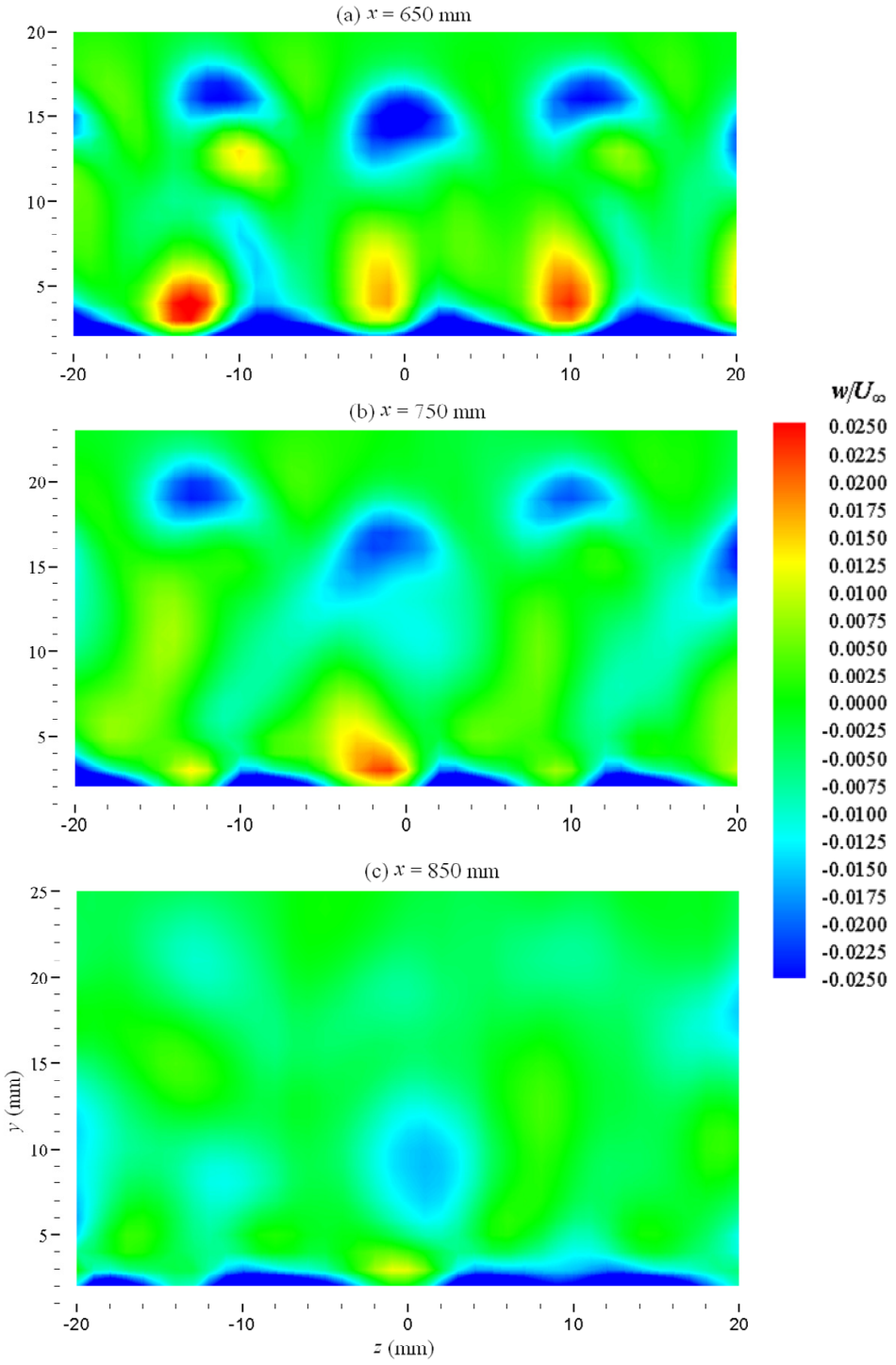

FIG. 6.1 Mean spanwise velocity (w/U_∞) contours on *y*-*z* plane.

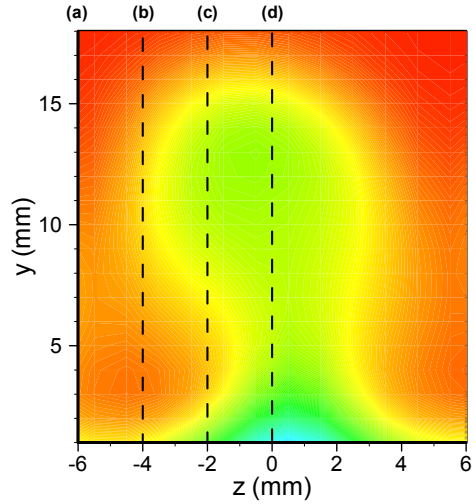

(i) Streamwise velocity contour showing four different spanwise (z) locations:
(a) middle of downwash region
(b) side of downwash region
(c) side of upwash region
(d) middle of upwash region

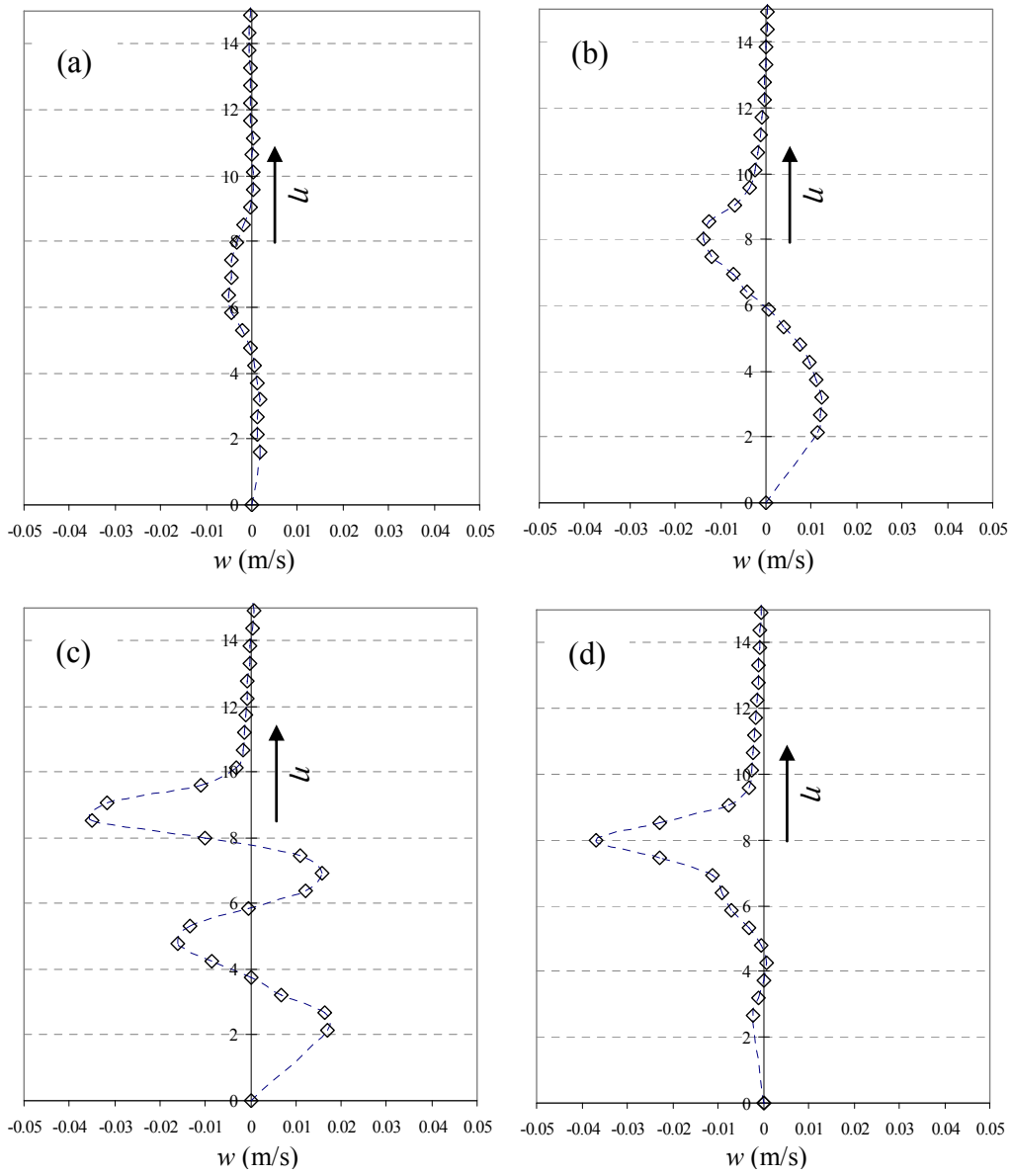

FIG. 6.2 Mean spanwise velocity (w/U_∞) profiles at some spanwise (z) locations (see Fig. 6.2(i)) for x = 650 mm.

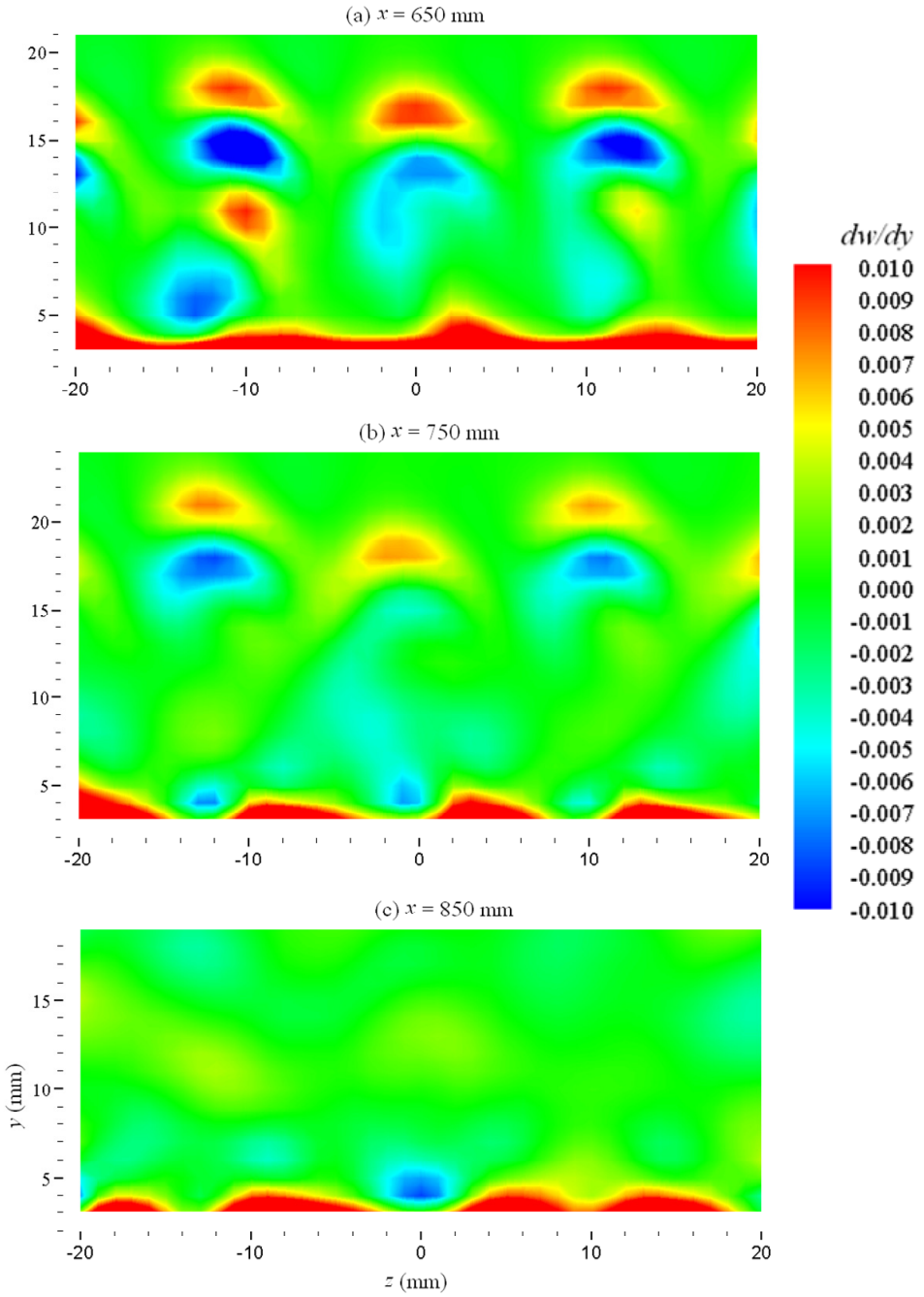

FIG. 6.3 Iso-shear ($\partial w/\partial y$) contours on y-z plane at several streamwise (x) locations.

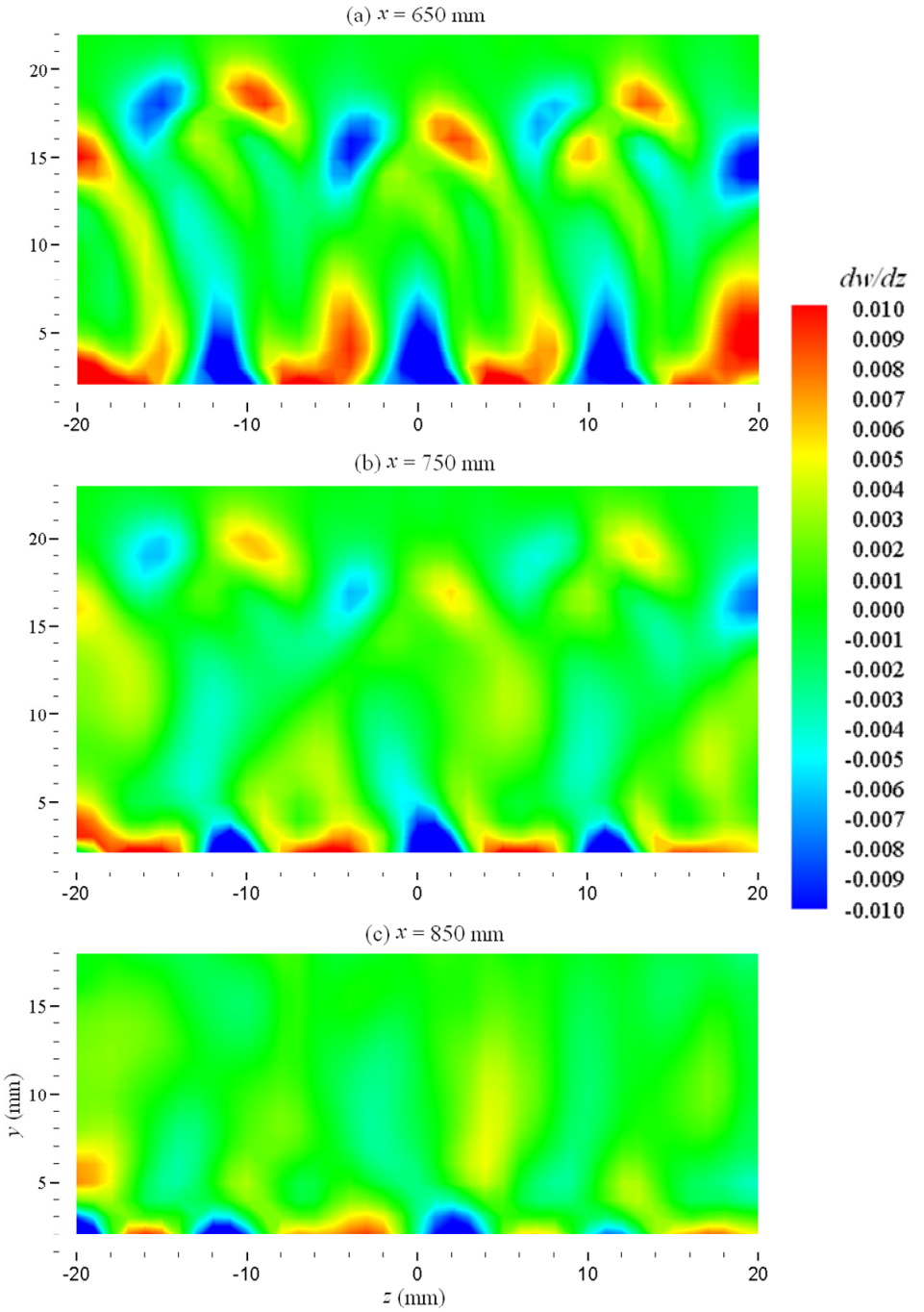

FIG. 6.4 Iso-shear ($\partial w/\partial z$) contours on y-z plane at several streamwise (x) locations.

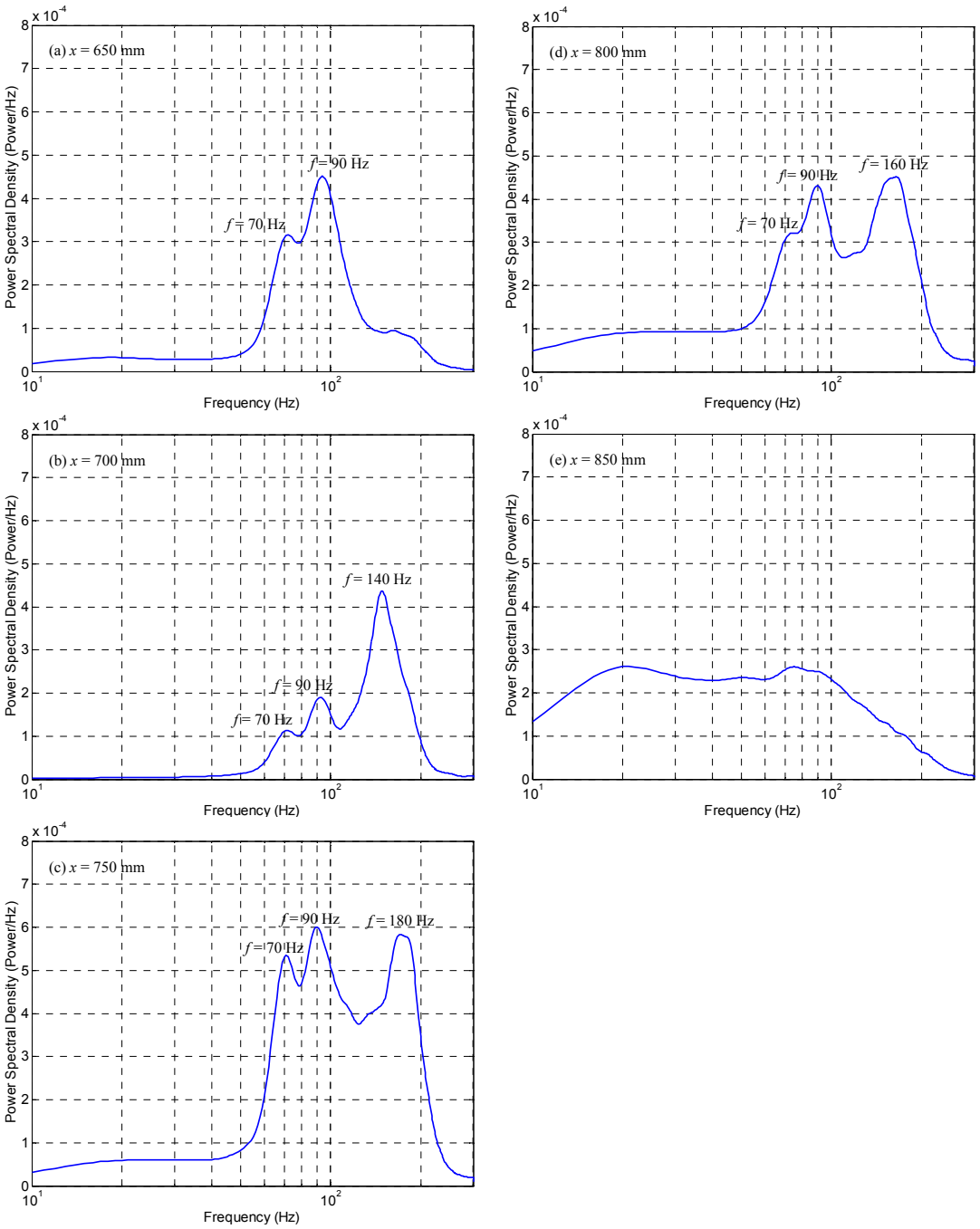

FIG. 6.5 Power spectra density of the spanwise velocity component w at several streamwise (x) locations.

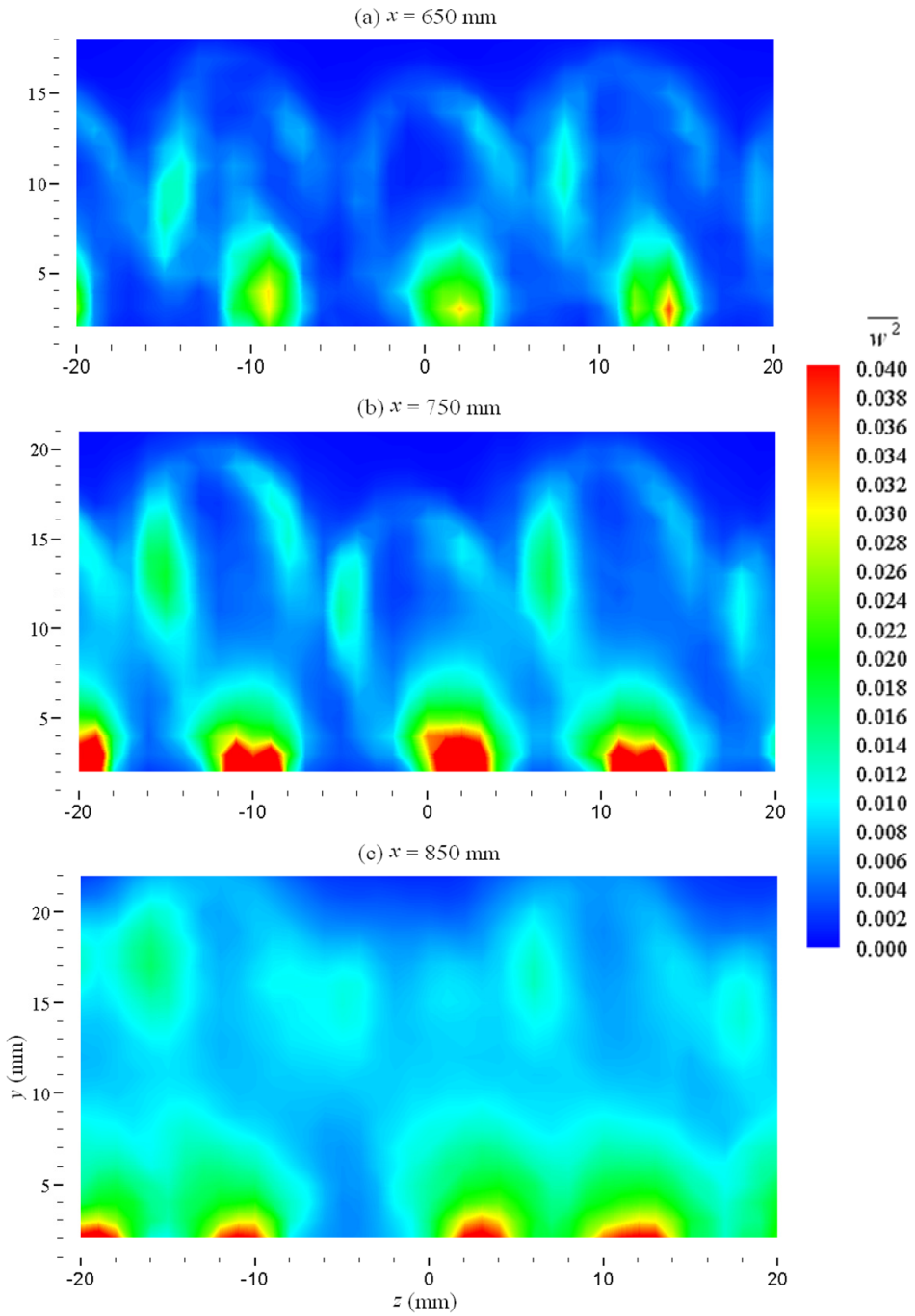

FIG. 6.6 Reynolds normal stress ($\overline{w'^2}$) contours on y-z plane at several streamwise (x) locations.

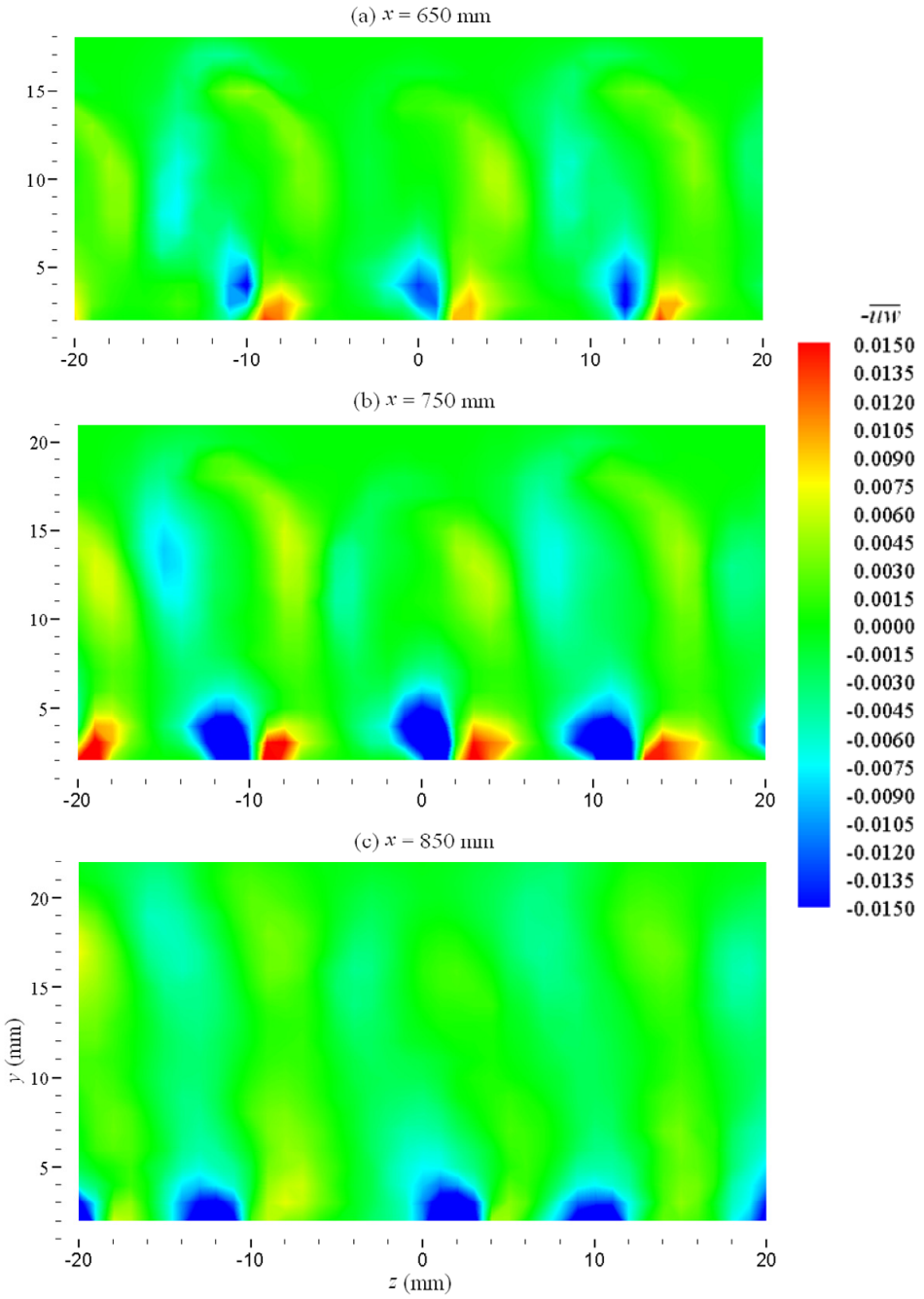

FIG. 6.7 Reynolds shear stress ($-\overline{u'w'}$) contours on y-z plane at several streamwise (x) locations.

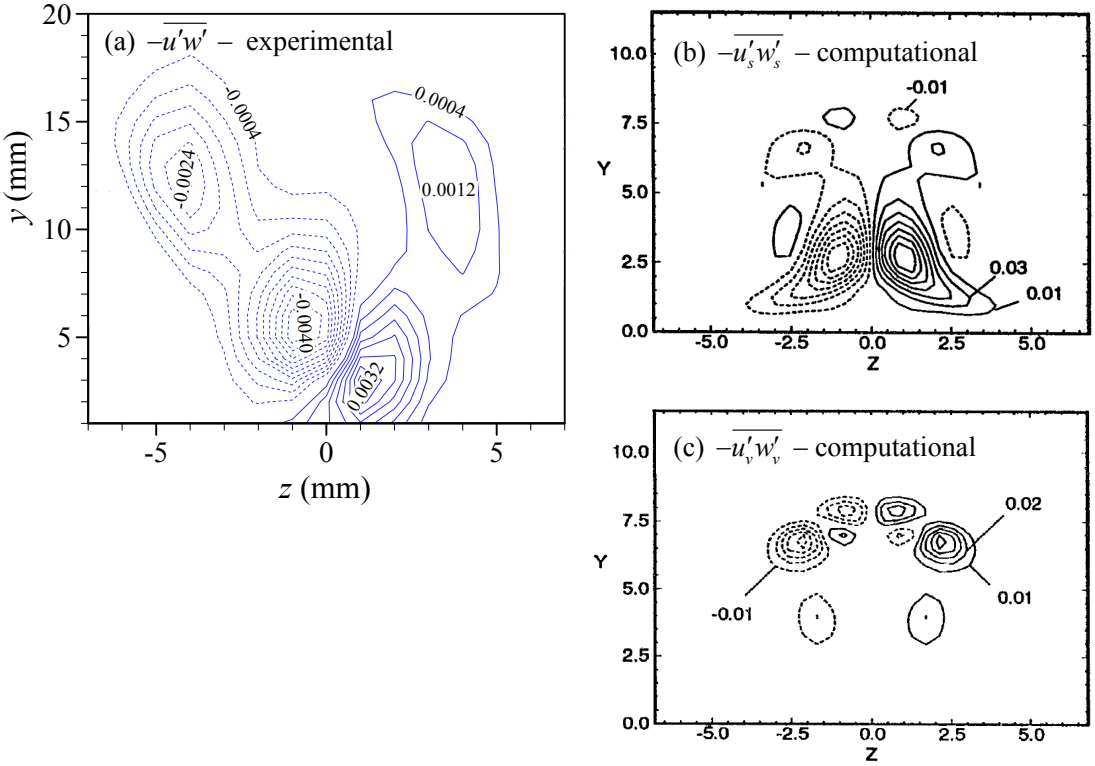

FIG. 6.8 Contours of Reynolds shear stress $-\overline{u'w'}$: (a) experimental result at x = 700 mm, and computational results of Yu and Liu (1994) for (b) sinuous mode, (c) varicose mode.

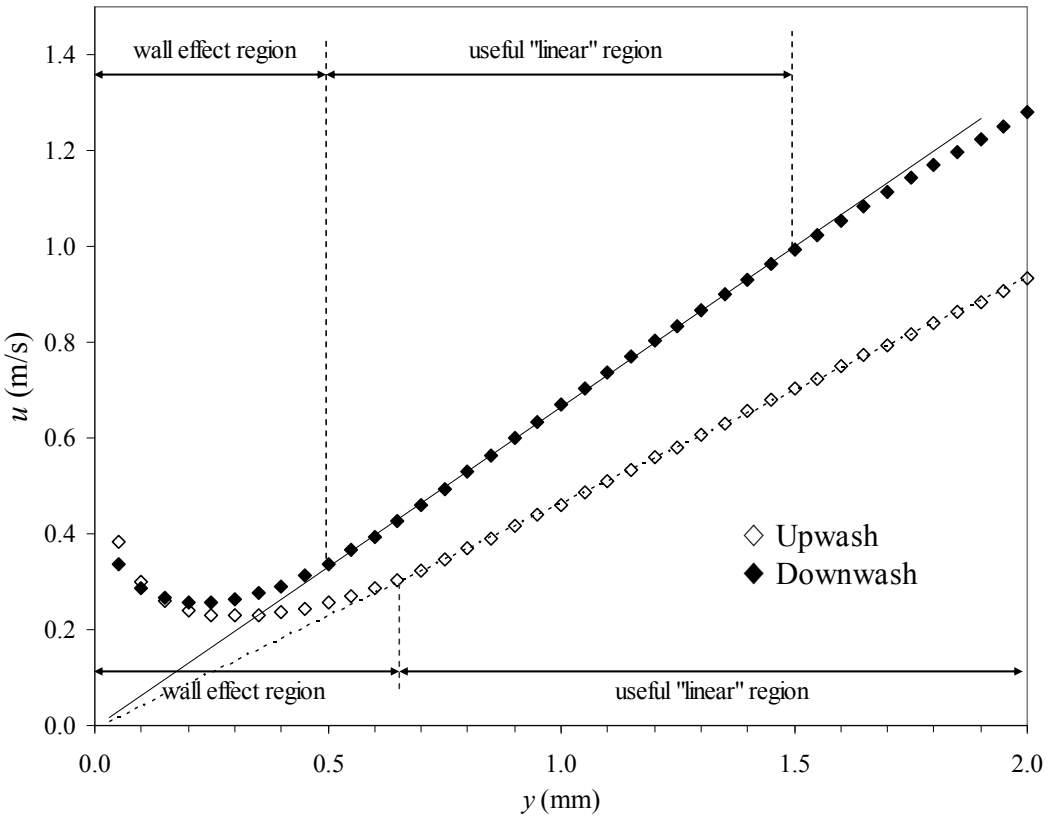

FIG. 7.1 A typical near-wall streamwise velocity measurements at upwash and downwash measured at x = 200 mm for case 2 (λ_m = 15 mm and U_∞ = 2.1 m/s).

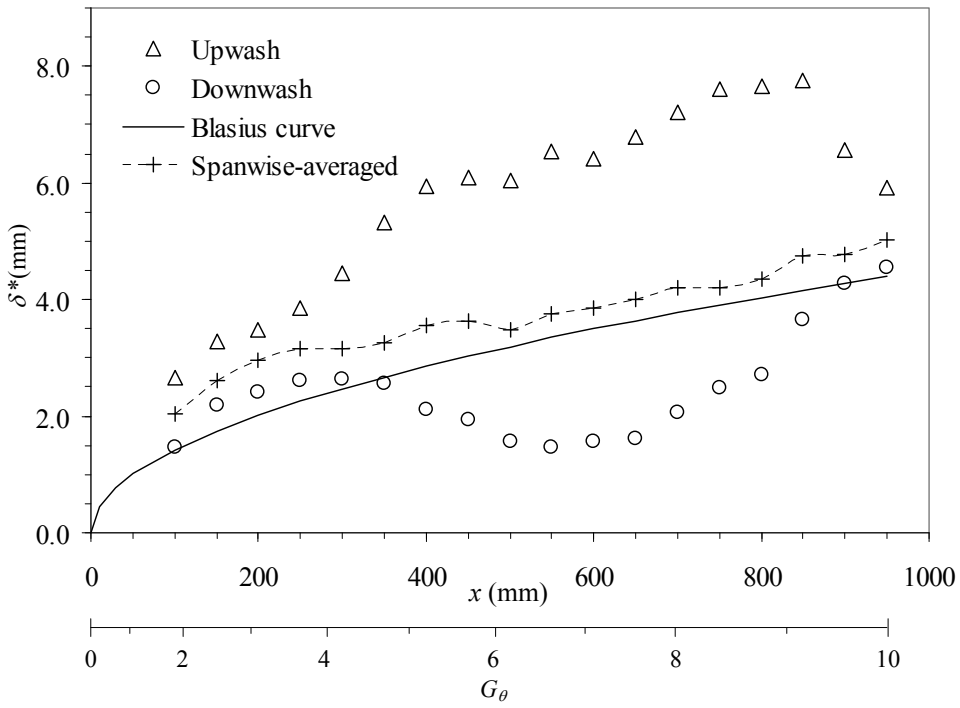

FIG. 7.2 Developments of boundary layer displacement thickness δ^* for case 2 (λ_m = 15 mm and U_∞ = 2.1 m/s).

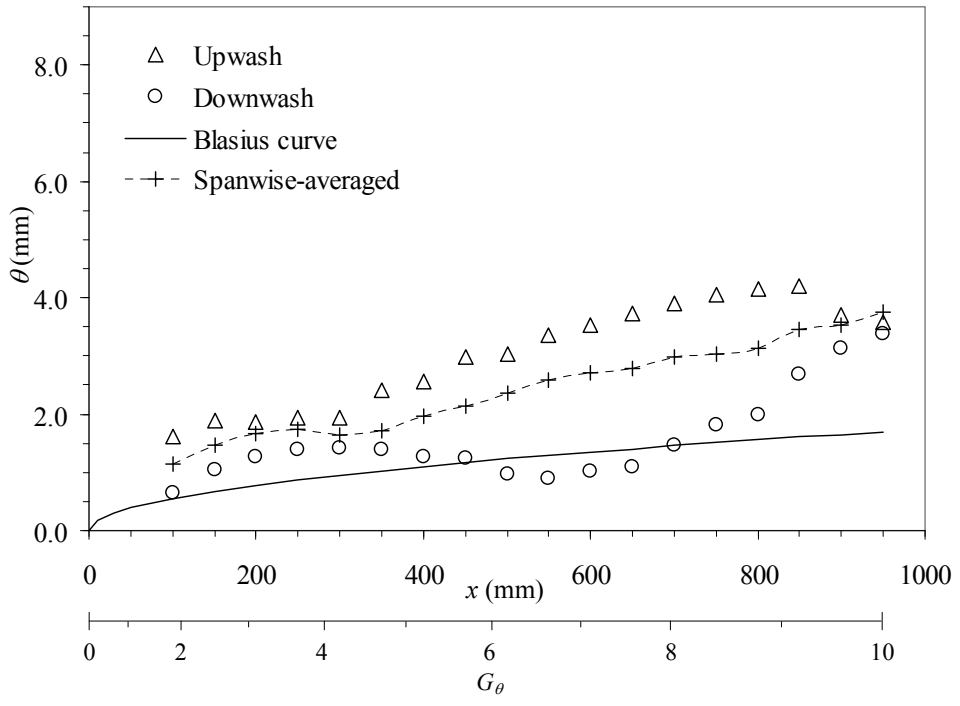

FIG. 7.3 Developments of boundary layer momentum thickness θ for case 2 (λ_m = 15 mm and U_∞ = 2.1 m/s).

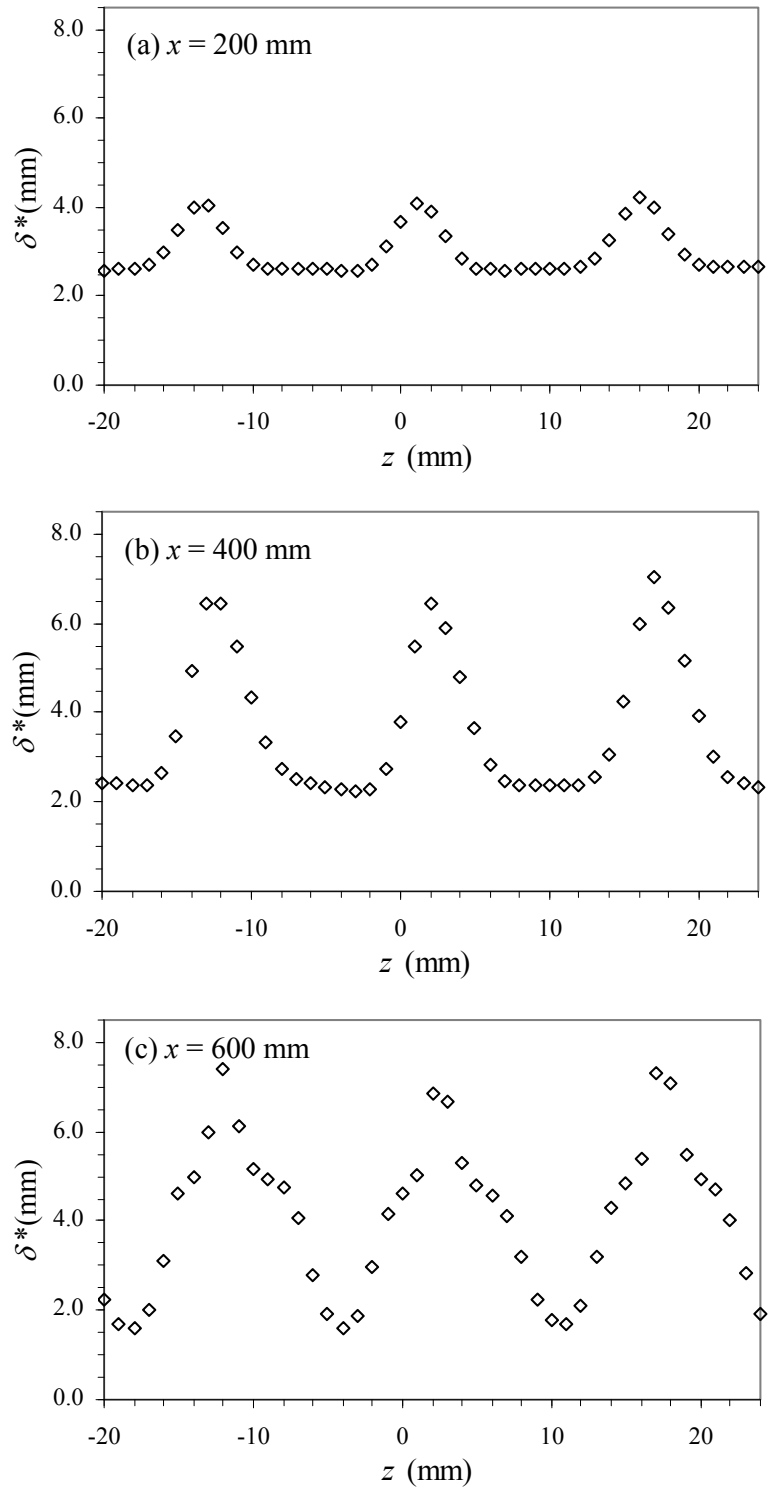

FIG. 7.4 Spanwise distribution of boundary layer displacement thickness δ^* at several streamwise (x) locations for case 2 (λ_m = 15 mm and U_∞ = 2.1 m/s).

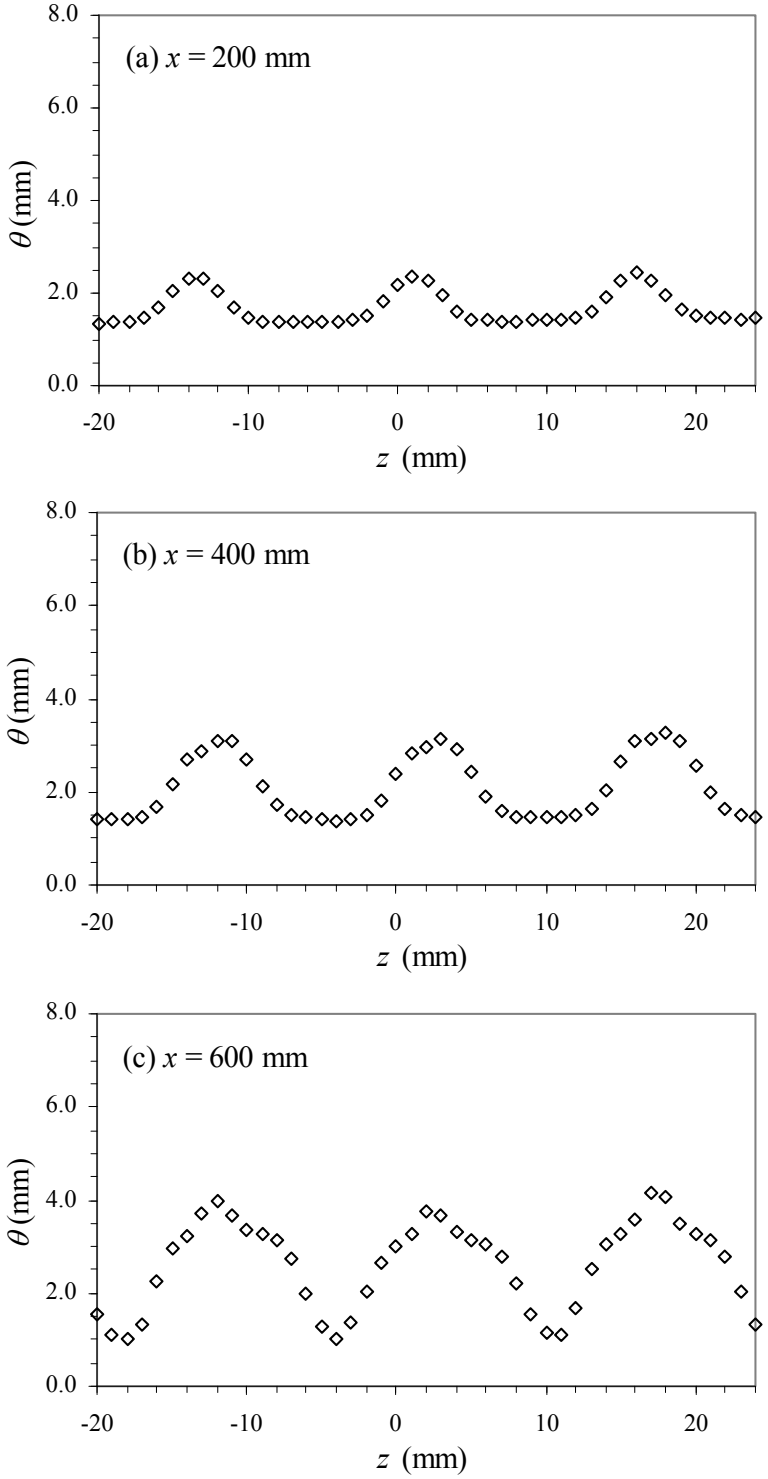

FIG. 7.5 Spanwise distribution of boundary layer momentum thickness θ at several streamwise (x) locations for case 2 (λ_m = 15 mm and U_∞ = 2.1 m/s).

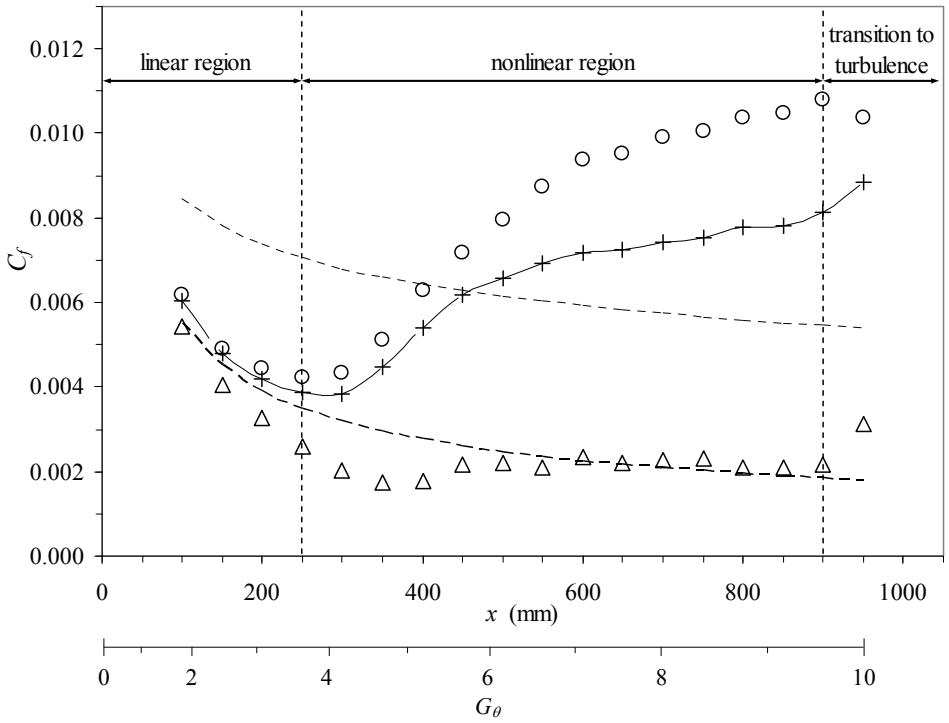

FIG. 7.6 Wall shear stress coefficient C_f for case 2: λ_m = 15 mm and U_∞ = 2.1 m/s (Δ : at upwash, O : at downwash, $-+-$: spanwise-averaged value $\overline{C}_f$, ——: Blasius boundary layer, ----- : turbulent boundary layer).

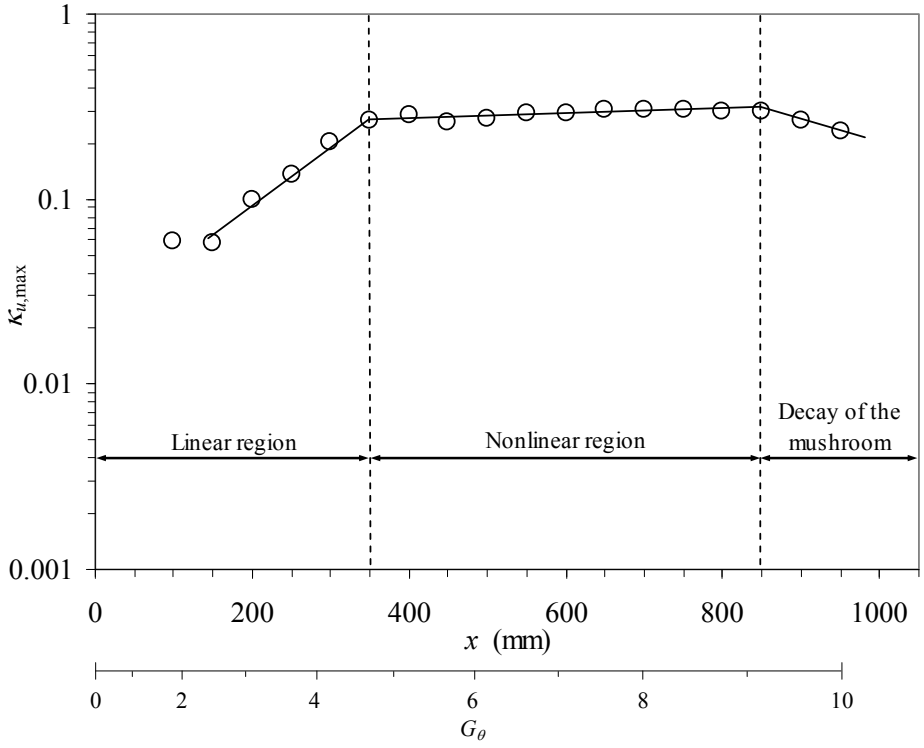

FIG. 7.7 Development of maximum disturbance amplitude $\kappa_{u,\max}$ for case 2 (λ_m = 15 mm and U_∞ = 2.1 m/s) showing three different regions, namely linear region, nonlinear region, and decay of the mushroom structures.

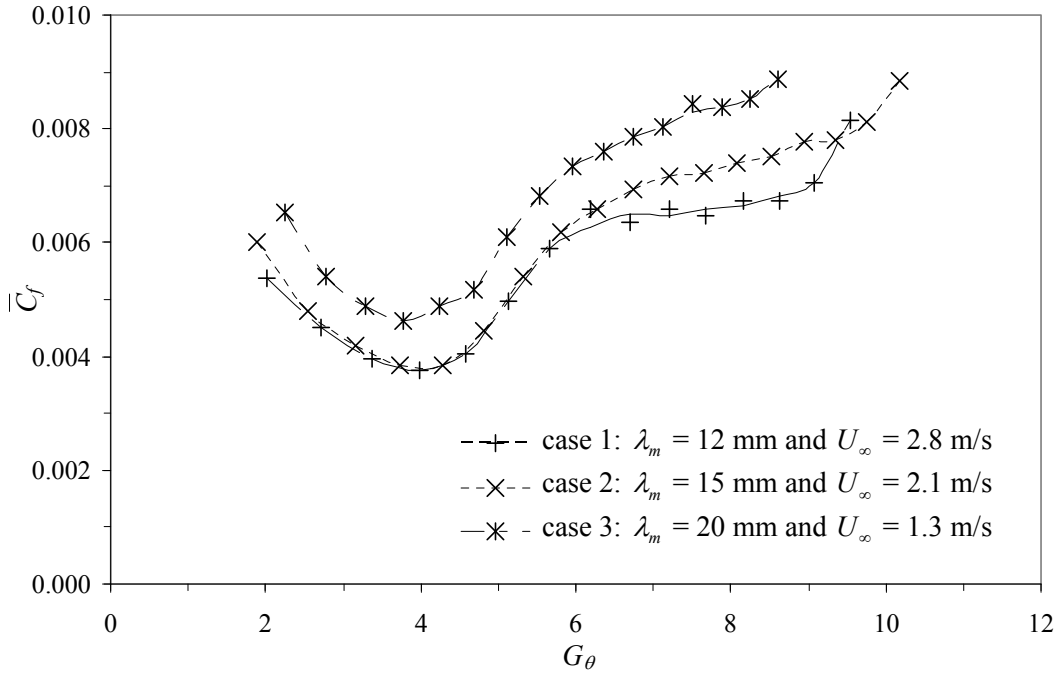

FIG. 7.8 Spanwise-averaged wall shear stress coefficient $\overline{C}_f$ versus Görtler number G_θ for case 1: λ_m = 12 mm and U_∞ = 2.8 m/s, case 2: λ_m = 15 mm and U_∞ = 2.1 m/s, case 3: λ_m = 20 mm and U_∞ = 1.3 m/s.

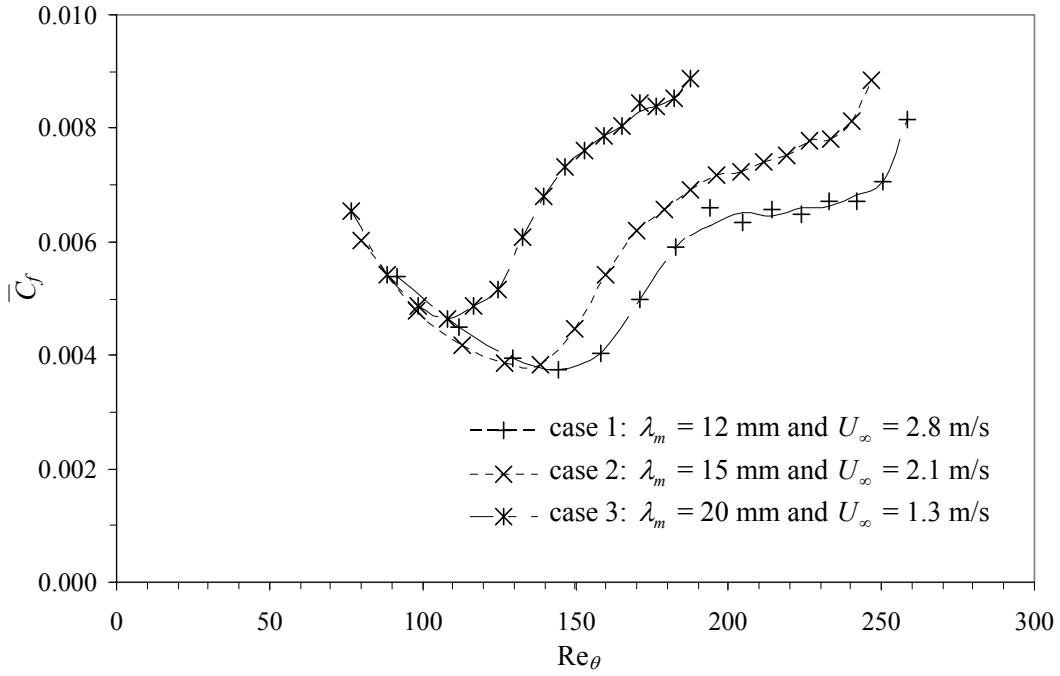

FIG. 7.9 Spanwise-averaged wall shear stress coefficient $\overline{C}_f$ versus Reynolds number Re_θ for case 1: λ_m = 12 mm and U_∞ = 2.8 m/s, case 2: λ_m = 15 mm and U_∞ = 2.1 m/s, and case 3: λ_m = 20 mm and U_∞ = 1.3 m/s.

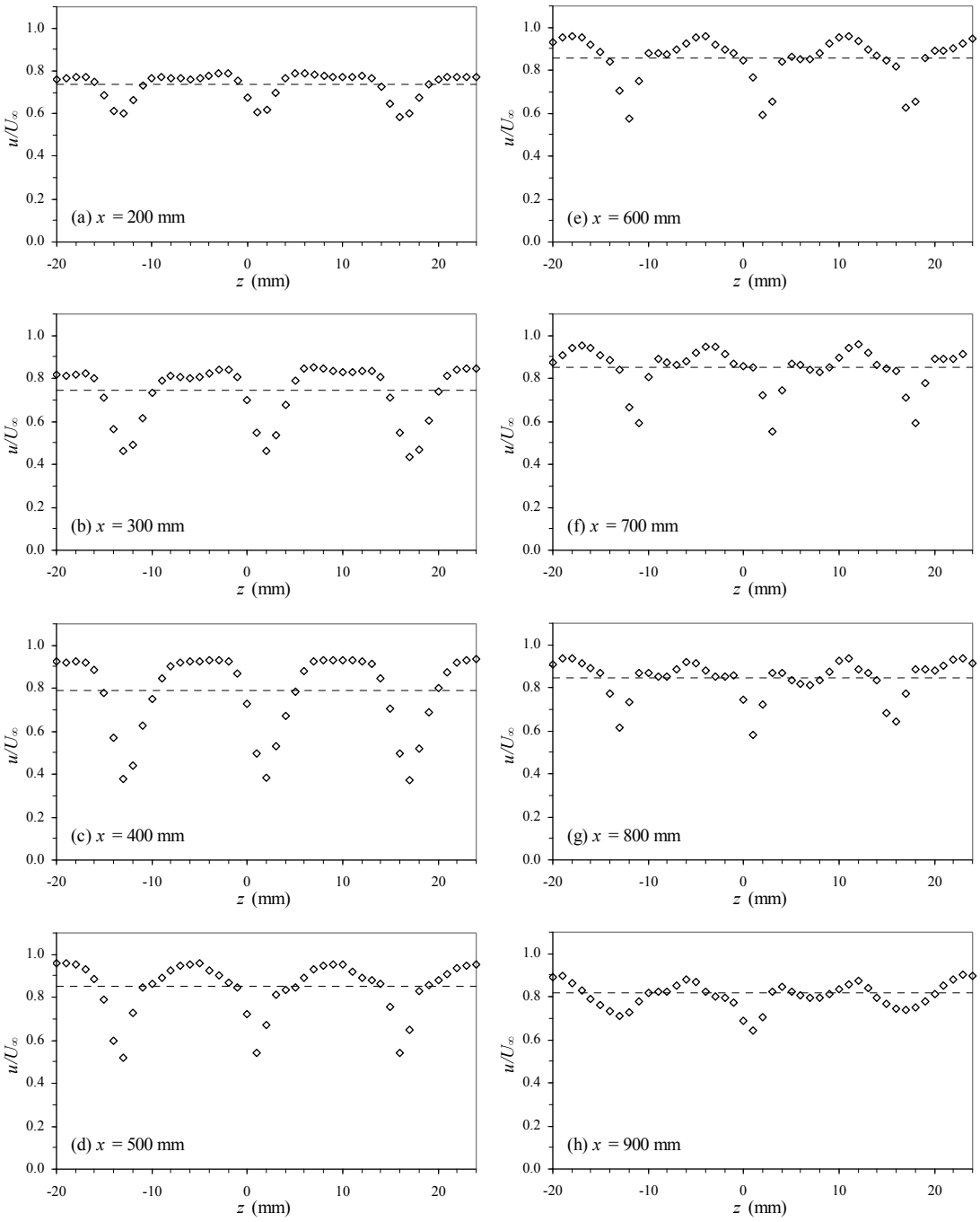

FIG 7.10 Spanwise distributions of mean streamwise velocity u/U_∞ for case 2: λ_m = 15 mm and U_∞ = 2.1 m/s at $y = 0.5\delta_L$ (------ is spanwise-averaged value of u/U_∞ at corresponding streamwise position).

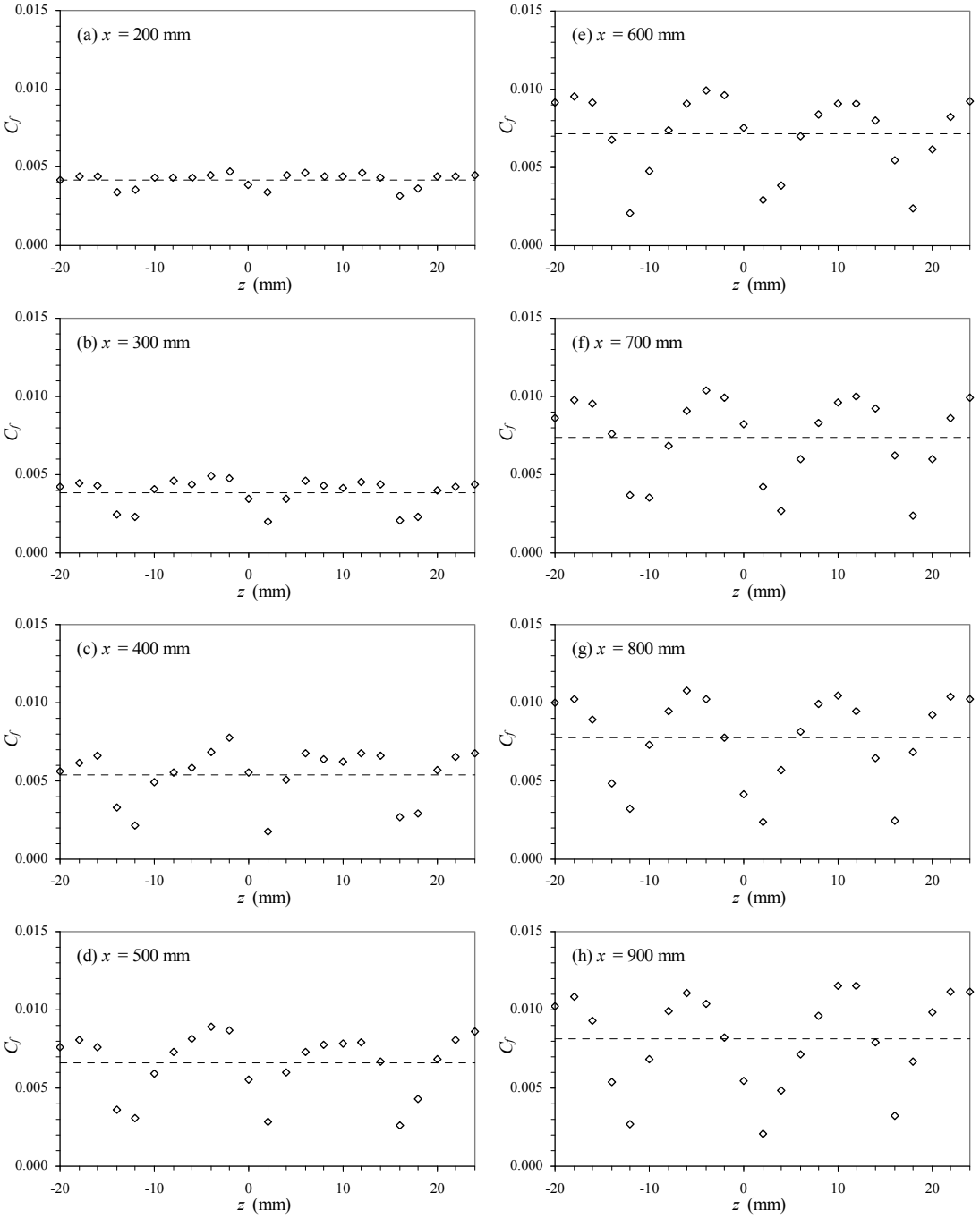

FIG. 7.11 Spanwise distributions of wall shear stress coefficient C_f for case 2: λ_m = 15 mm and U_∞ = 2.1 m/s (------ is spanwise-averaged value $\overline{C}_f$ at corresponding streamwise position).